Schweizerische Eidgenossenschaft
Confédération suisse
Confederazione Svizzera
Confederaziun svizra

Federal Department of the Environment, Transport, Energy and Communications DETEC

Swiss Federal Office of Energy SFOE
Energy Research and Cleantech

Yearly Report January 25, 2026

ModIceCrys

CFD Numerical modelling and experimental analysis of ice crystallizers for supercooling flows

Publisher:

Swiss Federal Office of Energy SFOE
Energy Research and Cleantech
CH-3003 Bern
www.energy-research.ch

Subsidy recipients:

OST - Ostschweizer Fachhochschule
SPF Institut für Solartechnik
Oberseestr. 10
CH-8640 Rapperswil
www.spf.ch

Authors:

Ignacio Gurruchaga, ignacio.gurruchaga@ost.ch
Daniel Carbonell, DCarbo Energy Consulting S.L., daniel.carbonell@dcarbo.es

SFOE project coordinators:

Elena-Lavinia Niederhäuser, elena-lavinia.niederhaeuser@bfe.admin.ch
Stephan A. Mathez, stephan.a.mathez@bfe.admin.ch

SFOE Contract number: SI/502570-01

Contents

List of Acronyms

BSI	Backlight Shadow Imaging
CCD	Charged-coupled Device
CFD	Computational Fluid Dynamics
CNT	Classic Nucleation Theory
DOF	Depth of Field
DVR	Dynamic Velocity Range
EER	Energy Efficiency Ratio
FOV	Field of View
GSHP	Ground Source Heat Pump
LMTD	Logarithmic Mean Temperature Difference
PBE	Population Based Equations
PBM	Population Based Model
PCM	Phase Change Material
PIV	Particle Image Velocimetry
QFV	Quantitative Flow Visualization
ROI	Region of Interest
RANS	Reynolds Averaged Navier Stokes
SPF	Seasonal Performance Factor
SS	Sensor Size
TES	Thermal Energy Storage
UDF	User-Defined Function
VDP	Valid Detection Probability

List of Symbols

Latin letters

A_{wi}	Hamaker constant, in J.
A_{sl}	interfacial area concentration, is the area between two phases per unit volume, $m^2\,m^{-3}$.
d_0	capillary length, m.
d_s	characteristic diameter of the solid particles, also referred as L in population balance equations, m.
e_{ss}	is the coefficient of restitution, -.
$error$	in the framework of this study, two main error functions will be used. The Root Mean Square Error (RMSE) and the Mean Absolute Percentage Error (MAPE).
f_{het}	heterogeneous nucleation factor, -.
G	Gibbs free energy, J.
G_V	volume Gibbs free energy, $J\,m^{-3}$.
G_S	surface Gibbs free energy, $J\,m^{-2}$.
$g_{0,ss}$	radial distribution function, -.
Gro_l	linear growth rate used in the Population Balance Equations is defined as the v_{tip}, the dendrite tip growth velocity, in $m\,s^{-1}$.

Gro_v	volumetric growth rate used in the Population Balance Equations is defined as the variation of volume per time unit, in $m^3\,s^{-1}$.
H	enthalpy, is a measure of the total energy of a system, accounts for both internal energy energy and work done against pressure forces, J.
h_{fus}	enthalpy of fusion, $J\,kg^{-1}$.
k_{agg}	aggregation kernel, which accounts for the aggregation of particles in the Population Balance Equations, in $m^3\,s^{-1}$.
k_{bre}	breakage frequency, which accounts for the fraction of particles breaking in the Population Balance Equations, in s^{-1}.
$k_{l,s}$	fluid-solid exchange momentum coefficients, $kg\,s^{-1}\,m^{-3}$.
k_B	Boltzamnn's constant $1\,380649e^{-23}$, $J\,K^{-1}$.
L	characteristic diameter of the solid particles, in m. Also referred as d_s in the CFD equations.
$\dot{m}_{s,l}$	mass transfer from $_s$-phase to $_l$-phase and viceversa in the CFD multiphase model, $kg\,s^{-1}$.
n_i	refractive index of an optical medium is the ratio of the apparent speed of light in the air or vacuum to the speed in the medium. n_i, -.
ndf	number density function, used in Population Balance Equations represents a function defining the density of particles of a specific size L, -.
Nu	the Nusselt number (Nu) is a dimensionless quantity used in heat transfer calculations. It represents the ratio of convective to conductive heat transfer, -.
p	static pressure, Pa.
p_s	solids pressure in granular flow, Pa.
$pdf(L\|L')$	probability density function of particles of size L' breaking into particle of size L used in the Population Balance Equations, in m^{-3}.
ppp	number of child particles produced per parent particle used in breakage term in Population Balance Equations, -.
r_n	radius of a small nucleus, m.
r_c	critical radius for nucleation, m.
r_{tip}	tip radius of a dendrite, m.
S	entropy, J.
S	intensive or specific entropy, $J\,kg^{-1}$.
T	temperature, °C (except it is explicitly expressed in K).
T_{sc}	supercooling temperature, °C.
T_m	melting temperature, °C.
$\vec{u}_q$	velocity vector of the $_q$-phase in the CFD multiphase model, $m\,s^{-1}$.
v_{tip}	dendrite tip growth velocity, $m\,s^{-1}$.

Greek letters

α_{diff}	thermal diffusivity, $m^2\,s^{-1}$.
α_q	volume fraction of the $_q$-phase in the CFD multiphase model, $m^3\,m^{-3}$.
γ_{iw}	interfacial energy between ice and water, $J\,m^{-2}$.
γ_{isurf}	interfacial energy between ice and surface, $J\,m^{-2}$.
γ_{wsurf}	interfacial energy between water and surface, $J\,m^{-2}$.
Δ_{p_e}	Péclet adimensional number, -.

ΔT_{sc}	supercooling degree, K.
ζ_T	factor for coalescence efficiency of turbulent collision, -.
Θ_s	granular temperature for solid phase in dense granular flows, °C.
θ_{wett}	wetting angle, rad.
$\dot{\lambda}$	is the deformation rate, in s^{-1}.
$\mu_{s,col}$	collisional viscosity component for solid shear stresses, $kg\,(m\,s)^{-1}$ or $N\,s\,m^{-2}$ or $Pa\,s$.
$\mu_{s,kin}$	kinetic viscosity component for solid shear stresses, $kg\,(m\,s)^{-1}$ or $N\,s\,m^{-2}$ or $Pa\,s$.
$\mu_{s,fr}$	friction viscosity component for solid shear stresses, $kg\,(m\,s)^{-1}$ or $N\,s\,m^{-2}$ or $Pa\,s$.
ν	kinematic viscosity, $m^2\,s^{-1}$ or $N\,m\,s\,kg^{-1}$ or $J\,s\,kg^{-1}$.
ξ	bulk viscosity for solid phase in dense granular flows, $kg\,(m\,s)^{-1}$.
ρ	density, $kg\,m^{-3}$.
ρ_q	density of the $_q$-phase in the CFD multiphase model, $kg\,m^{-3}$.
σ_{LM-K}	LM-K stability constant, -.

Subindexes

q	subindex for any phase.
l	subindex for liquid.
s	subindex for solid.
wat	subindex for water.
ice	subindex for ice.

.

Glossary

Notation	Description	Page List
attrition	the process of crystal erosion or breaking into smaller pieces when subjected to stress, e.g. due to collision a high fluid shear	71
BCF theory	a continuous crystal growth model developed by Burton, Cabrera and Frank in which the dislocations of existing crystals are the source of further growth.	57
Continuity equation	or conservation of mass equation, are a set of partial differential equations than state the conservation of mass. Coupled with conservation of momentum and energy equations form the governing equations for analyzing fluid flows.	63
dynamic velocity range	in PIV o BSI techniques is the maximum velocity range that can be measured with fixed set of instrumental optical and imaging system.	46
embryos	unstable, conglomerates of liquid particles, which may grow depending on local thermal conditions. Stable embryos that have grown larger than the critical radius are called nucleus.	54
focal length	is a fundamental lens parameter that describes how strongly the lens converges or diverges light. Lenses with longer focal lengths bend light more gradually, while shorter focal lengths bend it more sharply. For a thin convex lens, the focal length is the distance from the lens to the image plane when the object is at infinity.	48
Gibbs free energy	the thermodynamic potential that can be used to calculate the maximum amount of work that may be performed by a thermodynamically closed system at constant temperature and pressure, or equivalently, the maximum amount of non-expansion work that can be extracted from a closed system. During crystallization processes the Gibbs free energy change is: $\Delta G = \Delta H - T \cdot \Delta S$	54
granular flow	is a multiphase flow composed by a fluid and a collection of discrete solid material that flow in a manner similar to fluids but also exhibit some properties of solids.	63

Notation	Description	Page List
ice slurry	ice slurry is a pumpable biphasic mixture of small solid ice particles immersed in water or a mixture of water and a freezing point depressant.	11
LM-K theory	a theory developed by Langer and Müller-Krumbhaar (1970) which provided a universal model for dendritic growth rate based on stability criteria.	57
Navier-Stokes equation	or conservation of momentum equation, are a set of partial differential equations than describe the motion of a fluid. They are based on Newton's second law applied to fluid motion, incorporating surface and body forces, as viscous, pressure or gravity. Coupled with conservation of mass and energy equations form the governing equations for analyzing fluid flows.	66
nucleation	initial formation of embryos, when no ice crystals are present beforehand. This can happen homogeneously within the metastable supercooled liquid itself or heterogeneously originated by a foreign substrate.	54
nucleus	stable embryo.	54
orthogonality	property of a mesh for assessing its quality related to the angle between adjacent cells. A mesh with good orthogonality, a value closer to 1, is one whose cell faces are perpendicular to each other. A mesh with poor orthogonality, with a value closer to 0, may lead to poor numerical convergence and accuracy. The acceptable values for orthogonality should be above 0.8 - 0.9.	18
phase change material	a substance capable of undergoing a transition between solid and liquid states at a specific temperature, absorbing or releasing a significant amount of latent heat during this phase transition. PCMs are employed for thermal energy storage, helping to manage and regulate temperatures in various applications, including building construction, electronics, and renewable energy systems.	11
polymorphism	in the context of ice crystals refers to the capacity of ice to be formed in different crystalline forms, depending on factors like temperature, pressure or cooling rate.	58

Notation	Description	Page List
Péclet	is an adimensional number that is defined as the ratio of the rate of advection (convection) to the rate of diffusion. For example, in fluid flow through a pipe or over a surface, a high Péclet number suggests that the fluid is effectively carrying heat with it, while a low Péclet number suggests that heat is mainly conducted through the material.	60
resolution	refers to the smallest feature size of an object that an imaging system can distinguish. It is typically expressed as a spatial frequency, measured in line pairs per millimeter. While resolution is sometimes reported as a single dimension, describing it purely as the minimum resolvable size is incomplete. A more accurate definition treats resolution as a frequency, quantified in line pairs per millimeter. A line pair consists of one black and one white bar in object space. Lens resolution, however, is not absolute. At a given spatial frequency, the ability to distinguish the two bars depends on the difference in grayscale intensity between them. The greater this contrast, the more easily the system can resolve the line pair. Thus, resolution is defined as the spatial frequency at which a specified contrast level is achieved.	48
secondary nucleation	heterogeneous nucleation at the surface of an already existing seed crystal, with different crystal orientation.	54
skewness	property of a mesh for assessing its quality and quantifies how much the shape of the cell is distorted from the ideal (normally a perfect square or cube). A mesh with low skewness, a value closer to 0, is one with regular-shaped cells, close to the ideal square or cube. A mesh high skewness value indicates that the cells are highly distorted, deviating significantly from the ideal square or cube, which may lead to poor numerical convergence and accuracy. The acceptable values for skewness should be below 0.2.	18
Stefan's problem	formulates the evolution of the movable boundary between the phases of a material undergoing phase change.	57
valid detection probability	in PIV o BSI techniques is the fraction of vector fields that are considered valid after correlation and validation processes. A high VDP (close to 100%) means most image regions produced reliable velocity measurements while a low VDP indicates many correlation failures — often due to: out-of-plane particle motion or poor image contrast for example.	46

1 Motivation

The need for thermal energy storage to integrate high shares of renewable energy

Decarbonised energy systems increasingly rely on renewable technologies, including solar thermal, photovoltaic, wind turbines, biomass, and heat pumps. Although these technologies are becoming more cost-competitive, their contribution to meeting high shares of heating and cooling demand is limited by temporal mismatches between local resource availability (e.g., solar radiation, wind, biomass, or favourable source/sink temperatures) and energy demand profiles. Renewable generation and demand exhibit both seasonal and daily variations: solar energy is highest during daytime hours, while heating or cooling demand may occur at night or during other hourly periods. Specifically, solar energy peaks in spring and summer, residential heating demand is highest in winter, residential cooling peaks in hot periods, and industrial heating and cooling largely depends on the seasonal characteristics of specific processes.

A key challenge arises when energy management is analysed from a local perspective, for instance, within a single industrial site, residential complex, or district network. Focusing on the local level allows owners and operators to maximise self-consumption, reduce reliance on the wider electrical grid, and mitigate peak loads. In this context, excess renewable generation, that cannot be immediately locally utilised, may otherwise be exported to the grid, potentially stressing or saturating distribution infrastructure. Thermal energy storage (TES) provides a flexible solution, storing energy when available and releasing it when needed. TES smooths demand, reduces peak stress, decouples production from consumption, and increases the operational flexibility of heating and cooling systems across sectors from residential to industrial. Depending on the application, TES can range from short-term hourly or daily storage to long-term seasonal storage.

Among short-term TES technologies, ice storage, as a phase change material (PCM), is particularly attractive for applications requiring cooling or low-temperature heat. Its high energy density (334 $\mathrm{kJ\,kg^{-1}}$ compared to chilled water storage 21 $\mathrm{kJ\,kg^{-1}}$ for $\Delta T = 5$ K) reduces the required storage volume, lowering capital expenditure for vessels and thermal losses due to a smaller surface area exposed to the environment.

Ice storage is applicable across industrial facilities (e.g., fishing, dairies or general food processing Kauffeld et al. (2010)), residential buildings (e.g., space cooling or solar-ice systems as in the TRI-HP project [1]), and district heating and cooling networks, where it can act as a local buffer, shifting loads and reducing peak demands on the grid Kozawa et al. (2005). Building on these advantages, the Ice-Grid project Shubert et al. (2020) analysed the integration of ice storage into low-temperature *anergy* networks, focusing on both seasonal and short-term storage, concluding that ice storage can enhance network flexibility, support system expansion in future low-temperature district heating networks.

About the need to go one step further on the state-of-the-art of ice storages

The actual technology for ice storage, currently named "ice-on-coil" technology, shown in Figure 1, consists of a vessel using evenly distributed embedded tubes inside.

An anti-freeze heat transfer fluid flows through these tubes, causing ice to form on the outer heat transfer surface of the tubes. This approach has the advantage of relative simplicity, without moving parts. However, the embedded tubes represent a high cost that scales with thermal capacity and required thermal charging or discharging power, making the levelized cost of storage less competitive. In addition, the low thermal conductivity of ice forms a self-insulating layer. For example, for a capillary tube with a diameter of 5 mm, increasing the ice layer thickness from 10 mm to 100 mm reduces the heat transfer rate by approximately 57 %.

Similarly to the ice-on-coil concept, there is "ice-on-plate," in which, instead of tubes, plates serve as the heat transfer surface, functioning essentially as a type of heat exchanger. However, the same phenomenon

[1] An example of the development of the solar-ice technology was implemented within the framework of the European TRI-HP project (`www.tri-hp.eu`), in which several solutions for residential trigeneration (the generation of electricity as well as heating and cooling) were developed and analysed for the residential sector. As part of this project, a solar-ice slurry storage system, integrated with solar thermal, photovoltaics and a natural-refrigerant heat pump was designed to cover electricity, heating and cooling demands in most of the central and northern European climates at least with an 80 % on-site renewable share, thus achieving the objective pursued. In this project, ice slurry storage was used as a thermal energy storage for the solar thermal system and as a heat source for the heat pump, achieving the same efficiency (Seasonal Performance Factor (SPF)) as a Ground Source Heat Pumps (GSHPs) -with the additional benefit of not needing to drill boreholes- enabling efficient coupling between renewable generation and heating and cooling demand.

Figure 1: Ice-on-coil storage view from inside, in the left side picture. On the right side, the formation of an ice layer around the internal tubing inherently reduces thermal conductivity. Source: Viessmann.

occurs: as the ice layer on the plates grows beyond a certain thickness, it acts as an insulating layer, reducing the thermal transfer capacity. This, in turn, decreases the efficiency of the refrigeration system used to produce the ice, since the machines must operate at lower temperatures to maintain the desired ice growth. Moreover, the thermal power available for charging or discharging the ice storage system is always limited by the available heat transfer surface, which increases costs when large storage capacities or high charging/discharging power are required.

In parallel, other ice storage technologies, not limited by the constraints of heat transfer surface area or ice layer growth, have emerged, such as ice slurry technology.

Ice slurry is a biphasic mixture of small ice crystals suspended in a water-based fluid, typically at an equilibrium temperature of 0 °C for pure water or lower when freezing point depressants such as ethanol or ethylene glycol are added (Fig. 2). As a *phase change material* (PCM), ice slurry stores large amounts of latent heat at low temperatures, providing a high-energy-density storage medium. In practical systems, the maximum ice mass fraction is around 50 % Kauffeld et al. (2010), which is lower than the 70 % to 80 % typically achievable in ice-on-coil tanks; nevertheless, the resulting thermal energy density remains several times higher than that of conventional sensible heat storage, reaching approximately 167 $\mathrm{kJ\,kg^{-1}}$.

Figure 2: Left: ice slurry viewed through a microscope. (Source: Michael Froehlich). Right: ice slurry produced by the supercooling method. (Source: SPF - Institut für Solartechnik)

The ice slurry method offers the following advantages compared to the ice-on-coil or ice-on-plate method:

- Avoidance of the in-tank heat exchanger where ice is produced with the respective cost reduction.

- Higher heat transfer rates due to the large contact area between ice particles and water.
- Higher chiller or heat pump performance due to the free-of-ice heat exchanger when the ice slurry uses only water. The refrigerant's evaporation temperature during ice making will be higher than in ice-on-coil or ice-on-plate systems, where it decreases with increasing ice thickness [2].
- No risk of cracking the storage casing due to the expansion of water when freezing and no need to have a structure that keeps the ice immersed, i.e. very cheap vessels, or even rooms or spaces not suitable for residential use in buildings as, e.g. parking spots, can be used to store slurries.
- Avoidance of brine usage as heat transfer fluid in the hydraulic loop between the heat pump and the storage vessel.
- Slurry production and storage take place in two different devices which allows to decouple power requirements and energy storage capability. This provides flexibility for the storage concept, i.e. flexible, cheap and modular storage designs are possible.

Ice slurry production methods

There are different methods of ice slurry production: fluidized bed, vacuum ice slurry, supercooling and the most commonly used mechanical scraping devices.

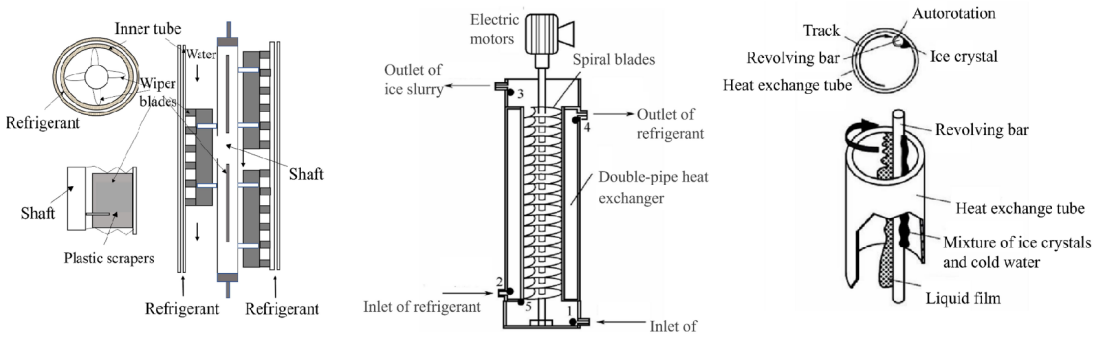

Figure 3: Schematic of ice slurry generators with moving parts, showing a) a rotary scraper type, and b) a spiral blade scraper and c) an orbital rod scraper. Schemes from Stamatiou et al. (2005)

The scraper design shown in Figure 3 uses mechanically scraped-surface heat exchangers, where ice is formed on a cold surface and is then removed continuously by a rotating mechanical rod that scrapes ice from a cylindrical barrel. The scraping mechanism creates ice shards that fall to the bottom of the barrel from where are transported away. This ice generating method requires high operation and maintenance cost, and has limited potential for scale up due to the mechanical constrains of the rotating-scraping rod.

For this reason, other ice-slurry production technologies, based on a passive concept for ice slurry production that does not rely on moving parts and that has high efficiency such as the supercooling method combined with a flow-based crystallizer, is desirable. The supercooling method involves cooling a substance below its melting point without it undergoing phase transition to the solid phase.

[2] For a thermal device such as a chiller, operating with ice-on-coil storage requires reducing the evaporator temperature to around −10.5 °C to overcome the thermal resistance of the ice layer on the coil surfaces. In contrast, when using ice slurry, the device only needs to reach the supercooler Logarithmic Mean Temperature Difference (LMTD) of about −4 °C. Operating at this higher temperature reduces the thermal lift required from the chiller, resulting in a higher energy efficiency ratio (EER) compared to the ice-on-coil configuration, where efficiency can be 10–20% lower depending on load and operating conditions.

Supercooling ice slurry production method

This method of producing ice slurry leverages the physical phenomenon of supercooling, sometimes referred to as subcooling, which is defined as "cooling a substance below the normal freezing point without the start of solidification" noa. In this process, a material remains in a metastable liquid state even when its temperature drops below the standard phase change point. This occurs because freezing or solidification requires more than just reducing the temperature; the molecules must also arrange themselves into an ordered, solid crystal structure. For crystallisation to occur, a nucleation site, a localised point where crystals can form and grow, is essential. These sites typically arise due to impurities, surface imperfections, or sudden thermal or pressure shocks. A key macroscopic parameter in this process is the supercooling degree (SD), defined as the difference between the melting temperature and the temperature of the supercooled liquid.

Figure 4 illustrates the thermodynamic cycle of the supercooling ice slurry method, which consists of three stages: supercooling, crystallization and utilization of ice slurry. (1) Supercooling, in which the liquid is cooled below its melting point without initiating crystallization; (2) Crystallization, where an external physical disturbance triggers the phase transition, reorganizing the disordered liquid molecular structure into an ordered solid lattice and converting sensible heat into latent heat, thereby exhausting the supercooling degree; and (3) Utilization, in which the high energy density of the resulting ice slurry enhances the dispatchability and efficiency of cooling processes.

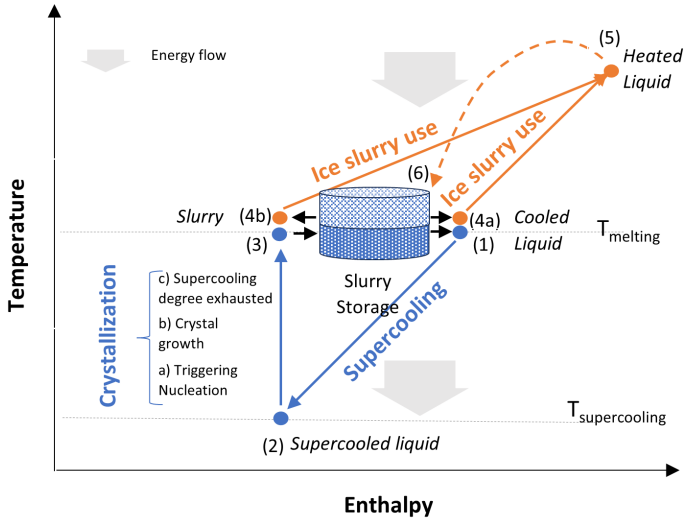

Figure 4: Supercooling ice slurry production method. Left: Thermodynamic cycle of the supercooling ice slurry production method process (blue) and potential applications of ice slurry (orange). The liquid stored at the melting temperature T_{melting} (1) is first supercooled to $T_{\text{supercooling}}$ (2). Within the crystallizer, nucleation and subsequent crystal growth occur, releasing the supercooling energy as latent heat. The resulting mixture of ice particles and water at T_{melting} is then collected in the ice slurry storage tank. By continuously repeating this cycle, the storage tank gradually fills until it reaches the maximum ice packing mass fraction limit (ca. 50 %). On the application side, the thermodynamic cycle illustrates two possible uses: either (4a) chilled water drawn from the ice slurry storage or (4b) the ice slurry itself as a secondary refrigerant are used for cooling applications (5). In closed-loop operation, those streams eventually return to the storage tank (6).

Figure 5 presents the main physical components of a supercooling ice slurry production system: the supercooler, a heat exchanger where the fluid (water, in this case) is cooled below its melting point (e.g., –2 °C); the in-stream ice crystallizer, where nucleation is induced and approximately 2.5 % of the water forms ice crystals, thereby releasing the latent energy (equal to the sensible supercooled amount); and the ice slurry storage, where the mixture is separated into water and ice slurry. A recirculation pump completes the circuit, progressively increasing the ice mass fraction in the storage tank up to 50 %.

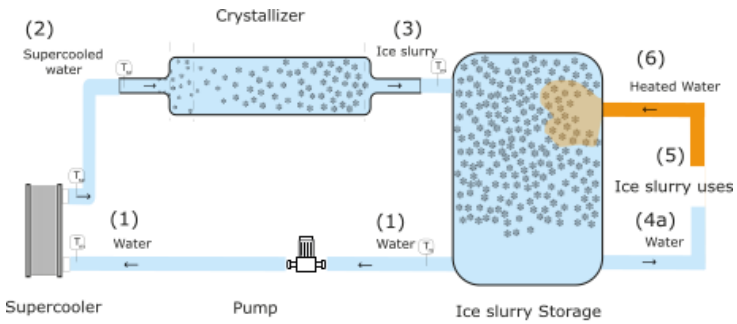

Figure 5: Supercooling ice slurry production method. Conceptual hydraulic scheme with the main physical components: supercooler, crystallizer, storage and recirculation pump.

Applications, target customers and barriers

Ice slurry systems are versatile thermal energy storage solutions that can be deployed across multiple sectors where cooling or low-temperature heat management is critical. They are particularly suitable for applications requiring cold storage around 0–15 °C range, enabling peak-shaving, load-shifting, and enhanced integration with renewable energy sources.

Industrial process cooling. Many industrial processes operate within the 0–15 °C range, including food and beverage production, dairy processing, pharmaceuticals, chemical manufacturing, and refrigerated logistics. In Europe, industrial cooling demand was approximately 99 TWh_e/year in 2012, with 83 TWh_e/year for process cooling and 16 TWh_e/year for space and air conditioning Fleiter et al.. About 54 % of this demand (46 TWh_e/year) falls in the 0–15 °C range, ideally suited for latent ice slurry storage Reitze. Assuming an EER of 2.5, this translates to roughly 115 TWh_h/year of thermal cooling energy, with an average daily requirement of 0.3 TWh_t/day. Storage for this demand would require approximately 6.8×10^6 m^3 of ice slurry, with an indicative market value of €3.3 billion, excluding chillers, installation, operation, and flexibility revenues.

Target customers are end-users or industrial energy system operators in the aforementioned sectors. Ice slurry systems allow reduction of peak chiller loads, downsizing of installed equipment, and load shifting to periods of lower electricity prices or higher on-site renewable generation.

Barriers include conservative investment practices, the lack of technology industrial adoption, limited familiarity with latent storage technologies, integration challenges with existing chillers, and regulatory/safety requirements.

Data center cooling. Data centers represent a rapidly growing segment in Europe, consuming between 40 TWh_e/year to 104 TWh_e/year, with 30–40% dedicated to cooling Kamiya and Coroamă. This corresponds, assuming a higher EER that compared to industry of 3.5 (due to higher evaporation temperatures) to an estimated 49 TWh_t/year to 127 TWh_t/year for cooling. This substantial cooling demand makes data centers a relevant target for ice slurry-based thermal storage solutions. Owing to their continuous 24/7 operation, cooling loads in data centers are highly stable, predictable. In this context, the primary value proposition of ice slurry integration is not peak load reduction, but rather increased operational flexibility and enhanced integration of renewable electricity. In particular, ice slurry storage enables the temporal decoupling of cooling production from IT heat rejection, allowing cooling energy to be generated during periods of high on-site photovoltaic production or low-carbon electricity availability and used when required. These characteristics make data centers well suited for controlled charging and discharging of latent thermal storage systems.

Target customers include data center operators, cloud service providers, and colocation facilities. Ice slurry systems can reduce peak electricity demand, enable load shifting, and improve overall energy efficiency by decoupling cooling production from IT heat generation.

Barriers include the requirement for extremely high reliability and uptime, integration with existing HVAC infrastructure, limited experience with latent storage in IT, and regulatory/safety considerations.

Residential solar-ice systems. In residential applications, ice slurry can serve as a thermal buffer between renewable heat sources (solar thermal collectors or photovoltaic electricity) and heat pumps. Solar-ice systems, such as those developed in TRI-HP EU projects, enable a cost-effective 80 % of local renewable heat production for space heating and domestic hot water demand in Central Europe climates Gurruchaga et al. (2023).

Target customers are homeowners, housing developers, and cooperatives seeking high renewable shares without requiring seasonal borehole storage.

Market barriers include availability of sun-exposed areas for solar thermal collectors and photovoltaic systems in high density areas, as well as a lack of previous implementation experience. Consequently, standardized system layouts and installation protocols are largely absent, slowing market adoption despite demonstrated technical feasibility.

District heating and cooling networks. Fifth-generation district heating and cooling (5GDHC) networks operate at low temperatures and increasingly rely on distributed sources such as waste heat, ambient heat, or solar energy. Ice slurry storage is attractive allowing shifting of heating/cooling availability and better integration of renewable/waste heat Shubert et al. (2020).

Target customers include network operators, municipalities, and urban developers.

Barriers include integration complexity, the need for coordination with other storage technologies, and, consequently, the requirement for advanced control strategies.

Table 2: Applications of ice slurry: target customers, market segments, and potential barriers.

Application	Target customers	Segment	Potential barriers
Industrial coooling (0–15 °C)	Food and beverage, pharmaceutical, chemical industries	Industrial	Integration with existing chillers; limited familiarity with latent storage technologies; regulatory and safety requirements; conservative investment practices; lack of technology adoption; and regulatory/safety requirement
Data centers	Operators, cloud service providers and colocation data centers	Industrial / IT	High reliability requirements; integration with existing HVAC; limited experience with latent storage; regulatory and safety considerations
Solar-ice residential systems	Homeowners, residential developers, housing cooperatives	Residential	Space constraints; social acceptance; high upfront costs; system complexity; lack of technology adoption
District heating and cooling networks	Network operators, municipalities, urban developers	Residential / Urban Planning	Coordination with other storage types; infrastructure constraints; need for advanced controls

Challenges for ice slurry by supercooling technology development and scale-up

The development and scale-up of ice slurry technology by supercooling method face several technical and operational challenges that must be addressed for widespread deployment. The supercooling ice slurry production method, which involves triggering nucleation in a supercooled water flow to release small ice particles, is particularly sensitive. Ensuring that the supercooling degree, the full sensible energy content, is completely converted into latent energy is essential to prevent unwanted ice formation upstream in pipelines or other system components.

Crystallizers are the key components where nucleation is triggered and ice crystal growth occurs. Despite the inherent instability ice formation and growth, crystallizers can be operated in a controlled and reliable manner, avoiding upstream ice propagation and minimizing exergetic losses.

While the physics of ice nucleation and growth under static conditions is relatively well understood, the behaviour of ice formation in dynamic supercooled flows remains less explored. Developing robust mathematical models to simulate ice nucleation, growth, and transport under realistic flow conditions is critical for proper scale-up, design optimization, and safe operation. Overcoming these challenges and mastering the formation and behaviour of supercooled ice slurries is precisely the goal of this project.

2 Objectives

ModIceCrys aims to understand the fundamentals of ice growth and its interactions with fluid flows. This know-how will be ultimately used to develop a flow-based ice crystallizer design tool by means of Computational Fluid Dynamics (CFD). Thus, a key aspect of the *ModIceCrys* project will be to numerically investigate ice crystallization processes in supercooling water flows. To validate the numerical model experimental assessment of ice crystallizers will be conducted.

The specific objectives of the project are:

1. Develop and validate a numerical model for ice growth to be implemented in the Population Based Equations (PBE).
2. Set-up and validate a Computational Fluid Dynamics (CFD) model of flow-based crystallizer designs without the ice crystallization process.
3. Develop a multi-scale numerical framework based on CFD coupled with PBE able to simulate the fluid flow behaviour, ice crystallization process and ice crystal growth.
4. Experimentally evaluate two crystallizer designs to validate the CFD model.

3 Work carried out

3.1 Introduction

During 2025, the work carried out within the project *ModIceCrys* project has been actively structured around three main axes: modelling, experimentation, and publication activities.

Modelling activities

From the modelling activities, several key tasks were completed to consolidate and strengthen the CFD–PBM framework:

- Additional independent validations and comparisons of the CFD–PBM model with real experimental data and other CFD numerical models, respectively, were carried out.
- The model was further developed and adapted to the specific geometry and operating conditions of the project's crystallizer, and has been prepared for validation against experimental data to be generated during the 2025–2026 experimental campaign.

Experimental activities

From an experimental perspective, the test facility was extensively upgraded and reconfigured to support the upcoming campaign, which included both energy efficiency measurements and visualisation techniques. The layout of the crystallizer, cameras, and supporting structures was redesigned to optimise optical access for high-speed imaging, while mitigating technical issues such as condensation on cold surfaces that could compromise visualisation quality. Several strategies were explored, including enclosing the setup within a dehumidified greenhouse and integrating airflow systems to reduce surface moisture.

As part of this reorganisation, the inlet and outlet piping of the crystallizer, its connections to the supercooler and ice slurry storage, and all support elements were redesigned and rebuilt. Independent support structures for both the crystallizer and the visualisation system were implemented to minimise vibrations and ensure stable and flexible experimental conditions. The ice slurry storage system was also relocated and enlarged to enable longer experimental runs without interruptions. In parallel, the cooling and heating generation systems, pumping and hydraulics, and the control and data acquisition systems were thoroughly reviewed and updated to guarantee full compatibility with the aforementioned changes.

During the second half of 2025, a first series of tests was conducted to evaluate the effectiveness of the Backlight Shadow Imaging (BSI) technique for ice slurry visualisation. Although the results did not yet yield sufficiently clear data to fully validate the CFD–PBM model, they provided valuable insights for redesigning the experimental approach. In particular, the tests highlighted the need for alternative "crystallizer" designs and improved optical access to obtain more representative and reliable experimental data.

It is important to emphasise that the ultimate objective of this work is to use the data from these experiments as a reliable basis for validating the CFD–PBM model.

Publications

In parallel, a scientific article titled *"Comparative Analysis of Three Ice Slurry Production Methods for Thermal Energy Storage Enabling Dispatchability in Industrial Cooling Demands"* has been submitted to the Journal of Energy Storage and is currently under peer review.

In the following sections, a summary of the investigations and progress for each topic is provided.

3.2 CFD-PBM model development

As previously explained, ice slurry is a mixture of small ice particles immersed in water. The interaction between the water and the solid ice particles involves heat and mass transfer through phase change mechanisms, as well as momentum transfer due to forces between the two phases or inelastic collisions between the ice particles themselves or with the domain boundaries.

In CFD, ice slurry is modelled as a two-phase flow, where the water (liquid) is treated as a continuous phase and the ice particles (solid) as a discrete phase. Both phases interact with each other through processes of mass, momentum, and energy transfer. For the ice content considered in this study (in any event below 60 %), the solid ice particles are treated as a dense discrete phase within the fluid flow.

The fundamental governing equations of fluid dynamics, the conservation equations of mass, momentum, and energy, as well as the Population Balance Model (PBM) incorporated to describe the evolution of the particle size distribution, involves an extensive mathematical formulation, which detailed description of the coupled CFD–PBM modelling framework is comprehensively documented in annexes (Sec. 7).

3.3 CFD-PBM model simulation

For preliminary model validation, experimental data from previously published studies were used Niezgoda-Żelasko (2006), Niezgoda-Żelasko and Zalewski (2006), Sari et al. (2000), Vuarnoz et al. (2002). These data provided an initial basis to conduct a preliminary validation of the multi-scale CFD–PBM model of the velocity and pressure drops of the ice slurry flows. In addition, the CFD–PBM results reported by Du et al. (2023) were used to perform a comparative analysis between modelling approaches, allowing for a broader evaluation of the CFD-PBM model developed.

However, this validation remains necessarily partial, as the available experimental measurements are largely limited to velocity fields, pressure drops, and volume fraction distributions, without detailed information on particle size distributions. A comprehensive and robust validation of the model will only be possible with the experimental data generated within the *ModIceCrys* project. Nevertheless, this initial comparison represents a crucial step towards establishing a more reliable and physically consistent modelling framework.

The preliminary results obtained from the coupled CFD–PBM model for these three experimental case studies are presented in the following sections.

3.3.1 CFD-PBM model Example-01

Introduction

The analysis of Vuarnoz et al. (2002) aimed to investigate the flow patterns of an ice slurry mixture in a horizontal pipe as a function of the mass flow and resulting type of flow inside the pipe (laminar, transitional or turbulent flow). The experimental results were limited to the vertical and horizontal velocity profiles inside a horizontal pipe of 23 mm diameter and 1.3 m length. To measure the velocity profiles, they applied a non-invasive technique using an ultrasonic analyser. The ice slurry was a mixture of 10.3 % ethanol-water solution. The initial ice solid phase volume fraction was 7.5 % and 16 %, depending on the case. Different inlet mass flow rates ($0.5\,\mathrm{kg\,s^{-1}}$, $0.21\,\mathrm{kg\,s^{-1}}$, $0.09\,\mathrm{kg\,s^{-1}}$, $0.06\,\mathrm{kg\,s^{-1}}$) were tested to evaluate the different profiles generated by different multiphase flow patterns. The vertical and horizontal velocity distribution profiles obtained by the experiment are shown in Fig. 6.

Modelling

A structured *O-Grid* mesh, as shown in Fig. 7, was employed to enhance convergence and improve accuracy.

An independence analysis of the mesh was conducted using three discretization meshes with 0.65 M, 1.326 M and 4.8 M (where M stands for million) cells, with the intermediate mesh of 1.326 M being selected throughout a mesh quality analysis that evaluated the independence of results as a function of the number of elements. The final mesh has a general cell size of 1 mm, and various methods were applied to the mesh to capture the boundary effects of the domain, mainly the walls. The resulting *O-Grid* mesh yields the following mean quality indicators: *orthogonality* 0.96 and *skewness* 0.09, which are considered well.

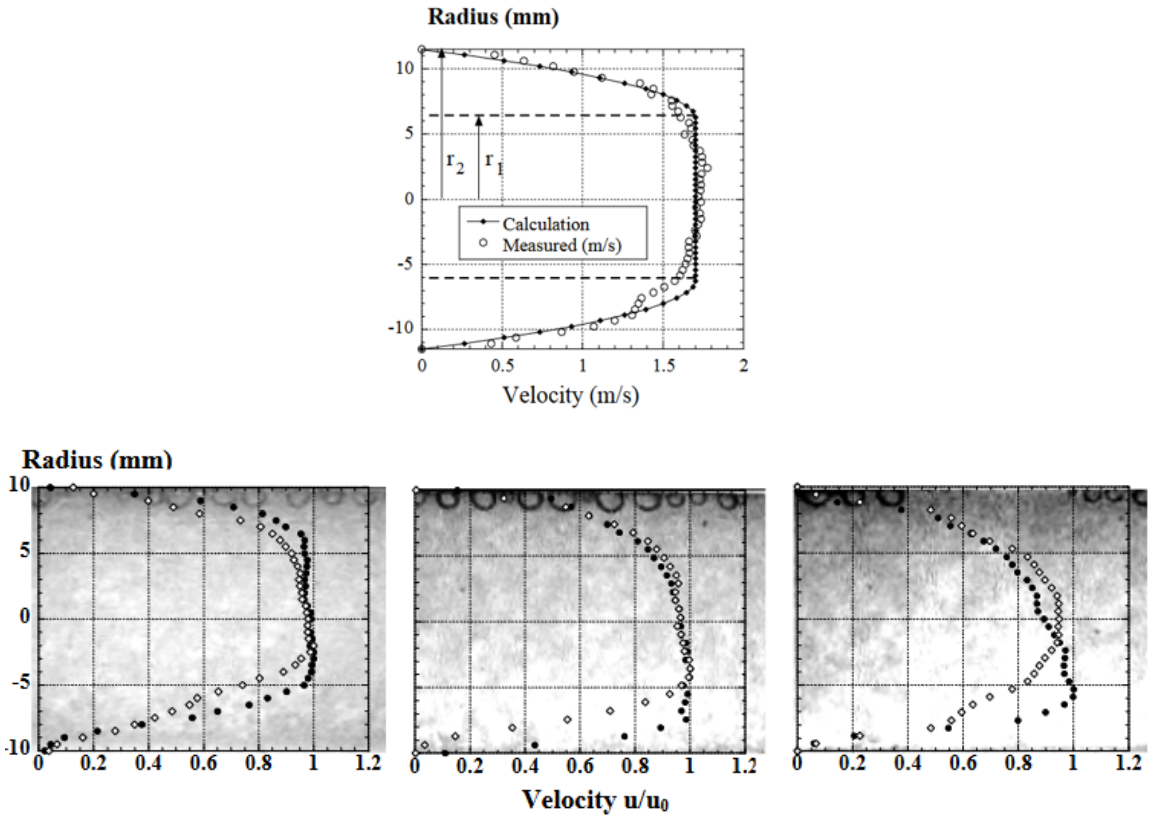

Figure 6: Top: Vertical velocity profile for $0.5\,\mathrm{kg\,s^{-1}}$. Down: Vertical and horizontal velocity profile for different flow rates obtained. From the left to the right: $0.21\,\mathrm{kg\,s^{-1}}$, $0.09\,\mathrm{kg\,s^{-1}}$, $0.06\,\mathrm{kg\,s^{-1}}$. Black markers show vertical profiles, and white ones belong to horizontal profiles. In the background, ice slurry particles flowing through the tube can be recognized. Source: Vuarnoz et al. (2002).

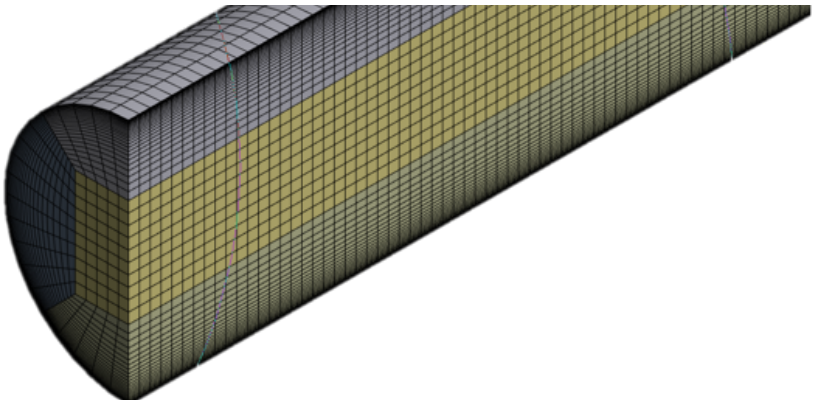

Figure 7: Structured *O-Grid* mesh used the multi-scale CFD coupled with PBE model simulations.

A three-dimensional, multiphase simulation was conducted, relying on the mass conservation (Sec. 7.2.1), momentum conservation (Sec. 7.2.2) and energy conservation (Sec. 7.2.5) fundamental physics principles. The $k-\epsilon$ *mixture* turbulence model with enhanced Wall Treatment, referred to in Sec. 7.2.6, was considered for the model. The sections reported above (as well as those below within this subsection) refer from previous yearly report of ModIceCrys Gurruchaga and Carbonell (2024).

An *Eulerian* multiphase model composed of two phases, liquid and solid, of the ethanol-water mixture is assumed. Buoyancy effects, relaying the different densities that have to be assumed for each of the phases, and an implicit volume fraction formulation of the two phases are considered.

The kinetic theory of granular flows (Sec. 7.2.8) is incorporated in the mathematical formulation. The momentum exchange between phases, with the drag force, employing the *Syamlal-O'Brien* model described in Sec. 7.2.4, are also modelled. For the heat transfer between phases, the correlation for the Nusselt described in Sec. 7.2.7 is chosen.

The mass transfer process is governed by the general expression of the PBE described in Sec. 7.3.2. For this modelling, the nucleation (Sec. 7.3.6) and growth rate (Sec. 7.3.3) were not necessary to be implemented[3]. For the aggregation term, a turbulent aggregation kernel, which includes the particle aggregation via the viscous and the inertial mechanisms, was introduced as detailed in Sec. 7.3.4. For the breakage term, *Ghadiri* kernel model for solids particles, following what is indicated in Sec. 7.3.5 is considered.

For the simulation with a higher flow rate ($0.5\,\mathrm{kg\,s^{-1}}$), the steady-state approach was sufficient to solve the coupled CFD-PBE model. However, due to the physical nature of the case with lower flow ($0.06\,\mathrm{kg\,s^{-1}}$), which involved a pulsating and unstable flow, the coupled CFD and PBE simulation had to be conducted through a transient simulation approach.

Results and comparison

As shown in Fig. 8, for the higher flow rate ($0.5\,\mathrm{kg\,s^{-1}}$), the velocity along the vertical axis of the pipe exhibits an approximately symmetrical distribution.

The mean absolute percentage $error$ (MAPE) between the experimental results from Vuarnoz et al. (2002) and the numerical simulation from Du referred in Du et al. (2023) is approximately 9 %, consistent with our analysis of the processing of the digitized graphs (8.2 % - 10.9 %, depending on whether or not the two extreme points of the velocity profile are considered or not). The model developed within the *ModIceCrys* project, depicted in blue in Fig. 8, has a better approach to the experimental results from Vuarnoz et al. (2002) with a MAPE (8.1 % - 10.8 %) improving the numerical model developed in Du et al. (2023).

Although, based on the Fig. 8, for the case of flow of $0.5\,\mathrm{kg\,s^{-1}}$, it could be argued that our CFD-PBM model is capable of accurately capturing the variation in ice slurry velocity, the validation of the model representing ice slurry under conditions of low ice content and high flow rate (high velocity, high turbulence, and high dispersion of the solid particle phase) is not highly representative. To better validate the model, it is preferable to expose it to more complex hydrodynamic situations and interactions between the liquid and solid phases, such as a pulsating slug flow. For this reason, an additional case at a low flow rate ($0.06\,\mathrm{kg\,s^{-1}}$), also included in Vuarnoz et al. (2002), is simulated.

For the lower flow rate ($0.06\,\mathrm{kg\,s^{-1}}$), the velocity along the horizontal axis of the pipe exhibits an approximately symmetrical distribution, as shown in the left-hand side of Fig. 9. The velocity along the vertical axis of the pipe on the right-hand side of Fig. 9 exhibits an asymmetrical distribution consistent with the experimental data of the right bottom of Fig. 6. Despite the differences between the experimental data and our model are higher for this case, the model is capturing the expected behaviour of the ice slurry flow rate. However, it is unclear whether this discrepancy arises from the model itself or from the uncertainties in the experimental procedure and results, including whether the measurement method used captured the velocity of the solid or liquid phase of the two-phase flow, which could explain the significant difference in the comparison between the experimental data and the model.

In Fig. 10 and Fig. 11 two different flow cases are depicted: higher flow regime at $0.5\,\mathrm{kg\,s^{-1}}$ and the lower flow regime at $0.06\,\mathrm{kg\,s^{-1}}$. For the turbulence flow, the volume fraction of solid ice particles is slightly concentrated in the upper midsection of the pipe due to buoyancy effects, but mostly distributed across the entire cross-section, while for the lower flow, the volume fraction of solid ice particles is progressively

[3] This simplification will not be possible for the modelling of the crystallizer foreseen in the project.

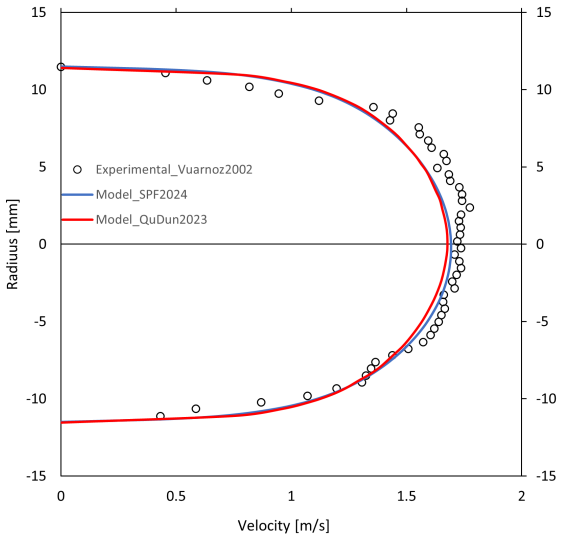

Figure 8: Results from the vertical velocity profile for the 0.5 kg s^{-1}. White circle marks show vertical velocity profiles obtained experimentally by Vuarnoz et al. (2002). The red line corresponds to the vertical velocity profile obtained in Du et al. (2023). In blue, the vertical velocity profile obtained by the *ModIceCrys* model.

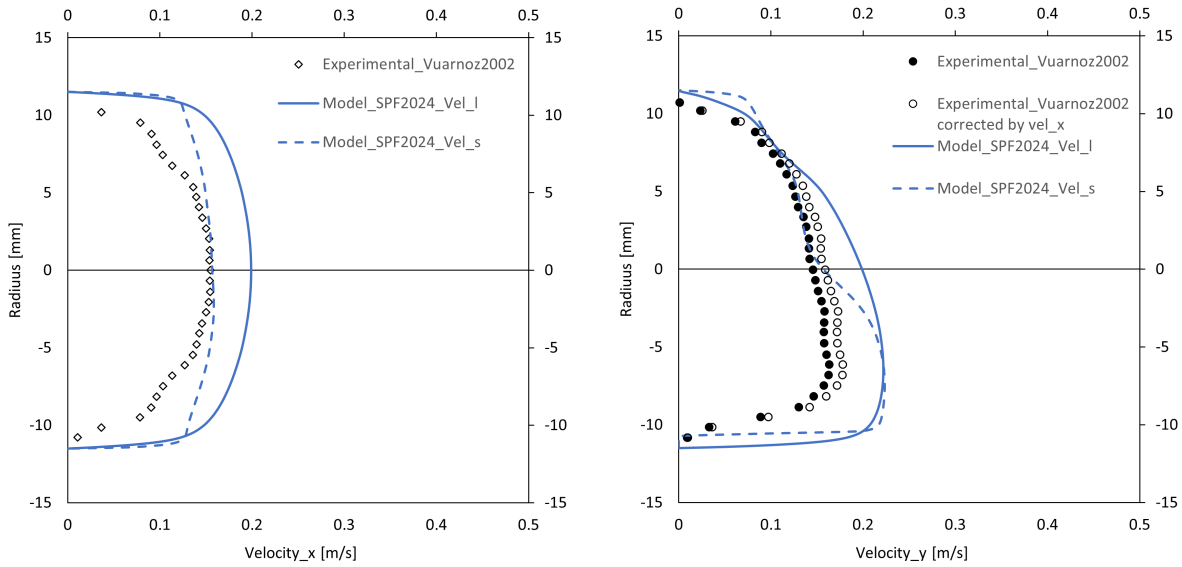

Figure 9: Results from the horizontal and vertical velocity profiles for the pulsating slug flow of 0.06 kg s^{-1}. On the left, white pointers show horizontal velocity profiles obtained by Vuarnoz et al. (2002). The blue continuous line corresponds to the liquid-phase horizontal velocity profile obtained by the model developed within the *ModIceCrys* project. The dashed blue line corresponds to the solid-phase horizontal velocity profile. On the right: white circle marks show vertical velocity profiles obtained by Vuarnoz et al. (2002). The black markers are vertical velocity profiles obtained by Vuarnoz et al. (2002) but displacing the velocity profile so that $u_{x,x=0} = u_{y,y=0}$. The blue continuous line corresponds to the liquid phase while the dashed blue line corresponds to the solid phase vertical velocity profile obtained by our model.

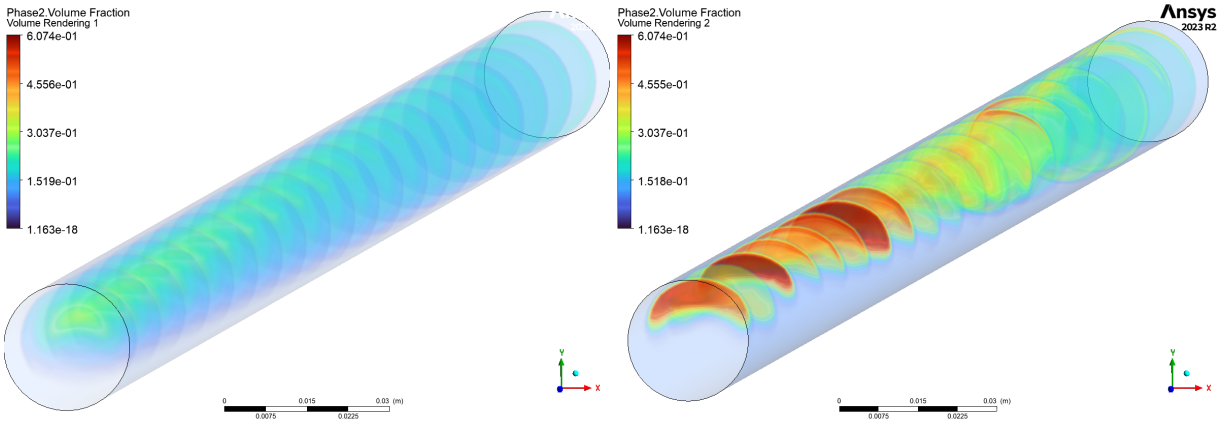

Figure 10: Results from the CFD and PBM *ModIceCrys* model for the Phase 2 volume fraction (ice particles) in different sections of the pipe, flowing from the top right to the bottom left. The left plot presents the turbulence flow at $0.5\,\mathrm{kg\,s^{-1}}$. For this case, the volume fraction of solid ice particles is slightly concentrated in the upper midsection of the pipe due to buoyancy effects. The right figure presents the lower flow at $0.06\,\mathrm{kg\,s^{-1}}$. For this case, the volume fraction of solid ice particles progressively concentrates at the top of the pipe due to buoyancy effects between the two phases, leaving no ice particles in the lower midsection of the outlet.

concentrated at the top of the pipe due to buoyancy effects between the two phases, leaving no ice particles in the lower midsection in the outlet.

The uneven distribution of solid ice particles influences the velocity profile, as the particles introduce resistance to the free stream of the fluid. In higher flow, where particles are more uniformly distributed, a symmetric vertical velocity profile is maintained. However, under slower velocity conditions, buoyant accumulation of particles at the top of the pipe reduces the velocity in the upper section while accelerating the flow in the shrunk lower section. Additionally, as observed in Fig. 12, certain regions accumulate ice particles, resulting in partial flow blockages and, consequently, the generation of a pulsating flow.

Conclusion

Two different scenarios of ice-slurry fluid flow patterns have been used to validate the CFD-PBM model developed within *ModIceCrys*. In the first scenario, which involves higher turbulent ice slurry flow, the differences between the CFD-PBM model and experimental results were even smaller than those observed in the model evaluation conducted in Du et al. (2023). For the case of low ice slurry flow, which generated challenging-to-predict pulsating slug flow conditions, a transient simulation was performed with good agreement, indicating that the model qualitatively captures the expected behaviour of the ice slurry flow rate. However, the discrepancies between the experimental results and the model (Fig. 9) remain unclear, as it is uncertain whether they stem from the model itself or uncertainties in the experimental procedure.

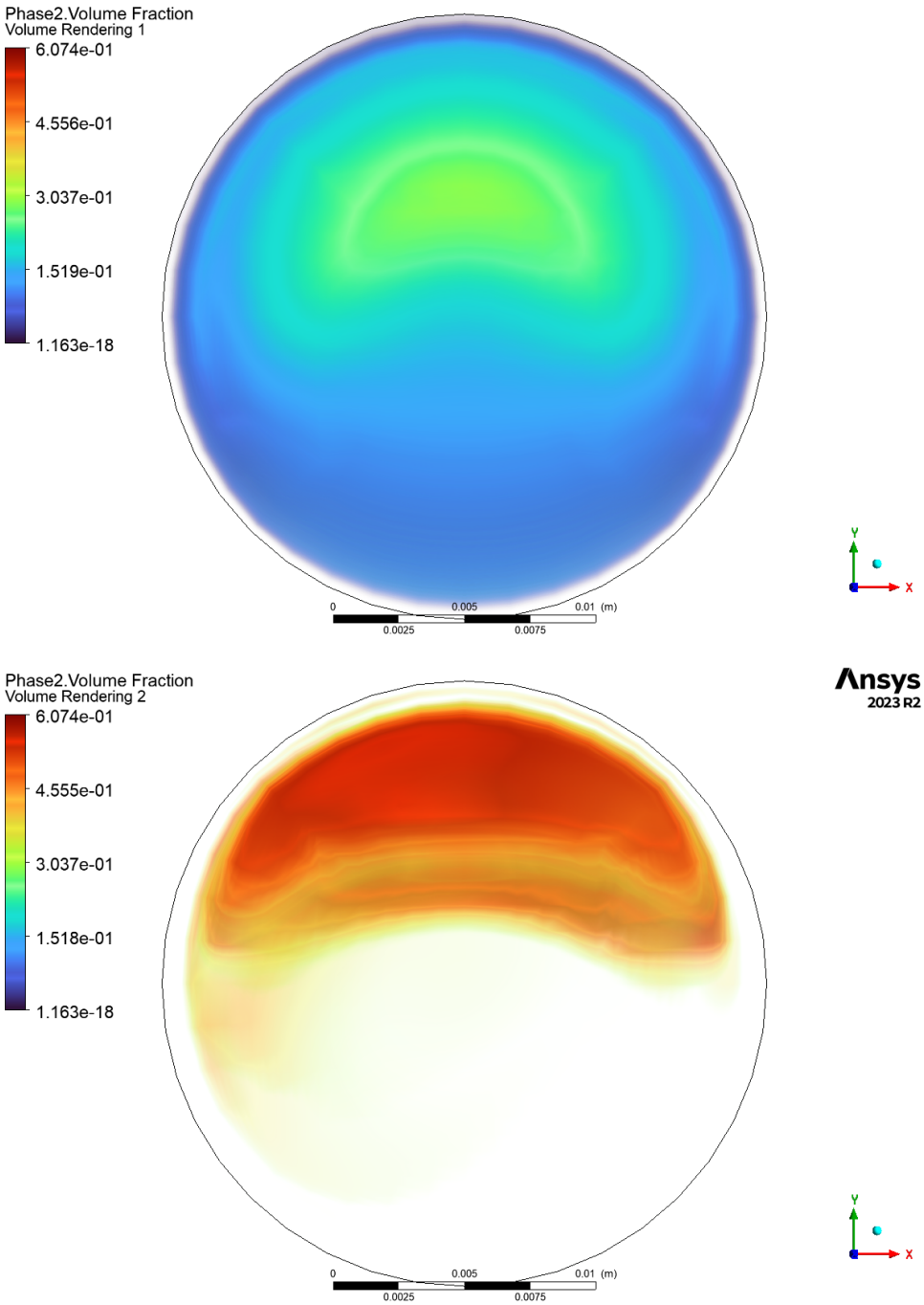

Figure 11: Results from the CFD and PBM *ModIceCrys* model for the Phase 2 volume fraction (ice particles) at the outlet section of the flow at 0.5 $\mathrm{kg\,s^{-1}}$ left and 0.06 $\mathrm{kg\,s^{-1}}$ right are presented. In the top figure, presenting the higher flow, the volume fraction of solid ice particles is more or less distributed along the cross-section with some slight concentration in the upper midsection, while in the bottom figure, depicting the lower (and pulsating slug) flow, the volume fraction of solid ice particles is highly concentrated at the top of the pipe due to buoyancy effects between the two phases.

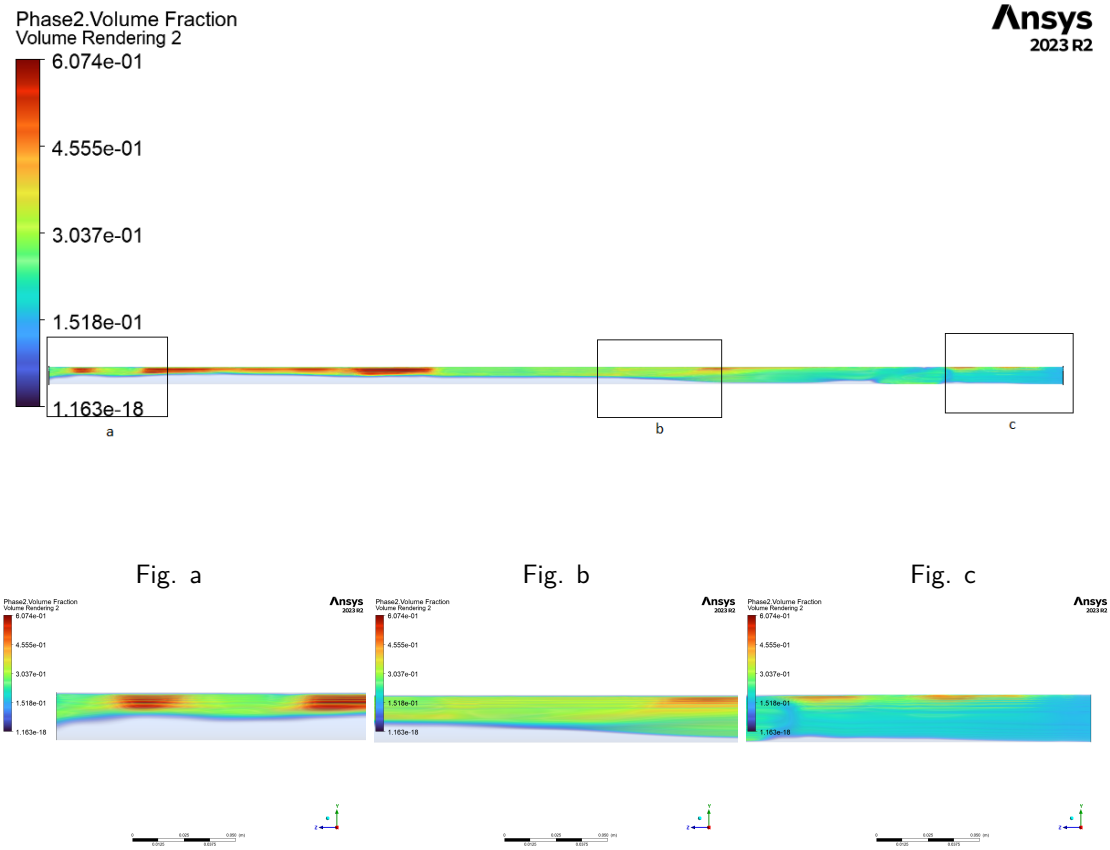

Figure 12: Results from the CFD and PBM *ModIceCrys* model for the Phase 2 volume fraction (ice particles) in different sections of the pulsating slug flow at 0.06 kg s^{-1} are presented. In the top figure, the general view of the ice slurry flow domain is shown, flowing from right to left, with three regions of interest: (a) outlet, (b) intermediate, and (c) inlet. In the bottom right Fig. c, a uniform distribution of the ice slurry volume fraction is observed at the flow inlet. In the bottom middle Fig. b (intermediate region), the ice slurry flow is displaced to the top of the pipe due to buoyancy. In the bottom left Fig. a, clear concentration spots of ice particles on the top of the pipe section are observed at the outlet, typical of a pulsating slug flow.

3.3.2 CFD-PBM model Example-02

Introduction

The analysis of Niezgoda-Żelasko and Zalewski (2006) focused on understanding ice slurry flow in horizontal pipes, particularly how variations in mass flow and ice content affect the flow regime (laminar, transitional, or turbulent). Experiments showed that ice slurry at higher ice fractions behaves as a non-Newtonian Bingham fluid, characterised by a yield shear stress and plastic viscosity. Increasing the solid fraction delays the onset of turbulence, effectively "laminarizing" the flow by absorbing part of the fluid's turbulence kinetic energy.

A second paper from Niezgoda-Zelasko from the same year (Niezgoda-Żelasko (2006)) investigates heat transfer in ice slurry flowing through horizontal tubes. The paper also explores modelling heat transfer in ice slurry flows using CFD, employing a single-phase Bingham fluid approach combined with the enthalpy–porosity method for melting and considering variable thermal conductivity in the moving suspension.

The test stand enabled precise measurement of thermal and flow parameters using a 4.6 m exchangeable pipe segment, sufficient for fully developed flow in tubes of various diameters. Heat was applied via a uniformly wrapped heating cable, and measurements were collected using temperature sensors and differential pressure transducers. The ice mass fraction was determined continuously using combined temperature and density

measurements.

Experiments were performed in copper tubes of various inner diameters, with focus here on the 0.016 m tube. Mean flow velocities ranged from 0.1 m s^{-1} to 4.5 m s^{-1}, and ice mass fractions varied from 0 % to 30 %, with an average ice crystal size of 100 µm to 150 µm. Applied heat was 5000 W m^{-2} along the second half of the pipe.

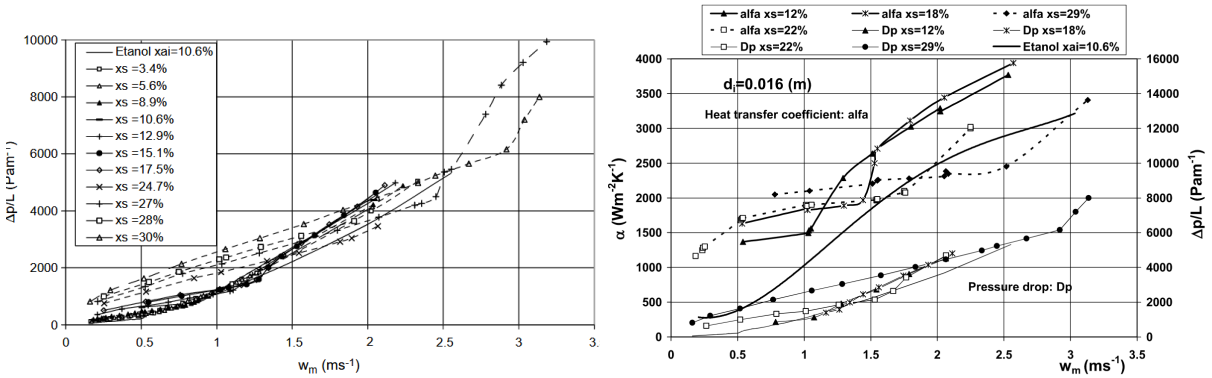

Figure 13: Top: Pressure drop (ΔP/L) as a function of mean velocity of the ice slurry flow for pipe diameter 0.016 m. Bottom: Local heat transfer coefficient (α in the figure, h_{x0} in this report) and pressure drop (ΔP/L) as a function of mean velocity of the ice slurry flow for pipe diameter 0.016 m. Source: Niezgoda-Żelasko and Zalewski (2006) and (Niezgoda-Żelasko (2006)).

Modelling

A similar approach, a structured *O-Grid* mesh, similar to shown in Fig. 7, for a the 0.016 m diameter and 4.6 m length pipe was employed to enhance convergence and improve accuracy.

As in Example-01, a three-dimensional multiphase simulation was conducted based on the fundamental conservation laws of mass, momentum, and energy (Secs. 7.2.1, 7.2.2, 7.2.5). Turbulence was modelled using the k–ϵ *mixture* approach with enhanced Wall Treatment (Sec. 7.2.6). The system employed an Eulerian two-phase representation, consisting of a liquid and a solid phase of the 10.3 % ethanol-water mixture. Buoyancy effects resulting from density differences between phases were included, and an implicit volume fraction formulation tracked the distribution of each phase.

Particle behaviour was described using the kinetic theory of granular flows (Sec. 7.2.8). Momentum exchange between phases was modelled through a drag force using the *Syamlal-O'Brien* correlation (Sec. 7.2.4), while heat transfer between phases was evaluated using an interphase Nusselt correlation (Sec. 7.2.7).

Mass transfer between the solid and liquid phases, mainly governed by ice melting (with crystallisation also considered), was implemented through an User-Defined Function (UDF) instead of a PBM, as the model focuses on fusion rather than crystal growth. The phase change rate, $\dot{m}_{ls}$ in kg s^{-1}, was calculated based on the local temperatures of the liquid phase (T_l) and solid phase (T_s) relative to the melting temperature (T_m):

$$\dot{m}_{ls} = \begin{cases} -\dfrac{h_{sl}\ \max(0, T_l - T_s)}{h_{fus}}, & T_s > T_m \quad \text{(melting)} \\ \dfrac{h_{sl}\ \max(0, T_s - T_l)}{h_{fus}}, & T_l < T_m - \Delta T_{hist} \quad \text{(crystallization)} \\ 0, & \text{otherwise} \end{cases} \tag{1}$$

where h_{sl} is the volumetric heat transfer coefficient in W K^{-1} m^{-3} (evaluated using the Gunn correlation Gunn (1978)), h_{fus} is the latent heat of fusion in J kg^{-1} K^{-1}, and ΔT_{hist} is a hysteresis term to prevent numerical oscillations.

To correctly evaluate the heat transfer in the near-wall region, an additional UDF was implemented to adjust thermophysical properties of the liquid and solid phases within the ice slurry mixture, as during heat

transfer, the wall heat flux is primarily absorbed by the liquid phase, due to solid particles are only in point contact with the tube wall. The absorbed heat is then transferred from the wall to the liquid, and from the liquid to the solid particles located in the near-wall layer. To represent this mechanism, the thermal conductivity of the solid phase in the near-wall region was modified following Legawiec and Ziólkowski (1994) cited by Xie et al. (2023) and Cai et al. (2023). The effective thermal conductivities of the liquid and solid phases ($k_{\text{eff},l}$, $k_{\text{eff},s}$) depend on the local solid volume fraction α_s and differ between the near-wall and core regions.

The implemented UDF reads the local cell temperatures (T_l, T_s), the phase volume fractions (α_l, α_s), and the particle characteristic size, simplified to a one-dimensional diameter (d_s).

The thermal conductivities of the liquid and solid phases (λ_l, λ_s), expressed in $\mathrm{W\,m^{-1}\,K^{-1}}$, were defined within the UDF as temperature-dependent functions for the 10.3 % ethanol-water mixture:

$$\lambda_l = 0.5034 + 0.00127\,(T_l - 273.15) \tag{2}$$

$$\lambda_s = 2.21 - 0.012\,(T_s - 273.15) \tag{3}$$

where T_l and T_s (in K) denote the local cell temperatures of the liquid and solid phases, respectively.

The auxiliary parameters A, S and B used in the auxiliary functions are computed as:

$$A = \frac{\lambda_s}{\lambda_l} \tag{4}$$

$$S = \frac{2\,l_w}{d_s} \tag{5}$$

$$B = \begin{cases} 1.25\left(\frac{\alpha_s}{\alpha_l}\right)^{10/9} & \alpha_l > 10^{-6} \\ 1.25 & \text{otherwise} \end{cases} \tag{6}$$

where A is the ratio of solid to liquid thermal conductivity, reflecting the relative ability of the solid phase (ice) to conduct heat compared to the liquid. It modulates the contribution of the solid particles to the effective thermal conductivity. l_w in m is the thickness of the near-wall layer and S is a parameter that compares the distance to the near-wall to the particle diameter, indicating how many particles occupy the near-wall region and thus the extent of solid-liquid interaction influencing heat transfer near the wall. B is a function of the local solid-to-liquid volume fraction and represents the effect of particle concentration on the effective thermal conductivity in the core region, accounting for interactions between neighbouring solid particles.

The auxiliary functions are:

$$\phi(A,S) = \left(\frac{A}{A-1}\right)^2 \left[\left(1 - \frac{1-S}{A}\right)\ln A - \frac{A-1}{A}\,S\right] \tag{7}$$

$$K(A,B) = \frac{1}{1-B/A}\left[\frac{A-1}{(1-B/A)^2}\left(\frac{B}{A}\right)\ln\left(\frac{A}{B}\right) - \frac{B-1}{1-B/A} - \frac{1}{2}(1+B)\right] \tag{8}$$

The effective thermal conductivities implemented in the UDF are:

- Near-wall region ($S/2 \le 0.5$):

$$k_{\text{eff},l} = \lambda_l\,\alpha_l \tag{9}$$

$$k_{\text{eff},s} = 3\,\lambda_l\,\alpha_l\,S\,\phi(A,S) \tag{10}$$

- Core region ($S/2 > 0.5$):

$$k_{\text{eff},l} = \lambda_l\left(1 - \alpha_s^{1/2}\right) \tag{11}$$

$$k_{\text{eff},s} = \lambda_l\,\alpha_s^{1/2}\left(A\,\beta + (1-\beta)\,K\right) \tag{12}$$

where $\beta = 7.26 \cdot 10^{-3}$.

It should be noted that this part of the model remains unresolved, as the formulations in the literature exhibit significant inconsistencies between different versions of the same expressions. In particular, the expressions for the function ϕ (Eq. 7) differ between the consulted references Legawiec and Ziólkowski (1994), as cited in Xie et al. (2023), and Cai et al. (2023). These discrepancies include variations in the placement of parentheses and in the structure of certain quotients, which inevitably lead to different numerical results.

Determining the most appropriate formulation for the present case remains an open task and will constitute part of the research work planned for the coming months.

For the simulation, the steady-state approach was sufficient to solve the CFD model by means of the COUPLED method for pressure-velocity coupling together with volume fractions.

Results and comparison

As shown in Fig. 14, the comparison between the experimental data of Niezgoda-Żelasko and the model predictions for different ice volume fractions (13 %, 19.4 % and 23.7 %), the correlation between pressure drop and flow velocity is generally satisfactory. The associated errors remain below approximately 7 % for low ice fractions and increase moderately (up to 15 %) at higher solid concentrations.

However, the main discrepancy between the experimental results and the numerical model appears in the prediction of the local heat transfer coefficient (h_{x0}) in $\mathrm{W\,m^{-2}\,K^{-1}}$, as illustrated in the right graphs from Fig. 14. The model only reproduces reasonable values at very low velocities, i.e. under laminar flow conditions, while the predictions deviate significantly under turbulent regimes. This discrepancy, which needs to be addressed in the next phase of the work, might be attributed to inconsistencies in the formulations of the effective thermal conductivities found in the literature of the different authors mentioned before. Therefore, further investigation is required to determine the correct and physically consistent formulation of the effective heat transfer coefficients of the model.

Fig. 15 shows, on left-hand figures, the distribution of the ice volume fraction along the vertical y-axis at different longitudinal positions (z=0.3, 1.3, 2.3, 2.6, 3.6 and 4.6 m) of the pipe, allowing the vertical concentration profile to be visualised along the pipe. The corresponding volume fraction coloured field distribution at the pipe outlet (right-hand figures) represents the same distribution at the outlet ($z = 4.6$ m). Note that the scales used in the x–y plots (left-hand figures) are different for the two cases; this adjustment was made to improve readability.

The upper figures correspond to a flow velocity of $0.5\,\mathrm{m\,s^{-1}}$, while the lower figures represent the case with $2.5\,\mathrm{m\,s^{-1}}$. At the lower velocity, a strong accumulation of ice particles near the upper region of the pipe is observed, with local ice fractions reaching values close to 30 %. This behaviour is primarily driven by buoyancy effects under laminar flow conditions. In contrast, at higher velocities, where turbulence is significantly stronger, the ice phase becomes well mixed and uniformly distributed across the cross-section, with ice fractions stabilising around 12–13 %. In this case, turbulence flattens the vertical distribution and homogenises the ice concentration.

These distributions are consistent with experimental observations reported in the literature as well as with trends obtained in other numerical studies.

Conclusion

The comparison between the experimental data of Niezgoda-Żelasko and the model simulation results shows that the numerical model captures the overall trends in pressure drop and flow behaviour with reasonable accuracy. Pressure drop errors remain approximately 10 % for low ice fractions and increase moderately at higher solid concentrations, indicating good agreement in terms of momentum transfer.

Additionally, the simulated ice distribution along the pipe shows that at low velocities, buoyancy dominates, leading to strong accumulation near the top of the pipe, whereas at higher velocities turbulence flattens the distribution and homogenises the ice phase. These observations are consistent with experimental results and other numerical studies.

The main limitation of the current model lies in the prediction of the local heat-transfer coefficient (h_{x0}). As observed in Fig. 14, the model reproduces realistic values only at low velocities under laminar flow conditions, while significant deviations appear in turbulent regimes. This discrepancy is likely related to inconsistencies in

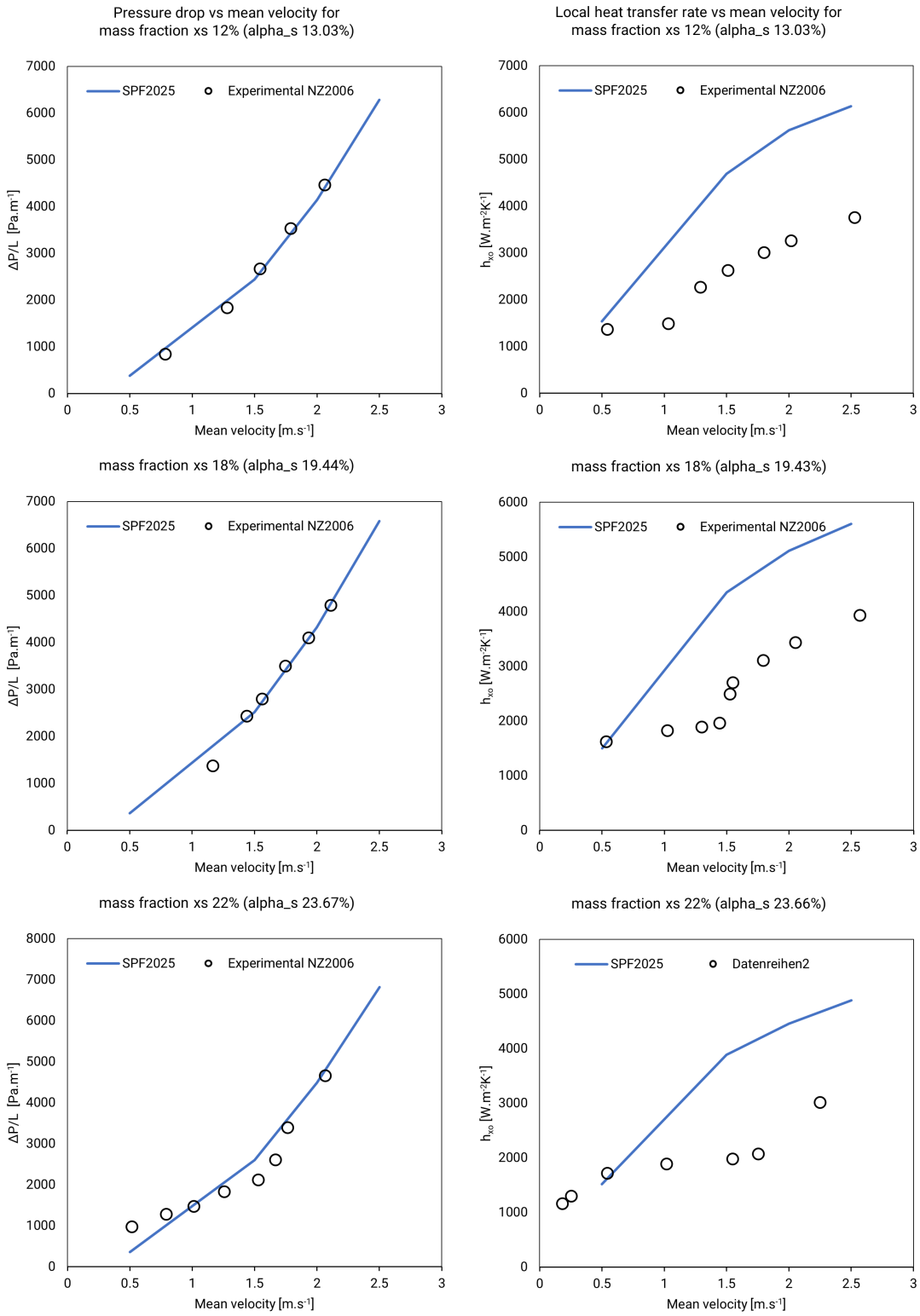

Figure 14: Results from pressure drop (left) and local heat transfer coefficient (right) vs mean velocity for different ice volume fractions obtained by Niezgoda-Żelasko and Zalewski (2006). The blue continuous line corresponds to the results obtained by the model developed within the *ModIceCrys* project. White circle marks show experimental results shown in 13.

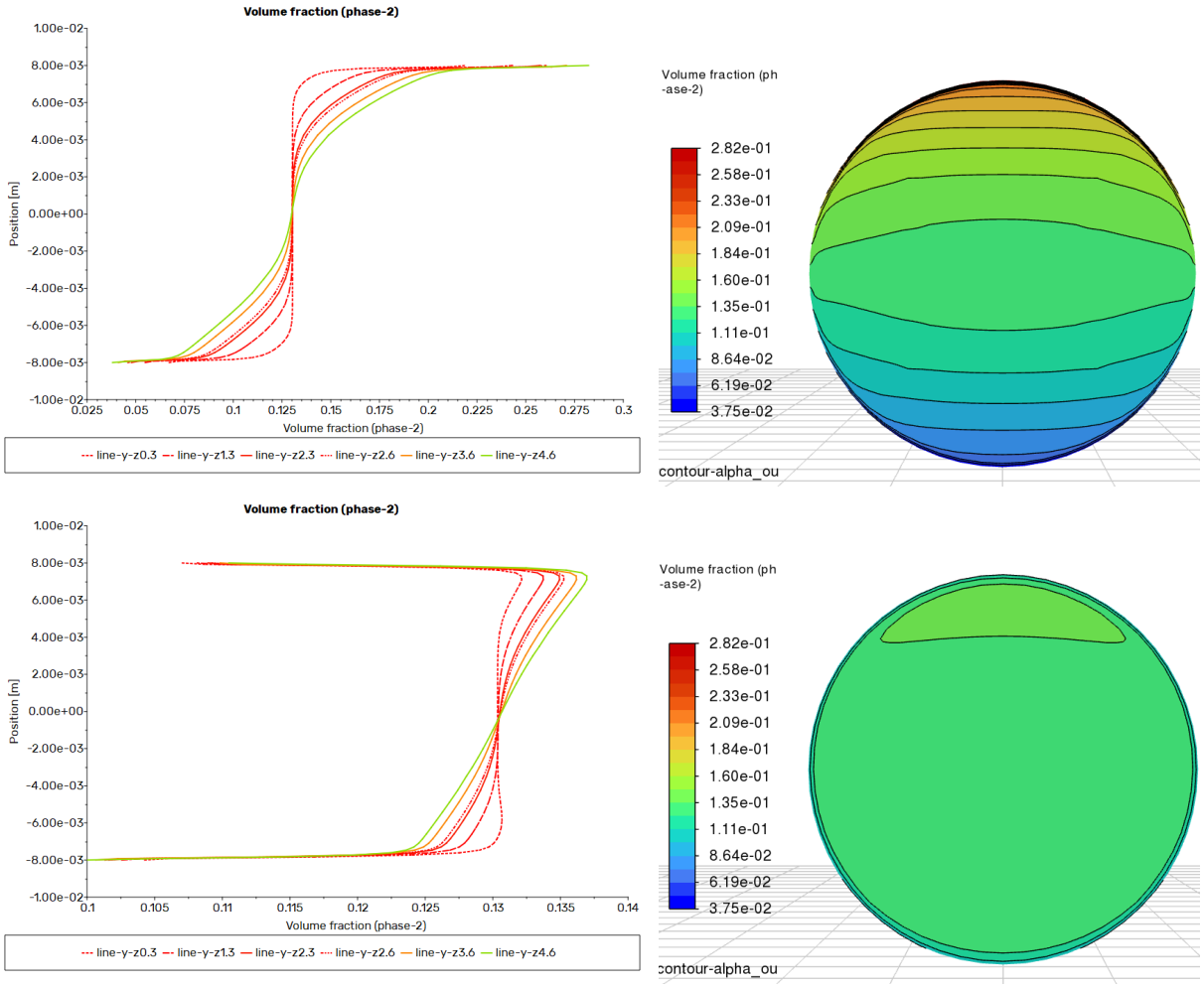

Figure 15: Left: Ice volume fraction distribution along the vertical y-axis at different longitudinal positions ($z = 0.3, 1.3, 2.3, 2.6, 3.6, 4.6$ m) along the pipe. Right: Ice volume fraction distribution at the outlet plane ($z = 4.6$ m). The upper figures correspond to an inlet velocity of $0.5\,\mathrm{m\,s^{-1}}$, while the lower figures correspond to $2.5\,\mathrm{m\,s^{-1}}$. It can be observed that, as the flow velocity increases, turbulence tends to flatten the ice distribution across the pipe cross-section, leading to a more homogeneous dispersion. In contrast, at low velocities under laminar flow conditions, buoyancy effects dominate, causing the ice particles to accumulate near the top of the horizontal pipe.

the literature regarding the formulation of the effective thermal conductivity, particularly in functions such as ϕ, which are expressed differently by various authors despite using the same theoretical basis.

Future work will focus on resolving the discrepancies in the thermal conductivity formulations from different authors to achieve a physically consistent model. This will involve systematically evaluating the different expressions for functions like ϕ to improve the near-wall heat transfer representation. The objective is to enhance the predictive accuracy of the model for both laminar and turbulent regimes and to better reproduce the observed ice distribution and heat-transfer behaviour in the pipe.

3.3.3 CFD-PBM model Example-03

Introduction

The objective of Du et al. (2023) analysis is to investigate the evolution and distribution of ice particles in supercooled water, as well as the flow characteristics of ice slurry during subcooling release in a horizontal straight pipe, using a CFD–PBM approach to capture particle growth, agglomeration, and breakage. The study examines the effects of inlet velocity, subcooling degree, and ice volume fraction on both the flow and particle behaviour.

It should be noted that Du et al. (2023) do not report experimental data, and model validation is conducted using previously published experimental results, analogous to the approach employed in our preliminary simulations of these three examples (Sec. 3.3.1, 3.3.2, and 3.3.3). Consequently, our comparison with these results does not constitute a validation against experimental measurements, but rather an assessment to a comparable modelling framework. Direct comparison is limited due to differences in specific sub-models and the absence of detailed information regarding the particle agglomeration, and breakage models used by Du et al. (2023).

Nonetheless, the study provides a wide range of CFD–PBM results beyond the velocity and pressure profiles shown in Sec. 3.3.1-3.3.2, including particle size distributions along the axial and vertical directions, with dependence on the supercooling degree, inlet velocity and ice volume fraction, offering valuable insights into particle behaviour and distribution. Comparing such a comprehensive set of data allows for an assessment of whether the model captures the essential aspects of the expected physical behaviour, even in the absence of direct experimental validation.

Modelling

The simulations were performed for a pipe with a diameter of 0.032 m and a length of 2.0 m. As in Examples 01 and 02, an structured *O-Grid* mesh, similar to that shown in Fig. 7, was used to enhance convergence and accuracy.

The model is developed similarly to the description in 3.3.1 and 3.3.2 with the main difference to the mass transfer process. The mass transfer process is governed by the PBE of Sec. 7.3 relying on the general expression of the PBE described in Sec. 7.3.2. For this modelling, the nucleation (Sec. 7.3.6) was not necessary to implement, as it was a boundary condition in the present simulations. A different growth rate as Langer and Müller-Krumbhaar (LM-K) model described in Sec. 7.3.3 was implemented via a UDF to adapt our model to the Du et al. (2023) model.

The corresponding particle growth rate used in Du et al. (2023) model is computed as

$$Gro_l = \frac{K_a}{3\,K_v}\left(\frac{h_{sl}}{\rho_s\,h_{fus}}\right)(T_m - T_l) \tag{13}$$

where Gro_l represents the particle linear growth rate, given in $\mathrm{m\,s^{-1}}$, h_{sl} denotes the interphase heat-transfer coefficient (computed from the Gunn correlation Gunn (1978)) expressed in $\mathrm{W\,m^{-2}\,K^{-1}}$ that it is also linked in the energy conservation law (Sec. 7.2.5). The geometric factors $K_a = \pi$ and $K_v = \pi/6$ correspond to the surface-area and volume-shape coefficients of the ice particles, respectively. The density of the solid phase, ρ_s, is defined in $\mathrm{kg\,m^{-3}}$, and h_{fus} is the latent heat of fusion of ice, $333\,550\,\mathrm{J\,kg^{-1}}$. The term T_m denotes the melting (equilibrium) temperature of the ice–water mixture in K, while T_l is the local liquid temperature surrounding the particles of the local cell, also in K. The sign and magnitude of the difference $(T_m - T_l)$ determine whether the dominant mechanism is particle melting or growth; however, for numerical stability, our code is limited to growth.

For the aggregation and breakage terms, alternative UDFs, based on different mathematical formulations than those described in Sec. 7.3.4 and in Sec. 7.3.5 were developed in order to reproduce the modelling approach of Du et al. (2023) as closely as possible. However, the kernel calibration parameters are not provided in that publication, despite these parameters having a dominant influence on the magnitude of the agglomeration and breakage source terms. Their absence leads to predictions in particle size that differ by up to an order of magnitude.

Consequently, although the corresponding UDFs were implemented, they could not be applied, and it was therefore not possible to reproduce particle-size predictions comparable to those reported by the author. A substantial part of the discrepancies observed between the two models can thus be attributed to the lack of calibration parameters for the breakage and agglomeration kernels, which directly affect the particle-size evolution and, ultimately, the comparability of the simulations.

Determining the most appropriate formulations for the agglomeration and breakage kernel functions, together with their calibration parameters, remains an open problem and will be addressed in the research planned for the coming months. This effort will require dedicated experimental data from this project.

Results and comparison

As shown in Fig. 16, the particle diameters predicted by the two models for the horizontal straight pipe (0.032m diameter and 2m length) exhibit substantial discrepancies, of approximately 20–40 %. Although considerable effort was made to reproduce the author's modelling approach by means of dedicated UDFs, important differences remain in the underlying formulations. As previously mentioned, and due to the absence of the required kernel calibration parameters, the model developed in this work does not incorporate aggregation or breakage UDFs, introducing a fundamental divergence from the reference model.

Despite these differences, the present model successfully reproduces the main physical trends observed in the original formulation. As shown in the upper plot of Fig. 16, increasing the degree of supercooling leads to larger particle sizes, consistent with both the author's results and the expected physical behaviour. The dependence of particle size on the inlet volume fraction, illustrated in the bottom-left plot of Fig. 16, also follows the same qualitative trend: higher inlet solid fractions yield larger particles. Similarly, the influence of inlet velocity, shown in the bottom-right plot of Fig. 16, is captured with a characteristic time response that depends on the flow velocity and remains consistent with the underlying physics: at higher flow velocities, the increase in mean particle size along the pipe is slower than at lower velocities.

The results from Du et al. (2023) shown in dashed lines in Fig. 17, which depict the distribution of the mean particle size along the vertical axis at the pipe outlet, capture the expected physical behaviour, with bigger particles tending to accumulate near the upper region of the pipe due to buoyancy effects. However, the preferential concentration of larger particles is less pronounced in our simulations, due to the absence of aggregation mechanisms in our model, which limits particle growth and results in generally smaller particles. Furthermore, under the turbulent flow conditions considered here, with velocities between $1\,\mathrm{m\,s^{-1}}$ and $2\,\mathrm{m\,s^{-1}}$, the particle distribution across the pipe cross-section is relatively uniform. This behaviour is physically reasonable and even more homogeneous than in the lower-velocity cases presented in the previous figures.

Fig. 18 shows the ice distribution, expressed as volume fraction, along the vertical axis at the pipe outlet. As previously noted, the absence of aggregation and breakage kernels in the model leads to a more uniform particle distribution, with fewer very large or very small particles. As a result, the distribution along the vertical axis is more homogeneous compared to the results reported in Du et al. (2023). Nonetheless, a clear tendency for the ice volume fraction to accumulate near the upper region of the pipe remains, reflecting buoyancy effects. This behaviour is qualitatively similar to the pronounced concentration peak observed in the original plots of Du et al. (2023), although it is less marked in our simulations. Overall, the key physical trends are correctly captured, despite notable differences in magnitude and particle size distribution.

Fig. 19 presents the mean fluid temperature along the pipe length, representing the evolution of the supercooling degree along the flow. The results indicate that our model predicts a faster rate of supercooling release compared to the trends reported by Du et al. (2023).

Fig. 20 presents two plots. The left plot shows the velocity profile at the pipe outlet as a function of the supercooling degree, which is very similar across all cases, with differences generally below 5–10 % at most points. The right plot depicts the fluid velocity along the pipe centerline for the $1\,\mathrm{m\,s^{-1}}$ inlet velocity case. A slight acceleration of the fluid along the pipe is observed, consistent with typical turbulent flow behaviour. This effect cannot be attributed to the small fraction of mass transitioning between solid and liquid phases, as the corresponding volume change is negligible. In our simulations, the final velocity is approximately 5 % lower than that reported in the reference study Du et al. (2023). These discrepancies might be influenced by particle size effects.

Fig. 21 illustrates the pressure drop along the pipe as a function of velocity. Minor differences of approx-

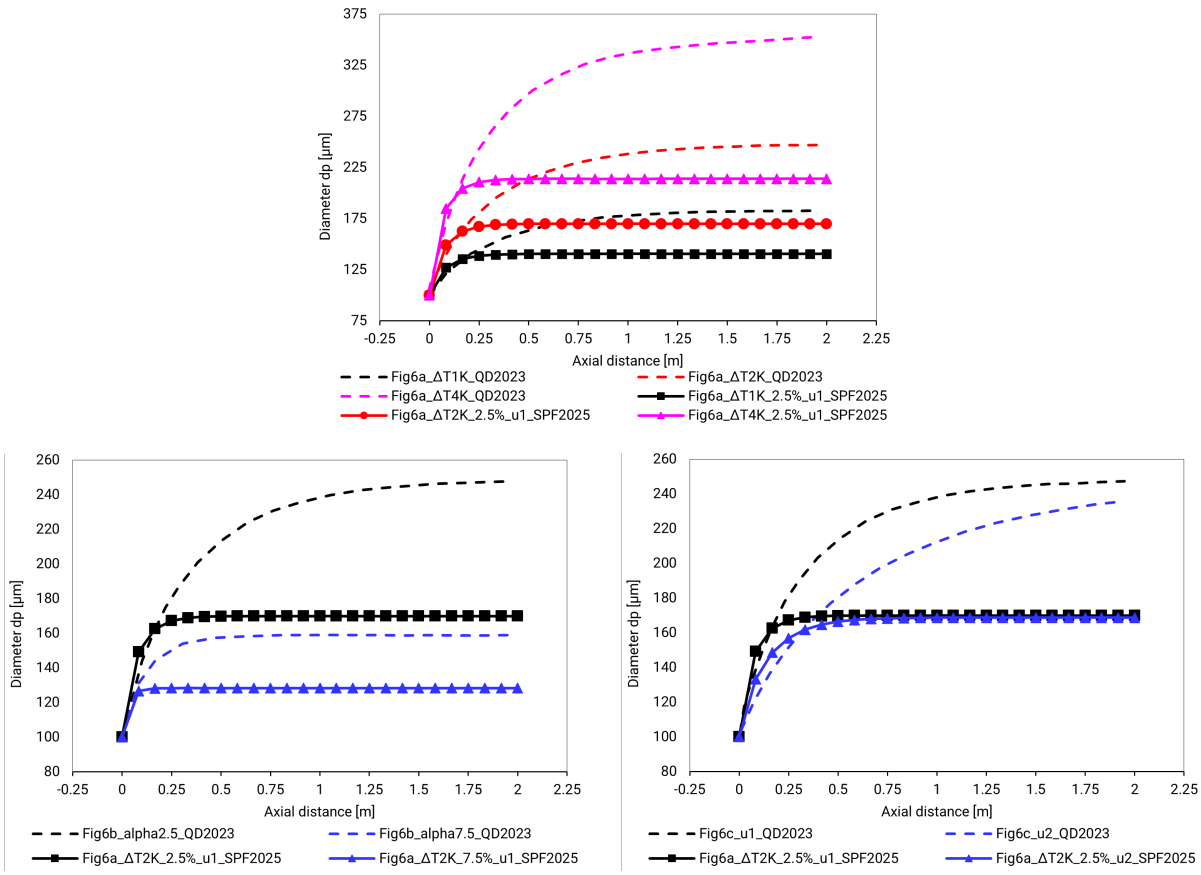

Figure 16: Comparative results of the mean particle diameter along the pipe length shown as functions of the following parameters: (top) supercooling degree (1, 2, and 4 K); (bottom right) inlet volume fraction (2.5 % and 7.0 %); and (bottom left) inlet velocity of $1\,\mathrm{m\,s^{-1}}$ to $2\,\mathrm{m\,s^{-1}}$. The dashed curves correspond to the results reported by Du et al. (2023), while the solid lines with markers represent the results obtained with our CFD–PBM model.

imately 4 % are observed at $1\,\mathrm{m\,s^{-1}}$, while larger deviations up to 29 % occur at higher velocities. These discrepancies may be related to particle size effects; however, this cannot be confirmed, as simulations with larger particles have not been conducted. In our model, as previously shown in the validation example with Niezgoda-Żelasko data 3.3.3, the simulated pressure drop aligns well with her experimental measurements rather than purely numerical simulations. Therefore, the validation of our model for pressure drop is expected to be more consistent and reliable compared to that of Du Du et al. (2023).

Conclusion

The comparative analysis between the present CFD–PBM model and the study by Du et al. (2023) highlights several key observations. Despite considerable effort to replicate closely the reference modelling approach using dedicated UDFs, significant differences remain due to the absence of aggregation and breakage kernels in our model. These differences result in particle diameters that diverge by 20–40 %.

Nevertheless, the present model successfully reproduces the primary physical trends observed in the reference study. Particle size increases with supercooling degree and inlet ice volume fraction, while the influence of inlet velocity is also qualitatively captured (Fig. 16). The distribution of particles along the vertical axis at the pipe outlet reflects expected buoyancy-driven behaviour, with larger particles tending to accumulate near the upper region of the pipe (Fig. 17), albeit less pronounced than in the reference results due to the absence of agglomeration mechanisms further than growth ones. Similarly, the ice volume fraction distribution is more

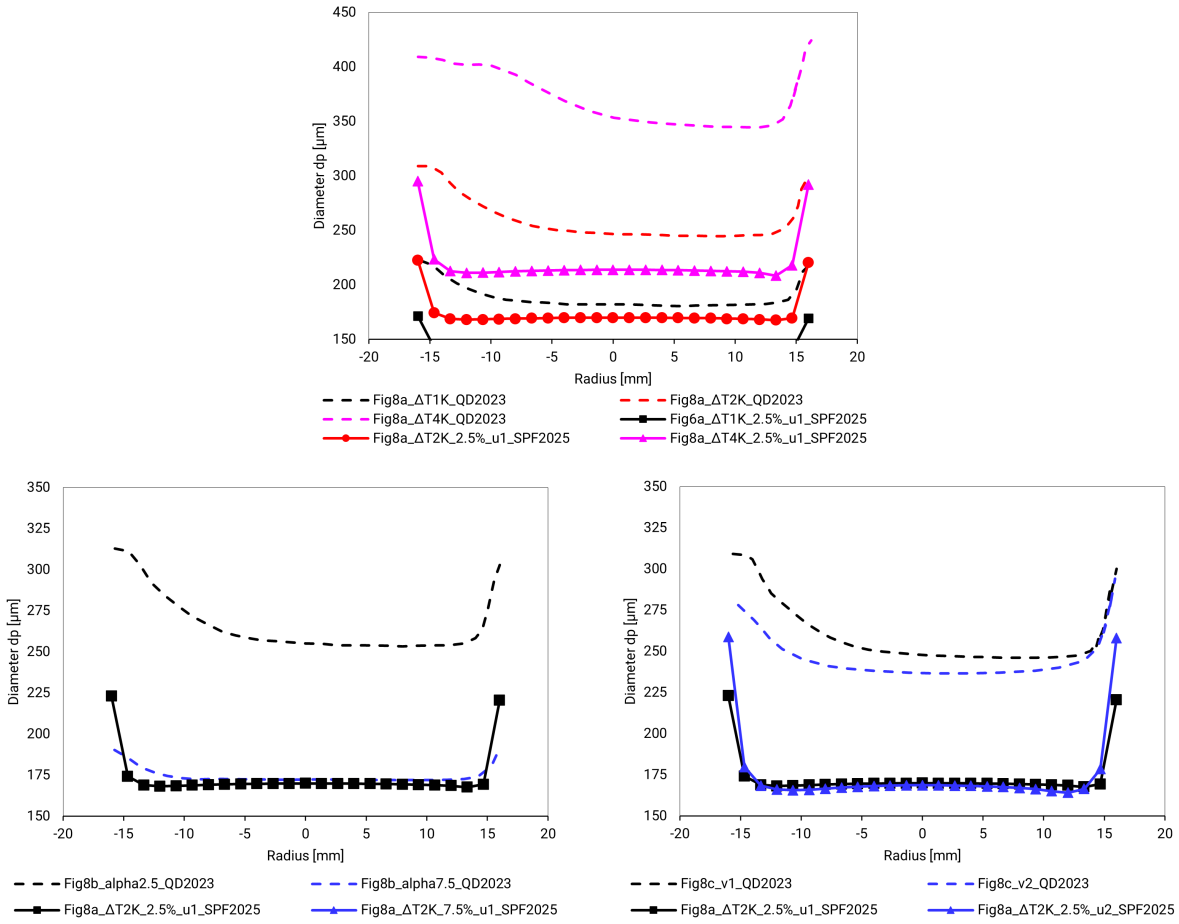

Figure 17: Comparative results of the distribution of the mean particle size along the pipe outlet vertical axis shown as functions of the following parameters: (top) supercooling degree (1, 2, and 4 K); (bottom right) inlet volume fraction (2.5 % and 7. %); and (bottom left) inlet velocity of $1\,\mathrm{m\,s^{-1}}$ to $2\,\mathrm{m\,s^{-1}}$. The dashed curves correspond to the results reported by Du et al. (2023), while the solid lines with markers represent the results obtained with our CFD–PBM model.

homogeneous, though the key qualitative trends remain consistent.

Regarding fluid dynamics, the model predicts a significantly faster release of supercooling along the pipe (Fig. 19), while velocity profiles at the outlet and along the centerline are in good agreement with the expected physical behaviour, showing minor deviations of 5–10 % (Fig. 20). The slight acceleration observed along the pipe (Fig. 20) is consistent with typical turbulent flow and cannot be attributed to the negligible volume fraction transitioning between solid and liquid phases.

Finally, pressure drop results from the present model (Fig. 21) show good agreement with experimental measurements reported by Niezgoda-Żelasko and Zalewski (2006), with minor differences at low velocities and larger deviations at higher velocities, potentially linked to particle size effects. Overall, the comparison demonstrates that, despite quantitative differences arising from missing aggregation and breakage terms, the model captures the essential physical behaviour of ice slurry flows, providing a solid basis for further development and refinement.

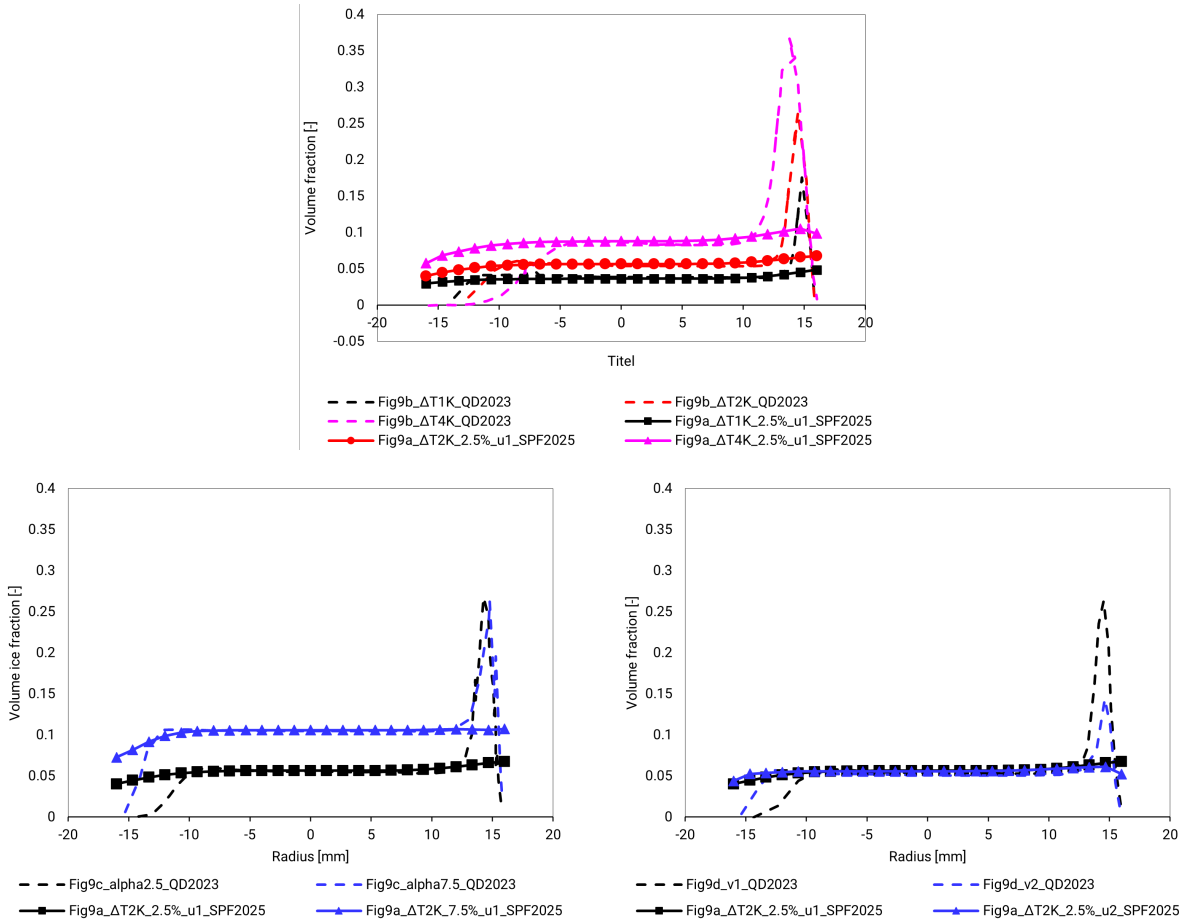

Figure 18: Comparative results of the distribution of the ice volume fraction along the pipe outlet vertical axis shown as functions of the following parameters: (top) supercooling degree (1, 2, and 4 K); (bottom right) inlet volume fraction (2.5 % and 7. %); and (bottom left) inlet velocity of $1\,\mathrm{m\,s^{-1}}$ to $2\,\mathrm{m\,s^{-1}}$. The dashed curves correspond to the results reported by Du et al. (2023), while the solid lines with markers represent the results obtained with our CFD–PBM model.

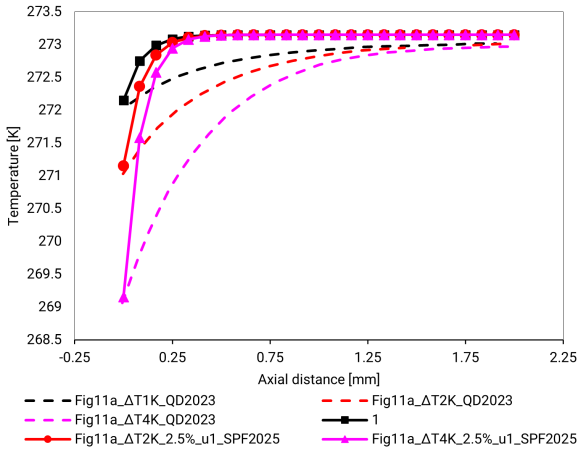

Figure 19: Comparative results of the mean fluid temperature along the pipe length as functions of the supercooling degree (1, 2, and 4 K). The dashed curves correspond to the results reported by Du et al. (2023), while the solid lines with markers represent the predictions obtained with our CFD–PBM model

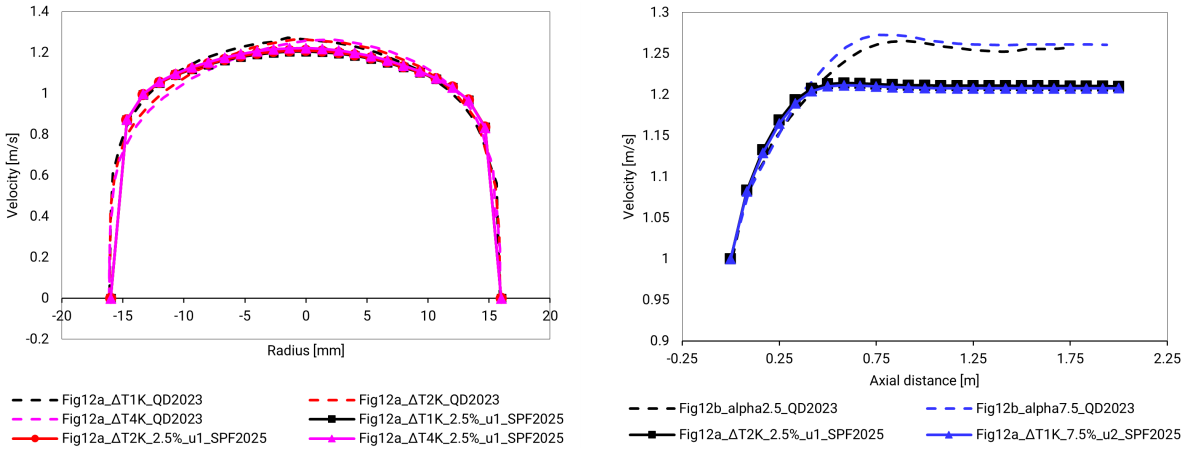

Figure 20: Left hand: comparative results of the velocity profile along the pipe outlet vertical axis shown as functions of the supercooling degree (1, 2, and 4 K). Right hand: comparative results of the velocity profile along the pipe centerline shown as functions of the inlet volume fraction (2.5 % and 7. %). The dashed curves correspond to the results reported by Du et al. (2023), while the solid lines with markers represent the results obtained with our CFD–PBM model.

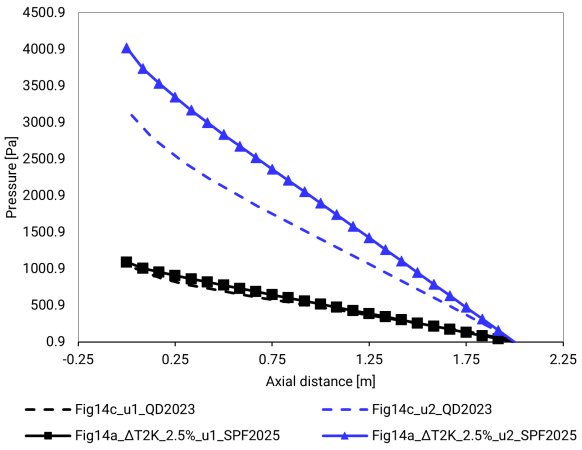

Figure 21: Comparative results of the pressure drop along the pipe versus inlet velocity of $1\,\mathrm{m\,s^{-1}}$ to $2\,\mathrm{m\,s^{-1}}$. The dashed curves correspond to the results reported by Du et al. (2023), while the solid lines with markers represent the results obtained with our CFD–PBM model

3.4 Experimental methods

3.4.1 Introduction

The experimental setup was designed and constructed with the objective of generating and characterising ice slurries under controlled conditions by means of non-intrusive Quantitative Flow Visualization (QFV) techniques.

The system setup allows the controlled formation, growth, and melting of ice particles within a closed hydraulic loop, where operating parameters such as flow rates and temperatures, specifically the supercooling degree, can be precisely regulated. The main active components of the experimental setup include a supercooler, a heat exchanger where water is supercooled in a control manner, a crystallizer equipped with ultrasonic activation for nucleation triggering, for exhausting the supercooling degree, and an ice slurry tank that storages ice slurry and separates ice crystals from water. This configuration enables stable, repeatable, and observable ice crystallization events suitable for optical measurements and quantitative image analysis.

Concerning the optical instrumentation, one of the main challenges in developing non-intrusive QFV techniques for measuring crystallization processes lies in the impossibility of applying conventional Particle Image Velocimetry (PIV) under laser illumination. The use of laser-based systems is unfeasible due to the strong light scattering produced by ice particles, which not only severely degrades image contrast and prevents accurate detection of particle size and motion but also introduces potential safety risks arising from the uncontrolled reflection of laser beams within the experimental domain. To overcome this limitation, an alternative illumination strategy is required—one that mitigates the effects of light scattering while still allowing clear visualization of particles within the flow. In this context, Backlight Shadow Imaging (BSI), which employs diffuse or collimated backlight illumination instead of laser light, offers a promising and non-intrusive approach.

Nevertheless, the visualization of ice crystals remains particularly challenging even with BSI, due to their transparency and the close refractive index similarity between ice and the surrounding medium ($n_{ice} = 1.309$, $n_{wat} = 1.333$ compared to $n_{air} = 1.000$). These optical characteristics reduce image contrast, challenging to delineate crystal boundaries and extract accurate quantitative parameters.

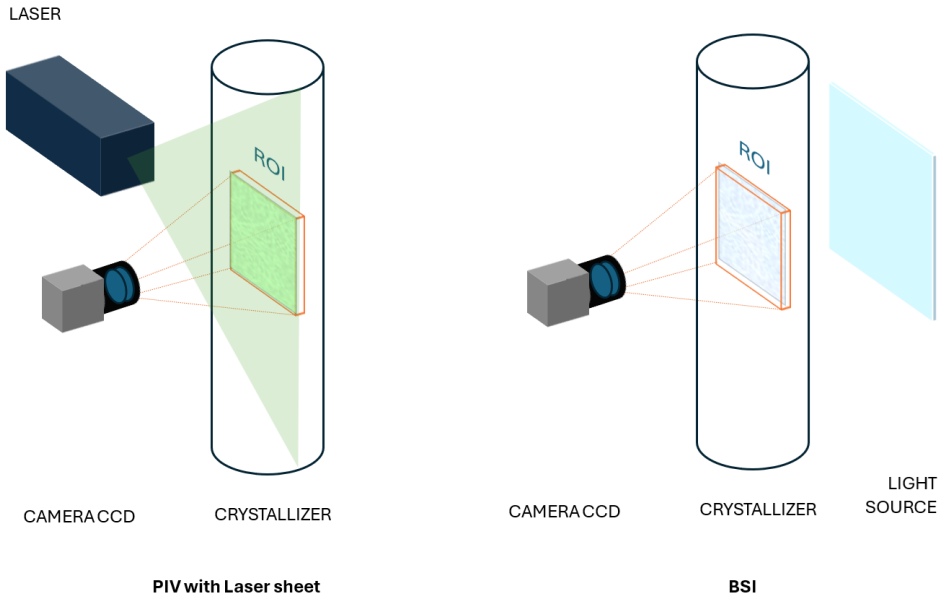

Figure 22: Comparison between optical visualization methods of a Region of Interest (ROI): on the left, a conventional Particle Image Velocimetry (PIV) setup employing a laser sheet; on the right, the Backlight Shadow Imaging (BSI) configuration using a backlight illumination source.

Backlight Shadow Imaging (BSI)

BSI is highly effective for visualizing and tracking particles, droplets and other structures such as ice crystals. It operates on the principle of pulsed backlight illumination combined with a (high-)magnification imaging system, enabling the precise capture of particle size, shape, orientation, and perimeter in the Region of Interest (ROI), within a well-defined focal plane and Depth of Field (DOF). The BSI method is applied to a wide variety of particles, solid, liquid, or gaseous, since it is largely independent of the particles' shape or material composition. However, the specific methodology must be adapted to the characteristics of the medium under investigation, with particular attention to the particles' optical contrast and scattering behaviour.

When operated in a double-pulse light source configuration and combined with a double-frame camera, the BSI setup enables not only the measurement of particle size and shape but also the determination of individual particle velocities and their spatial and temporal distributions within the ROI. By recording two successive images separated by a well-defined time interval (Δt), the displacement of each particle centroid between frames can be tracked, allowing for its velocity estimation. This approach provides time-resolved information on the fluidodynamic behaviour of dispersed phases, including velocities, trajectories, and local concentration gradients.

The quantitative data obtained from BSI can be statistically processed to derive size and velocity distribution functions and phase fraction estimations within the measurement volume. These outputs are particularly valuable for validating Computational Fluid Dynamics integrated with the Population Balance Models (developed in Sec. 7.2), referred as CFD-PBM, as they provide experimental evidence to compare with the model.

In addition, the simultaneous acquisition of morphological and dynamic parameters facilitates a direct correlation between particle shape, size, and motion, enabling a more comprehensive understanding of the coupling between dispersed and continuous phases within the crystallizer. Consequently, the BSI technique could serve as a powerful diagnostic tool that bridges the gap between high-fidelity optical measurements and predictive multiphase flow simulations.

3.4.2 Experimental setup for ice slurry crystallizer testing

Layout description

The experimental setup shown in Fig. 23 designed and constructed for the controlled production of ice slurry and for conducting complementary experiments, is based on a previous experimental ice slurry generation system employing the supercooling method, developed at SPF-OST under the supervision of Dr. Ann-Katrin Thamm and Kevin Erb.

As shown in Fig. 23 the experimental setup comprises three main circuits:

- the main circuit (in cyan), which employs tap water as the carrier fluid, which is successively supercooled, partially crystallized in the crystallizer to release the supercooling degree, then stored in the ice slurry tank, where ice particles are separated from the liquid phase.
- the glycol circuit (in orange), which employs a solution of tap water and glycol at 33% with a cold storage and serves as cooling thermal inertia for operating the setup.
- the hot tap water circuit (in blue) including a hot storage which serves as a heat sink for operating the heat pump, and heat source required for the preheater and in case of freezing events in the supercooler.

A water-water *heat pump* operates between the *hot storage* (blue in Fig. 23), filled with tap water, and the *cold storage* (green), filled with a 33 % glycol solution. The temperature in the cold storage (sensors TI 20 and TI 21) serves as the control variable for the heat pump, which activates to charge the glycol storage to the desired temperature. The cold water glycol solution from the cold storage is circulated through the *Supercooler HX*, controlled by TI 11 (to the desired T_{GlyIn}) by means of pump *Pe4* and the mixing valve V_{Gly}.

The water in the supercooled loop (cyan in Fig. 23) is circulated by pump *Pe1* from the storage *Slurry Tank* (in temperature close to 0 °C) through the *PreHeater*, a brazed-plate heat exchanger used to control the inlet temperature TI 1 (T_{WatIn}) of the supercooler. The hot side of the PreHeater is connected to the hot storage, and its temperature is regulated by pump *Pe3* and valve V_{Pre}. The mass flow rate in the supercooled loop is measured using a Coriolis mass flow meter (*Fl Wat*). The pumped water is supercooled in the supercooler to

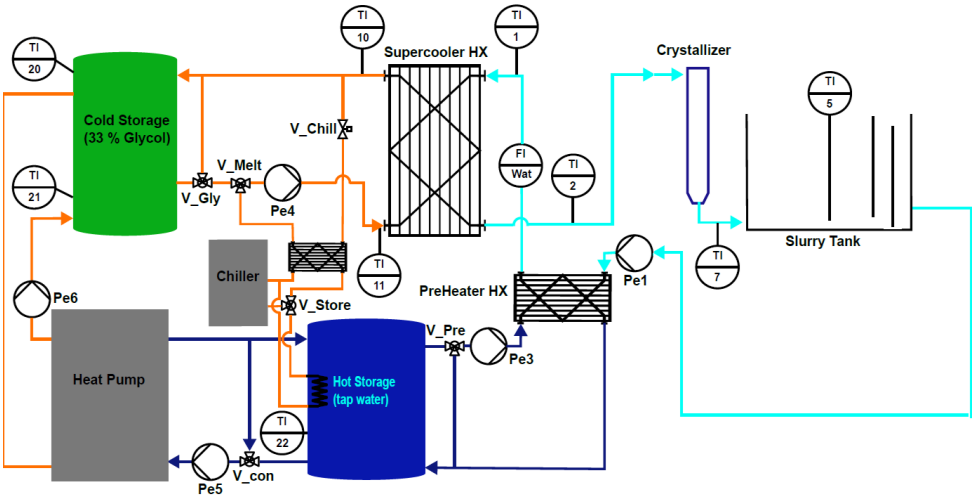

Figure 23: Schematic Piping & Instrumentation Diagram of the current set up. The color code represents the working fluids: orange indicates the glycol circuit, cyan corresponds to the supercooled loop (filled with tap water in our experiments), and dark blue denotes the tap water circuit for heating purposes. Main equipment composed by the Heat Pump and the Cold and Hot Storage, the Chiller, the Supercooler and PreHeater HX, the Crystallizer and the Slurry Tank.

the desired supercooling degree ΔT_{sc}, controlled by the temperature sensor TI 2 (T_{WatOut}) and directed into the crystallizer.

In the *crystallizer*, nucleation is triggered in the supercooled water by ultrasonic transducers attached to the external wall of the crystallizer. Once ice nuclei are present, the ultrasonic transducers are turned off, and nucleation continues autonomously. The supercooling potential is released through controlled crystal growth. The resulting ice slurry leaves the crystallizer at approximately 0 °C, consisting of ice particles suspended in liquid water, with a solid mass fraction of about 2.5 % (when the $\Delta T_{sc} = 2$ K). The produced slurry is then directed into the ice *slurry tank*, thereby closing the circuit and allowing recirculation of the liquid phase to continuous produce ice slurry.

When melting of ice within the supercooler is required, hot glycol, supplied from the chiller and connected via valves V_{melt} and V_{Chill}, and pumped by *Pe4*, can be employed.

Control description

The experimental system is controlled and monitored using a National Instruments (NI) CompactDAQ platform, which interfaces between a computer running a custom LabVIEW GUI and the connected I/O hardware modules. The I/O hardware consists of digital and analog modules from WAGO, each with two to four channels, responsible for controlling valves, pumps, the heat pump, and the chiller.

The control software continuously monitors the system for freezing events, which are detected as sudden deviations in mass flow indicating potential hydraulic blockage. Upon detection, the control automatically stops the test: pumps Pe1, Pe3, and Pe4, as well as the chiller, are turned off, and all valves are closed to prevent equipment damage and allow automated de-icing.

Temperature measurements are obtained from PT100 sensors immersed in the flow and acquired by 8-channel NI temperature input modules, with a precision of ± 0.03 K.

The mass flow rate in the supercooled loop is measured using a Coriolis flow meter with a precision of ± 0.15 %.

The supercooling power, defined as the thermal energy stored in the supercooled water as sensible heat and subsequently released as latent heat upon nucleation, is calculated from the measured supercooling degree ΔT_{sc} in K, the mass flow rate of the supercooled water $\dot{m}$ in kg h^{-1}, and the specific heat capacity of water c_P in J kg^{-1} K^{-1}), according to:

$$P = \frac{Q}{t} = \dot{m} \cdot c_P \cdot \Delta T_{sc} \tag{14}$$

Crystallizer description

Two crystallizers are described in the following paragraphs. *Crystallizer-01* corresponds to the unit currently installed in the experimental setup, which has been used for the initial measurements with the BSI technology. *Crystallizer-02* is the one planned for the future experimental campaign. Although it is not yet certain whether it can operate reliably and safely to perform the crystallisation process, it offers advantages for BSI technique and image acquisition, as well as for subsequent particle characterisation and model validation. In this configuration, the particles flow approximately parallel to the region of interest (ROI), and the particle age can be tracked in detail, making it particularly useful for experimental analysis.

Crystallizer-01

The crystallizer-01 is composed by an approximately one meter length and 100 mm diameter transparent PVC cylinder ($n_{pvc} = 1.53..1.55$) to which there is a tangential inlet. Fig. 24

Supercooled water, free of ice, is introduced at the top of a vertically mounted in-stream crystallizer (Fig. 24) through the inlet. The tangential entry accelerates the fluid and creates a swirl, which promotes uniform mixing of ice crystals and supercooled water within the crystallizer (see Fig. 26 (a) and (b) showing fluid flow trajectories and, (d) and (f) depicting the turbulent kinetic energy in a rage between 0.01 $m^2\,s^{-2}$ to 1 $m^2\,s^{-2}$).

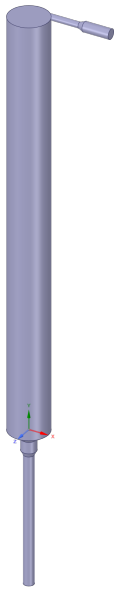

Figure 24: General view of Crystallizer-01. Water is fed at the top of the vertically aligned in-stream crystallizer through a tangential inlet and discharged through the bottom outlet.

As shown in Fig. 26 (d), the velocities in the region of interest (ROI) range from approximately 3 $m\,s^{-1}$ at the outer edges to less than 1 $m\,s^{-1}$ in the central region. The higher velocities near the walls are mainly tangential to the ROI plane due to the swirl induced by the tangential inlet, with a slight downward component toward the bottom outlet. In contrast, the central region exhibits a much lower and oscillating upward flow, with magnitudes below 1 $m\,s^{-1}$, as indicated by the blue coloring in the figure. These observations correspond to the nominal operating conditions of the crystallizer, which correspond to a mass flow rate of 1.19 $kg\,s^{-1}$.

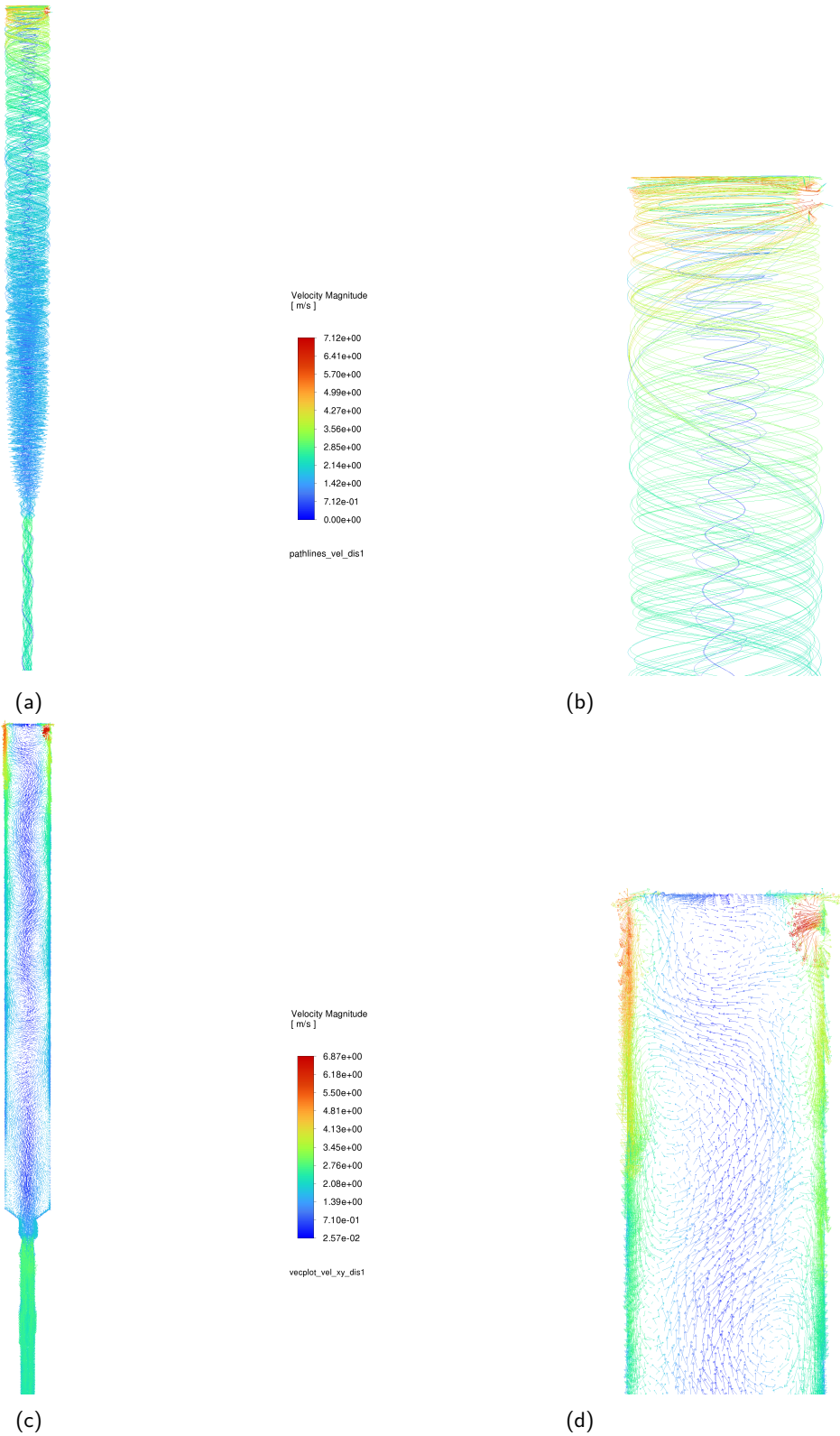

Figure 25: Results from CFD simulation: (a, b) pathlines illustrating the 3D fluid flow trajectories; (c, d) fluid velocity vectors projected onto the ROI plane.

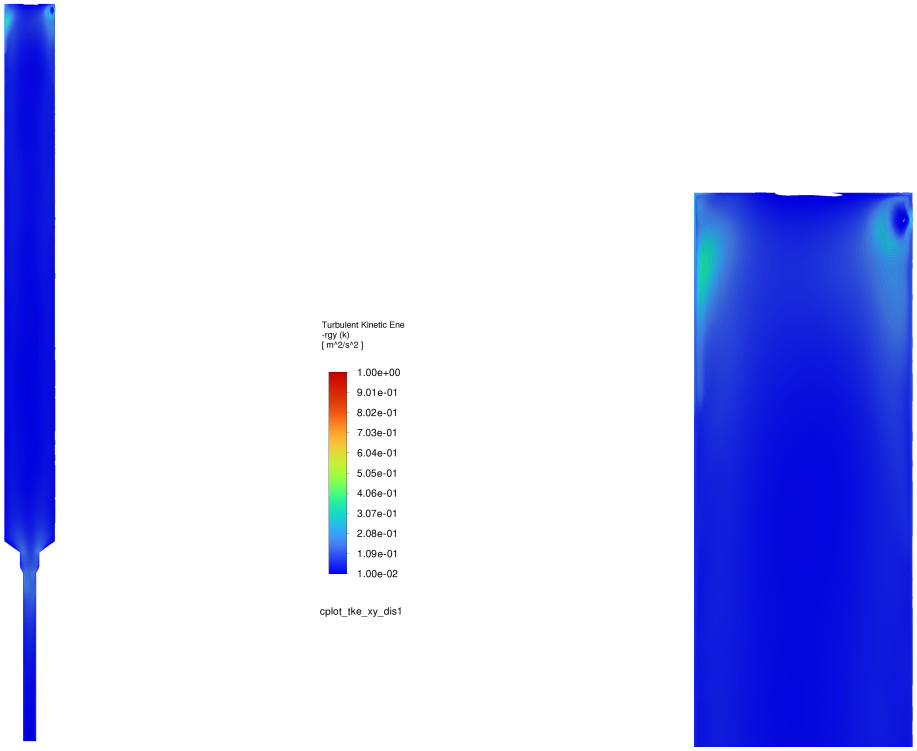

(e) (f)

Figure 26: Results from CFD simulation: (e, f) turbulent kinetic energy distributions on ROI plane.

It is also expected that particle velocities will be of the same order of magnitude as those of the fluid. Due to the design characteristics of crystallizer-01, particle sizes in the ROI are highly variable. The population within this region is expected to be well mixed, containing particles of different "ages": some particles may have only a few milliseconds, while others may have a residence time of several seconds. Consequently, the particle population in the ROI is likely to exhibit a wide range of sizes. Experimental evidence indicates the formation of ice particle conglomerates of several millimeters in size, even exceeding 10 mm to 20 mm mean diameter. Individual crystals are expected then to reach sizes of up 10 mm, starting from the minimum nucleation size of 2.3×10^{-5} mm.

Crystallizer-02

Crystallizer-02, designed to have a volume comparable to that of Crystallizer-01, is composed of an approximately five-meter-long cylinder, bent into four straight sections, with a diameter of 47 mm, made of transparent PVC. A coaxial inlet is attached to the cylinder, as shown in Fig. 27.

Likewise, in Crystallizer-01, supercooled water, free of ice, is introduced at the top of the vertically mounted in-stream crystallizer (Fig. 27). In the absence of the tangential inlet, the fluid flows along the pipe, predominantly parallel to the plane of symmetry (which coincides with the ROI), as shown in Fig. 29 (a) and (b), depicting the fluid flow trajectories. Consequently, the turbulent kinetic energy, shown in Fig. 29 (d) and (f), remains below $0.01\,\mathrm{m^2\,s^{-2}}$ along most trajectories, which reduces the mixing effect expected in the previous crystallizer, but allows a new perspective for model validation.

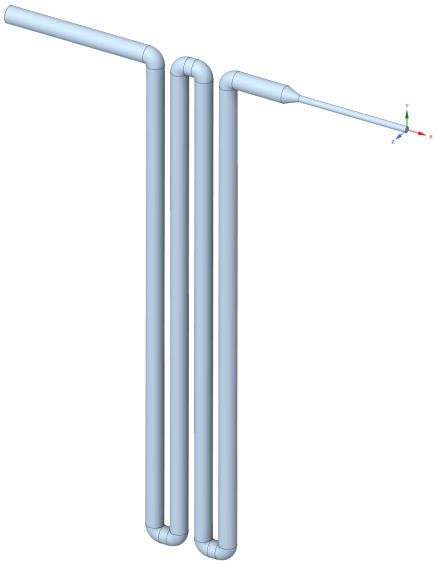

Figure 27: General view of Crystallizer-02. Water is fed at the top of the vertically aligned in-stream crystallizer through a coaxial inlet and discharged through the bottom outlet.

As shown in Fig. 29 (d), the velocities in the region of interest (ROI) range from approximately $0.5\,\mathrm{m\,s^{-1}}$ to $1\,\mathrm{m\,s^{-1}}$ as indicated by the blue colouring in the figure. The vector velocities are mainly parallel to the ROI plane due to the absence of swirl induced by the tangential inlet. These observations correspond to the nominal operating conditions of the crystallizer, which correspond to a mass flow rate of $1.19\,\mathrm{kg\,s^{-1}}$.

In contrast to Crystallizer-01, the particles in this configuration appear gradually and consecutively within the ROI across each of the four vertical straight sections. This provides more detailed information on the characteristic size of the ice particles in each section, since the particles exhibit different residence times within the crystallizer. Unlike in Crystallizer-01, where particles within the ROI were highly mixed, in this case their "age" distribution is more clearly differentiated.

This crystallizer-02 is intended to improve the analysis of three main aspects:

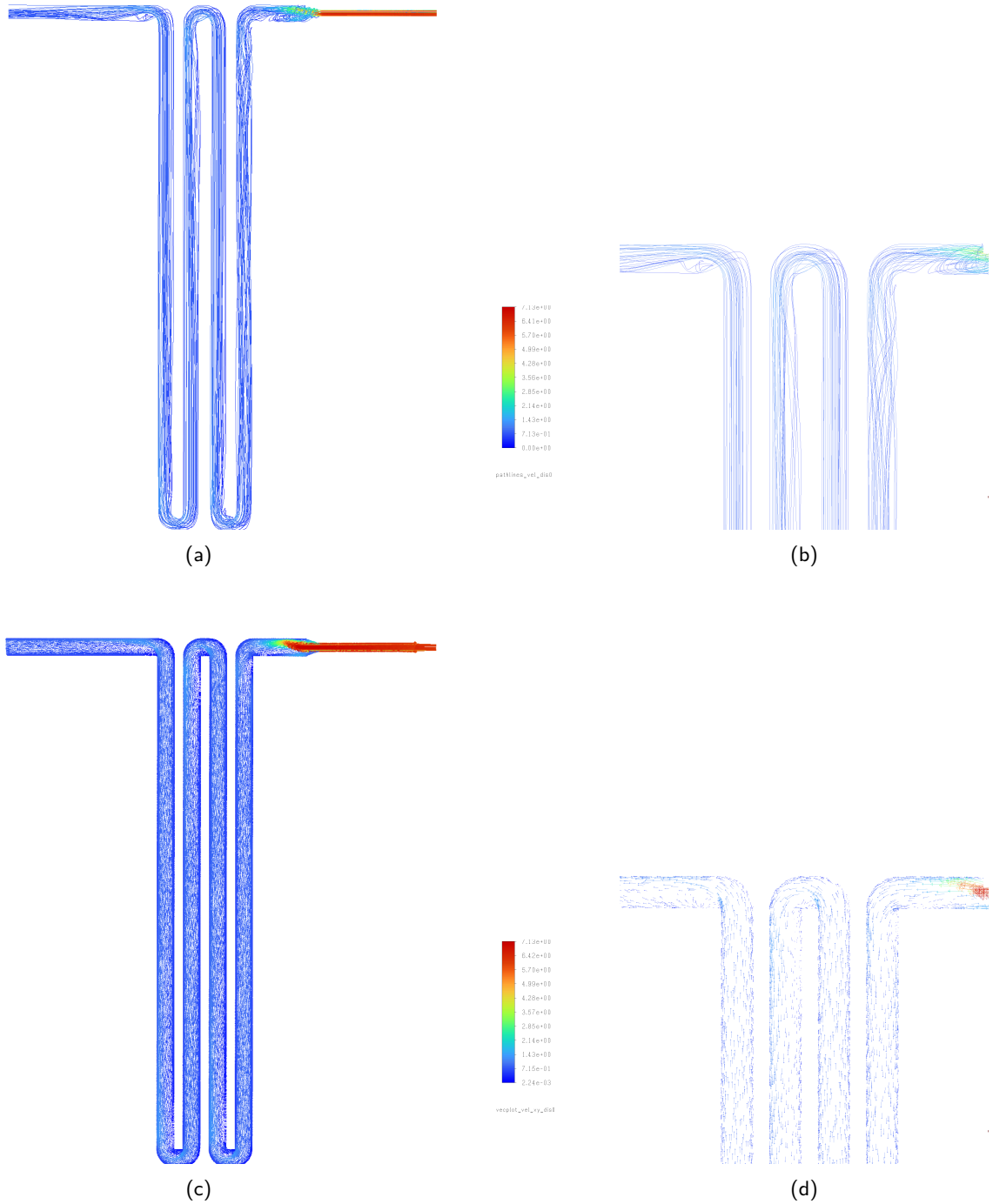

(a) (b)

(c) (d)

Figure 28: Results from CFD simulation: (a, b) pathlines illustrating the 3D fluid flow trajectories; (c, d) fluid velocity vectors projected onto the ROI plane.

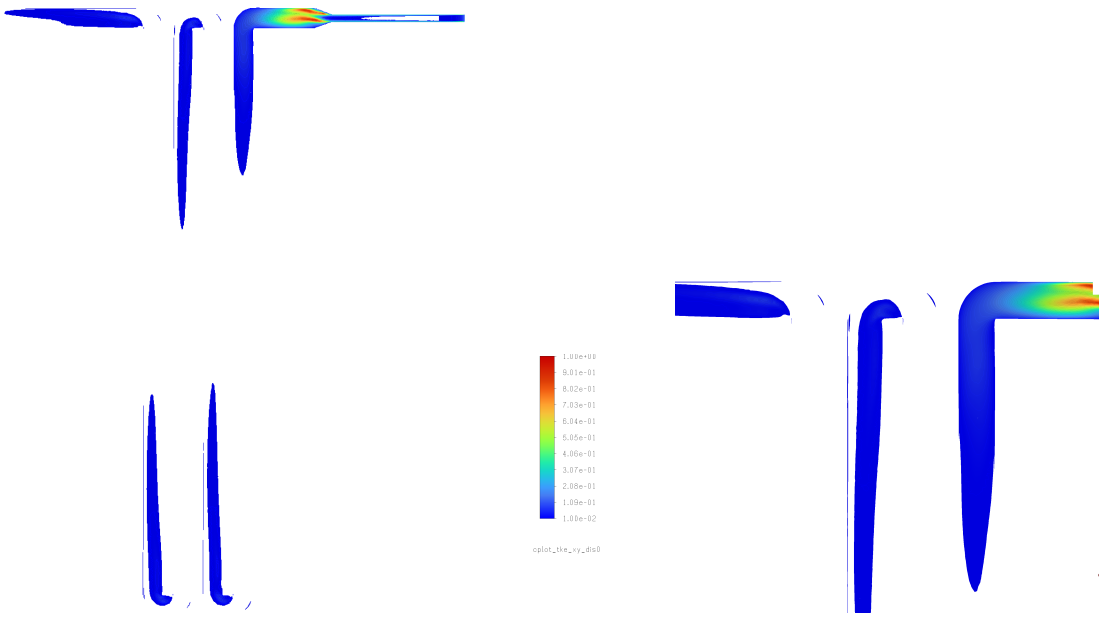

(e) (f)

Figure 29: Results from CFD simulation: (e, f) turbulent kinetic energy distributions on ROI plane.

- **Particle stability within the observation region:** ensuring that the particles remain within the depth of focus of the measurement area.
- **Detailed growth analysis:** enabling a more precise evaluation of particle growth, as particles can be distinguished according to their residence time inside the crystallizer.
- **Optical clarity:** by reducing the crystallizer diameter, the amount of scattered light, and therefore image blurriness, is expected to decrease. A smaller diameter reduces the number of ice particles located in front of and behind the depth of focus, allowing the light to reach the observation plane more directly and with less deviation.

.

3.4.3 Optical system selection for imaging a defined region of interest

The successful implementation of the in-stream crystallization experiment visualization by means of the Backlight Shadow Imaging (BSI) relies on careful harmonization of multiple interconnected parameters from fluid-flow and from optical and imaging visualization system, each of which influence the achievable spatial resolution, measurement uncertainty, and overall reliability of the results. A systematic approach is essential, starting from the characteristics of the supercooled flow and ice particles' size and trajectories, and proceeding through optical and imaging system design, to the final evaluation of the recorded images.

Flow and ice particle characteristics

The first step in the design of the experiment is to define the flow conditions and particle properties. Key factors include:

- **Particle material**. Individual ice crystals are almost transparent owing to their structural uniformity and purity, allowing light to traverse them with very limited scattering. When multiple crystals combine

to form larger conglomerates, however, light scattering increases substantially due to the presence of internal interfaces (trapped air inclusions, and misaligned crystal orientations). Consequently, these conglomerates appear translucent rather than transparent, transmitting light but diffusing it in multiple directions. Using BSI imaging, visualizing ice crystals remains particularly difficult because of their optical transparency and the close similarity between the refractive indices (n_i) of ice n_{ice} and liquid water n_{wat}. This small difference, approximately 1.309 for ice and 1.333 for water, produces very weak optical contrast, reducing image sharpness and making it challenging to distinguish crystal boundaries or obtain reliable quantitative measurements.

- **Particle size**. While the particles within the ROI can span from the nucleation size of approximately 2.3×10^{-5} mm up to the order of 10–20 mm, forming conglomerates of particles, the experimental focus will be more on particle growth and its motion. Monitoring particles from nucleation to supercooling degree exhaust, across those five orders of magnitude in size, is impractical, as it would require extremely high magnification and thus sacrifice the FOV to very few mm. Therefore, the analysis will concentrate on particles larger than 0.2 mm, resulting in a size range roughly from 0.2–0.5 mm up to 15 mm. Restricting the observation to two orders of magnitude, rather than five is a compromise between a wide enough FOV and is sufficient for characterizing the ice crystal growth and motion model under turbulent flow conditions, which is the main objective of the experiment in order to validate de CFD-PBM model.

  Previous studies Adrian (1997), Kähler et al. (2012), Scharnowski and Kähler (2020) have shown that the apparent diameter of particle images on the sensor critically affects the accuracy of displacement estimation and, consequently, the derived velocity fields. Particle images that are significantly larger than approximately three pixels lead to broadened correlation peaks and increased random uncertainty, whereas images smaller than two pixels suffer from under-sampling, which impairs centroid detection and degrades the signal-to-noise ratio due to electronic and photon noise.

  An optimal compromise is therefore achieved when particle images span roughly 2–3 pixels in diameter (measured at the $1/e^2$ intensity level), balancing localization accuracy and image contrast while minimizing the influence of background noise. In this study, this criterion guided the selection of optical magnification, camera pixel pitch, and illumination intensity to ensure that particles within the target size range (0.2 mm to 15 mm) are captured with sufficient resolution across the entire field of view, thereby reducing measurement uncertainty and supporting reliable PIV/BSI post-processing.

  Unlike conventional PIV experiments with nearly uniform seeding particles, the present work focuses on ice crystal growth, which spans several orders of magnitude—from micrometer-scale nuclei to millimeter-scale crystals and aggregates. Accordingly, the particle image size varies considerably during an experiment. While the smallest crystals may occupy only 2–3 pixels initially, larger particles and aggregates can cover tens of pixels.

  In this context, the previous guidance on optimal particle image size remains applicable as a lower bound, ensuring that even the smallest particles are resolved with adequate accuracy for displacement measurements. Simultaneously, the imaging system must accommodate the full range of particle sizes without detector saturation or loss of field-of-view coverage. This necessitates careful choices of magnification, illumination, and camera dynamic range to capture the complete spectrum of particle growth, enabling quantitative measurements of particle size, shape, and motion throughout the experiment.

- **Particle velocity and displacement:** The expected particle velocities define the required minimum *dynamic velocity range* (DVR), the maximum velocity range that can be measured with a fixed optical and imaging system, and thus dictate the temporal separation (Δt_{bf12}) between successive camera exposure times and the timing of the light sources to ensure that particle images are properly captured . In determining (Δt_{bf12}), both main directions of particle motion within the region of interest (ROI) must be considered: the *in-plane* motion, which should produce measurable displacements without exceeding the interrogation window, and the *out-of-plane* motion, perpendicular to the ROI, which should be limited to minimize the number of particles leaving the depth of field (DOF) and consequently reducing *valid detection probability* (VDP), thus reducing the fraction of vector fields that could be considered valid.

Therefore,the choice of temporal separation between pulses must balance these two considerations, ensuring sufficient particle displacement for reliable correlation while keeping particles within the imaged volume defined by the DOF.

- **Flow orientation relative to the measurement plane:** Although particles travelling parallel to the ROI plane are ideal for 2D PIV or BSI measurements, transverse motion can cause out-of-plane decorrelation. When motion perpendicular to the ROI plane cannot be avoided, it should be taken into account to maintain a high Valid Detection Probability (VDP), thus maintaining the maximum fraction of vector fields that will be considered valid within the ROI.

Magnification

In order to design an imaging system for a Region of Interest (ROI) measuring approximately 100 mm in width which is the diameter of the crystallizer experimental setup, as depicted in Fig. 30, and using a camera sensor with a Sensor Size (SS) of 15.6 mm, the required optical magnification (M) can be calculated using the ratio between the sensor size and the vertical or horizontal of the Field of View (FOV), which corresponds to a demagnification of approximately 1:6.4, indicating that the ROI must be reduced by a factor of 6.4 to fit the sensor.

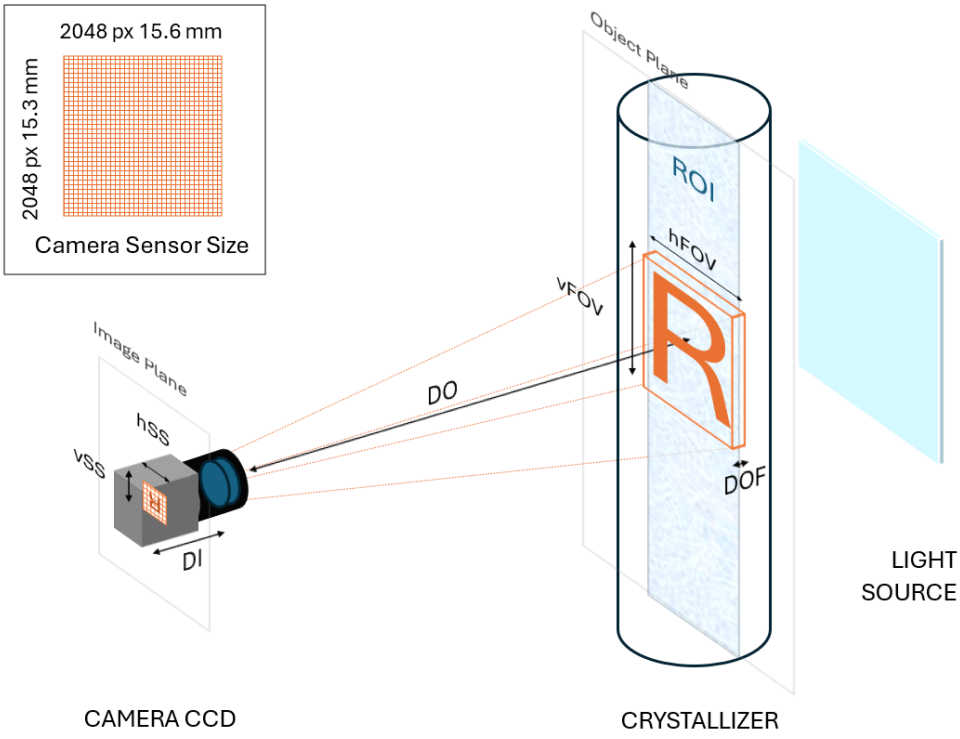

Figure 30: A schematic representation of the optical system illustrating the object and image planes. The region of interest (ROI), characterised by a defined field of view (vFOV × hFOV), is located in the object plane, which only a specific depth of field (DOF) can be sharply imaged. The resulting image is formed in the image plane and should be captured within the sensor's active area (vSS × hSS). Although the object distance (DO) and image distance (DI) shown in the diagram represent distances within the optical system relative to the lens elements, the mathematical expressions presented later treat the system as a simplified single thin-lens model, even though the optical system typically consists of multiple lens elements.

Resolution

In imaging systems, *resolution* describes the ability to reproduce fine details of the object plane. It is influenced by several factors, including illumination, contrast, sensor pixel size, and the optical performance of the system.

The sensor of the CCD Imager ProX4M LaVision camera employed in the experimental setup is the starting point for calculating system resolution, as it defines the baseline requirements for lens performance and ensures compatibility with application needs. The CCD camera ProX4M from LaVision integrates a sensor with (2048 x 2048) pixel resolution and physical dimensions of 15.6 mm x 15.3 mm, yielding a pixel size (pixs) of 7.4 µm x 7.4 µm LaVision (2023).

The highest spatial frequency that a sensor can theoretically resolve corresponds to two pixels forming one line pair.

Hence, the smallest resolvable feature in the object plane is approximately 95 µm, or about ca. 0.1 mm when rounded, which aligns well with the scale of the experiment under evaluation.

Lens - Focal Length

Fixed focal length lenses are defined by a specific *focal length* (f) and a constant angular field of view (AFOV). When the distance to the object changes, the size of the field of view varies accordingly. However, the angular field of view itself remains constant. Fixed focal length lenses are defined by a specific focal length (f) and a constant angular field of view (AFOV). When the distance to the object changes, the size of the field of view varies accordingly. However, the angular field of view itself remains constant.

As shown in Fig. 30 and Fig. 31, the image is formed on the image plane, located at a distance DI from the lens, where light rays originating from the object plane at DO converge to form a sharp image. In real optical systems, however, points lying within a limited range around these ideal planes are captured within an acceptable sharpness. These regions around the ideal planes are known as the Depth of Field (DOF) for the object plane and depth of focus for the image plane, which depend on different factors.

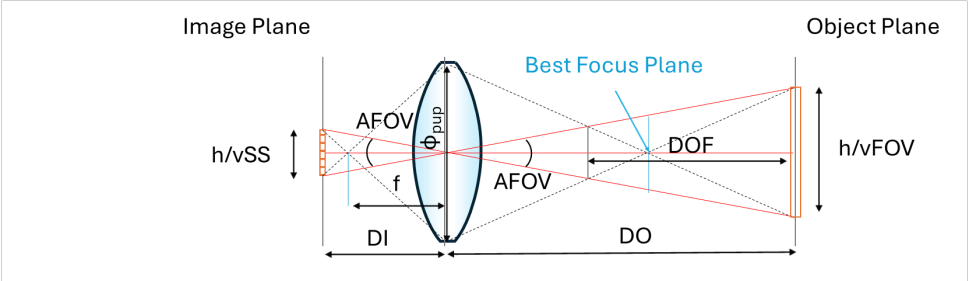

Figure 31: Simplified scheme of the relation between horizontal or vertical Field of View (h/vFOV) in the object's plane, horizontal or vertical sensor size (h/vSS) in the image plane captured by the sensor of the camera, the Focal length (f) of the selected lens and the resulting distance to object (DO) and distance to image (DI). Additionally, the angular field of view (AFOV), depth of field (DOF) and lens diameter aperture (ϕ_{pup}) are represented.

,

4 National/International cooperation

In the current stage of the project *ModIceCrys*, the national/international cooperation level has been initiated:

- A collaboration with Assis. Prof. Dr. Thomas Schutzius, through an SNF project *FRIO: Fundamentals of Recalescent Freezing on Immersed Nano-engineered Surfaces: The Influence of External Flow and Ultrasonic Fields* was in place last year. This proposal was submitted and approved when Dr. Thomas Schutzius was in Institut für Energietechnik - ETH Zürich. Currently, Prof. Dr. Thomas Schutzius is at Berkeley University in California (United States) from where he leads as Principal Investigator (PI)

the FRIO project. Dr. Daniel Carbonell is the Co-Investigator (CoI) ensuring thus a proper know-how transfer.

- SPF is a partner in an inter-continental project funded by the Department of Energy (DOE) from United States where the ice slurry using the supercooling method is applied to thermo-electrical energy storage solutions using a Carnot battery concept. The ice crytallizer develop for that project will be used in ModIceCrys as first design for testing the CFD models.

5 Publications and conference contributions

In parallel, a scientific article entitled *"Comparative Analysis of Three Ice Slurry Production Methods for Thermal Energy Storage Enabling Dispatchability in Industrial Cooling Demands"* was submitted to the Journal of Energy Storage in September and is currently under peer review. A second manuscript, planned for the second half of 2026, will address the modelling of ice slurry flow phenomena. A third publication, focused on the experimental validation of the developed model, may also be initiated before the end of 2026.

6 Evaluation of 2025 and outlook of 2026

The project *ModIceCrys* started in November 2022. During 2023, a comprehensive literature review of supercooling method and crystallization was conducted. This comprehensive review gave valuable insights into nucleation and crystal growth models that have been employed in both the Population Balance Models (PBM) and the coupled multi-scale Computational Fluid Dynamics (CFD) for the crystallizer model.

During 2024, based on the previous bibliographic research, the first multi-scale coupled CFD-PBM model has been developed and tested with good agreement for an ice slurry flow in a horizontal pipe in different flow-rates boundary conditions. The development of this model embraced an extensive mathematical overview of the model and are comprehensively documented in the report from the previous year.

Following the literature review performed during 2023 and the initial model development in 2024, the CFD–PBM framework was further consolidated in 2025. Additional independent validations were conducted using experimental datasets from the literature, and the model was refined and adapted to the specific geometry and operating conditions of the project's crystallizer. The model has been prepared for validation using experimental data from the 2025–2026 campaign.

The CFD–PBM model developed within *ModIceCrys* was initially validated by comparing its simulation results against both experimental data Niezgoda-Żelasko (2006), Niezgoda-Żelasko and Zalewski (2006), Sari et al. (2000), Vuarnoz et al. (2002) and the CFD–PBM results reported by Du Du et al. (2023). The comparisons focused on key observables, including pressure drop, velocity profiles, fluid temperature, ice volume fraction, and particle size distribution along the pipe.

Overall, the model reproduces the expected fluid behaviour and main physical trends inherent to ice slurry flows. Vertical and horizontal velocity profiles show good agreement with experimental observations, capturing the characteristic flow patterns. The model also correctly predicts the preferential accumulation of particles near the upper region of the pipe due to buoyancy, the effect of supercooling on particle growth, and the qualitative influence of inlet velocity and ice volume fraction on particle size. Pressure drop simulations align well with the Niezgoda–Żelasko experimental data, while velocity profiles remain consistent with both experimental and numerical references.

Nevertheless, some discrepancies were identified. Simulated particle sizes differ from Du's CFD–PBM results by approximately 20–40 %, primarily because the current model does not include aggregation or breakage phenomena due to the lack of calibration parameters for the breakage and agglomeration kernels in Du et al. (2023). Deviations in local heat-transfer coefficients under turbulent flow conditions further highlight the need for a physically consistent formulation of effective thermal conductivity.

Despite these limitations, the preliminary simulations provide the first step for a representative and physically coherent description of ice slurry flows. Future work will focus on incorporating aggregation and breakage mechanisms and obtaining detailed experimental data for model calibration and full validation, aiming to refine simulation results and minimize remaining discrepancies.

On the experimental axis, the laboratory setup was upgraded and prepared for the experimental campaign, including improvements on the ice slurry pumping and hydraulics as well as on control and data acquisition. Particular attention was given to optical access and visualization challenges, especially condensation on cold surfaces from the crystallizer. Several mitigation strategies were implemented and tested, with air-blowing systems proving to be the most effective.

A first series of tests using the Backlight Shadow Imaging (BSI) technique were conducted during the second half of 2025. Although the results have not yet provided sufficient data for full model validation, they have yielded important guidance for improving the experimental design, including the need for alternative crystallizer configurations and enhanced optical accessibility.

Looking ahead to 2026, the project will continue to focus on modelling, experimental, and dissemination activities.

In terms of modelling, further developments of the CFD–PBM model will be undertaken only if required by the experimental observations. In particular, the incorporation of additional physical mechanisms, such as ice adhesion effects, will be considered only in the event that upstream ice growth or related phenomena are observed, which, to date, have been successfully mitigated under the current experimental conditions.

In the experimental dimension, testing with the crystallizer is planned to continue during the first half of 2026, potentially involving the evaluation of an alternative crystallizer design. The data generated from both experimental campaigns will be essential for validating the CFD–PBM models and for strengthening the synergy between the theoretical and experimental components of the project.

In terms of dissemination, one or two scientific publications are anticipated. One article will focus on the modelling of ice slurry flow phenomena, while a second publication, addressing the experimental validation of the developed model, is expected by the end of 2026 or the beginning of 2027.

References

International dictionary of refrigeration.

Abrahamson, J. Collision rates of small particles in a vigorously turbulent fluid. 30(11):1371–1379.

Adrian, R. J. (1997). Dynamic ranges of velocity and spatial resolution of particle image velocimetry. 8(12):1393.

Akhtar, S., Xu, M., and Sasmito, A. P. A novel crystal growth model with nonlinear interface kinetics and curvature effects: Sensitivity analysis and optimization. 21(6):3251–3265.

ANSYS.Inc. Ansys fluent theory guide. release 2022 r2.

Burton, W. K., Cabrera, N., Frank, F. C., and Mott, N. F. The growth of crystals and the equilibrium structure of their surfaces. 243(866):299–358. Publisher: Royal Society.

Cahn, J. W., Hillig, W., and Sears, G. The molecular mechanism of solidification. 12(12):1421–1439.

Cai, L., Mi, S., and Luo, C. (2023). Study on enhanced heat transfer of a phase change material slurry in transverse corrugated tubes. 226:120293.

Dorsey, N. E. The freezing of supercooled water. 38(3):247–328. Publisher: American Philosophical Society.

Du, Q., Chen, M., Song, W., Qin, K., and Feng, Z. (2023). Investigation on the evolution of ice particles and ice slurry flow characteristics during subcooling release. 209:124008.

Fernandez, R. and Barduhn, A. The growth rate of ice crystals. 3(3):330–342.

Fisher, J. C., Hollomon, J. H., and Turnbull, D. Rate of nucleation of solid particles in a subcooled liquid. 109(2825):168–169. Publisher: American Association for the Advancement of Science.

Fleiter, T., Steinbach, J., Ragwitz, M., Dengler, J., Köhler, B., Dinkel, A., Bonato, P., Azam, N., D, K., and Al, E. Mapping and analyses of the current and future (2020-2030) heating / cooling fuel deployment (fossil / renewables). work package 1: Final energy consumption for the year 2012. Publisher: European Commission.

Ghadiri, M. and Zhang, Z. Impact attrition of particulate solids. part 1: A theoretical model of chipping. 57(17):3659–3669.

Gibbs, J. W. On the equilibrium of heterogeneous substances. Publisher: Heidelberg University Library.

Giberti, F. Computer simulations of homogeneous nucleation. Accepted: 2017-06-14T01:22:52Z.

Gidaspow, D. *Multiphase flow and fluidization: continuum and kinetic theory descriptions*. Academic Press.

Gidaspow, D., Bezburuah, R., and Ding, J. Hydrodynamics of circulating fluidized beds: Kinetic theory approach. Number: CONF-920502-1 Publisher: Illinois Institute of Technology. Department of Chemical Engineering.

Gunn, D. J. (1978). Transfer of heat or mass to particles in fixed and fluidised beds. 21(4):467–476.

Gurruchaga, I. and Carbonell, D. (2024). Modicecrys - cfd numerical modelling and experimental analysis of ice crystallizers for supercooling flows. Technical report, SPF-OST.

Gurruchaga, I., Carbonell, D., Arenas, M., Pena, X., and Alonso, L. (2023). TRI-HP Deliverable D7.10 - Potential benefits of TRI-HP systems around Europe. Technical report, SPF-OST.

Higashitani, K., Yamauchi, K., Matsuno, Y., and Hosokawa, G. Turbulent coagulation of particles dispersed in a viscous fluid. 16(4):299–304.

Ivantsov, G. P. Temperature field around a spherical, cylindrical, and needle-shaped crystal, growing in a pre-cooled melt. Publication Title: Temperature field around a spherical Volume: 58 ADS Bibcode: 1985tfas.rept..567I.

Kallungal, J. P. and Barduhn, A. J. Growth rate of an ice crystal in subcooled pure water. 23(3):294–303.

Kamiya, G. and Coroamă, V. C. Data Centre Energy Use: Critical Review of Models and Results.

Kauffeld, M., Kawaji, M., and Egolf, P. W. *Handbook on ice slurries: fundamentals and engineering*. International Institute of Refrigeration. OCLC: 833158681.

Kauffeld, M., Wang, M. J., Goldstein, V., and Kasza, K. E. (2010). Ice slurry applications. *International Journal of Refrigeration*, 33(8):1491–1505.

Kozawa, Y., Aizawa, N., and Tanino, M. (2005). Study on ice storing characteristics in dynamic-type ice storage system by using supercooled water.: Effects of the supplying conditions of ice-slurry at deployment to district heating and cooling system. *International journal of refrigeration*, 28(1):73–82.

Kurz, W. *50 Year's Solidification Research The Dendrite Growth Problem between Brighton and Old Windsor*.

Kähler, C. J., Scharnowski, S., and Cierpka, C. (2012). On the resolution limit of digital particle image velocimetry. 52(6):1629–1639.

Langer, J. and Müller-Krumbhaar, J. Stability effects in dendritic crystal growth. 42:11–14.

Langer, J. S. and Müller-Krumbhaar, H. Theory of dendritic growth—i. elements of a stability analysis. 26(11):1681–1687.

Langer, J. S., Sekerka, R. F., and Fujioka, T. Evidence for a universal law of dendritic growth rates. 44(4):414–418.

LaVision (2023). 1003029_imagerproplus_imagerprox_d11 product manual imager pro plus & imager pro x.

Legawiec, B. and Ziólkowski, D. (1994). Structure, voidage and effective thermal conductivity of solids within near-wall region of beds packed with spherical pellets in tubes. 49(15):2513–2520.

Lehr, F., Millies, M., and Mewes, D. Bubble-size distributions and flow fields in bubble columns. 48(11):2426–2443. _eprint: https://onlinelibrary.wiley.com/doi/pdf/10.1002/aic.690481103.

Liao, Y., Rzehak, R., Lucas, D., and Krepper, E. Baseline closure model for dispersed bubbly flow: Bubble coalescence and breakup. 122.

Lun, C. K. K., Savage, S. B., Jeffrey, D. J., and Chepurniy, N. Kinetic theories for granular flow: inelastic particles in couette flow and slightly inelastic particles in a general flowfield. 140:223–256.

Luo, H. Coalescence, breakup and liquid circulation in bubble column reactors. \textbar national technical reports library - NTIS.

Mazzotti, M., Vetter, T., and Ochsenbein, D. R. Crystallization process modeling. In Hilfiker, R. and Raumer, M. V., editors, *Polymorphism in the Pharmaceutical Industry*, pages 285–304. Wiley, 1 edition.

Niezgoda-Żelasko, B. (2006). Heat transfer of ice slurry flows in tubes. 29(3):437–450.

Niezgoda-Żelasko, B. and Zalewski, W. (2006). Momentum transfer of ice slurry flows in tubes, experimental investigations. 29(3):418–428.

Němec, T. Estimation of ice–water interfacial energy based on pressure-dependent formulation of classical nucleation theory. 583:64–68.

Prince, M. Bubble coalescence and break-up in air-sparged bubble columns.

Reitze, F. Endenergiebedarf zur prozesskälteerzeugung, effizienzpotentiale, sowie hemmende faktoren für den einsatz von effizienter kältetechnologie im GHD-sektor und bei milchproduzierenden betrieben in deutschland in der periode 2008 - 2020.

Saffman, P. G. and Turner, J. S. On the collision of drops in turbulent clouds. 1(1):16–30.

Sari, O., Vuarnoz, D., Meili, F., and Egolf, P. (2000). Visualization of ice slurries and ice slurry flows.

Scharnowski, S. and Kähler, C. J. (2020). Particle image velocimetry - classical operating rules from today's perspective. 135:106185.

Shibkov, A., Golovin, Y., Zheltov, M., Korolev, A., and Leonov, A. Morphology diagram of nonequilibrium patterns of ice crystals growing in supercooled water. 319:65–79.

Shibkov, A., Zheltov, M., Korolev, A., Kazakov, A., and Leonov, A. Crossover from diffusion-limited to kinetics-limited growth of ice crystals. 285(1):215–227.

Shibkov, A. A., Zheltov, M. A., Korolev, A. A., Kazakov, A. A., and Leonov, A. A. Effect of surface kinetics on the dendritic growth of ice in supercooled water. 49(6):1056–1063.

Shubert, M., Ruesch, F., and Carbonell, D. (2020). *Ice-Grids - Implementation of ice storage tanks into 5GDHC networks as seasonal storage or load shifting element*. Institut für Solartechnik SPF for Swiss Federal Office of Energy (SFOE), Research Programme Solar Heat and Heat Storage, CH-3003 Bern.

Smoluchowski, M. v. Versuch einer mathematischen theorie der koagulationskinetik kolloider lösungen. 92:129–168. Publisher: Geest & Portig.

Stamatiou, E., Meewisse, J. W., and Kawaji, M. (2005). Ice slurry generation involving moving parts. *International Journal of Refrigeration*, 28(1):60–72.

Syamlal, M., Rogers, W., and O'Brien, T. MFIX documentation theory guide.

Vuarnoz, D., Sari, O., Egolf, P. W., and Liardon, H. (2002). ULTRASONIC VELOCITY PROFILER UVP-XW FOR ICE- SLURRY FLOW CHARACTERISATION.

Wang, T., Lü, Y., Ai, L., Zhou, Y., and Chen, M. Dendritic growth model involving interface kinetics for supercooled water. 35(15):5162–5167. Publisher: American Chemical Society.

Xie, F., Guo, W., and Zhu, Y. (2023). Numerical study on flow-melt characteristics of ice slurry in horizontal straight pipe with a local large heat flux segment. 16(1):476.

Xu, A., Liu, Z., Zhao, T., and Wang, X. Population balance model of ice crystals size distribution during ice slurry storage. 22(2):1440001. Publisher: World Scientific Publishing Co.

Xu, D., Liu, Z., Cai, L., Tang, Y., Yu, Y., and Xu, A. A CFD-PBM approach for modeling ice slurry flow in horizontal pipes. 176:546–559.

7 Annexes

7.1 Ice growth modelling

7.1.1 Nucleation

There are two different nucleation mechanisms: *homogeneous* and *heterogeneous* nucleation.

- The *homogeneous nucleation* occurs spontaneously in the aforementioned metastable state of supercooled water when stochastic spatial fluctuations form "isolated singularities" of water molecules, called *embryos* which transform into ice (Dorsey). These embryos, depending on size and shape, may decay and redissolve into the parent phase again, or grow, and turn into a stable *nucleus*, depending on the local balance of the *Gibbs free energy* of nucleation (Kauffeld et al.).
- The *heterogeneous nucleation* initiates from a foreign substrate (a boundary such as a wall, another particle or seed in the aqueous solution). A special case of heterogeneous nucleation is the *secondary nucleation* where nucleation is triggered by a previously formed crystal.

Homogeneous Nucleation

The Classic Nucleation Theory (CNT) explains *nucleation* in terms of Gibbs free energy G, considering two counteracting free energy factors: the variation of the volume free energy, ΔG_V, J, and the surface free energy ΔG_S, J, (Fisher et al.). During the phase transition from water to ice state, the Gibbs free energy of the *liquid* water molecules is released due to the lower free energy of *solid* ice, while some free energy is required for the creation of a new interface that splits the two phases: water and ice. The expression reads as:

$$\Delta G = -\Delta G_V + \Delta G_S \tag{15}$$

In the case of the formation of a small ice nucleus with a spherical shape from a purely metastable state in homogeneous nucleation, the expression can be rewritten as the following:

$$\Delta G = -V\ \Delta G_{V'} + A\ \Delta G_{S'} = -\frac{4}{3}\pi r_n^3\ \Delta G_{V'} + 4\pi r_n^2\ \gamma_{iw} \tag{16}$$

where $\Delta G_{V'}$ and $\Delta G_{S'}$ are the variation in the volume and surface free energy in relative volume and area units respectively $\Delta G_{V'}$ is in $\mathrm{J\,m^{-3}}$, $\Delta G_{S'}$ in $\mathrm{J\,m^{-2}}$, r_n is the radius of the small nucleus in m, and γ_{iw} is the interfacial tension, $\mathrm{J\,m^{-2}}$, (the surface free energy required) between the small nucleus and the supercooled water.

For the volume of free energy released by the small nucleus, the general expression for the change in Gibbs free energy can be used, where H is enthalpy, J, T the temperature, in K and S is entropy $\mathrm{J/K^{-1}}$:

$$\Delta G_{V'} = \rho \cdot (\Delta H - T \cdot \Delta S) \tag{17}$$

Developing the previous:

$$\Delta G_{V'} = \rho \cdot ((H_{wat} - H_{ice}) - T_{sc} \cdot (S_{wat} - S_{ice})) = \rho \cdot (\Delta h_{fus} - T_{sc}\frac{h_{fus}}{T_m}) = \rho \cdot h_{fus}(1 - \frac{T_{sc}}{T_m}) = \frac{\rho\ h_{fus}\Delta T_{sc}}{T_m} \tag{18}$$

where $_{wat}$ and $_{ice}$ subindexes refer to water and ice respectively, ρ is the density of water, $\mathrm{kg\,m^{-3}}$, h_{fus} is the enthalpy of fusion, $\mathrm{J\,kg^{-1}}$, T_m the melting temperature, K, T_{sc} the supercooled water temperature, K, and ΔT_{sc} the supercooling degree $T_m - T_{sc}$. Substituting in equation (15):

$$\Delta G = -\frac{4}{3}\pi r_n^3\ \frac{\rho\ h_{fus}\Delta T_{sc}}{T_m} + 4\pi r_n^2\ \gamma_{iw} \tag{19}$$

From the previous expression, it can be stated that homogeneous nucleation depends basically on the supercooling degree ΔT_{sc} and interfacial energy between ice and water γ_{iw}. In Fig. 32, it is shown how different free energy for nucleation are required depending on different interfacial energy between ice and water γ_{iw}.

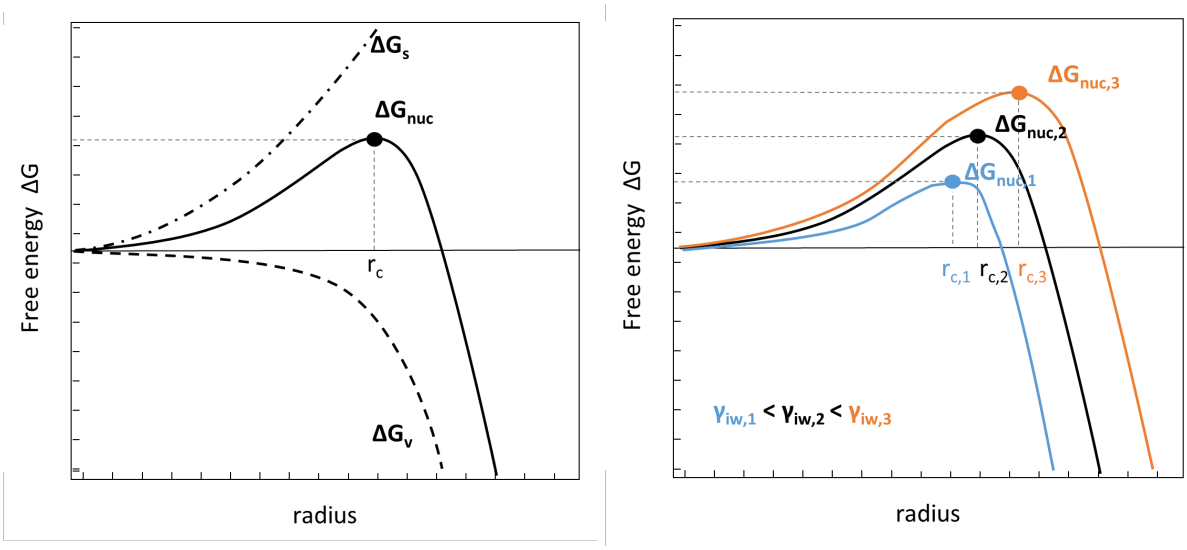

Figure 32: *Left*: Sketch of the free energy of nucleation composed by the balance of volume and surface Gibbs free energy. The critical radius r_c for homogeneous nucleation is derived for $\partial(\Delta G)/\partial r = 0$. Spontaneous crystal growth starts from $\Delta G < 0$, previously the free energy of nucleation ΔG_{nuc} should be met for achieving the r_c. *Right*: Different free energy of nucleation $\Delta G_{nuc,1,2or3}$ result depending on different interfacial energy between ice and water $\gamma_{iw,1,2or3}$ *

For obtaining the critical radius r_c, above which the nucleation process releases energy and the spontaneous growth of the nucleus occurs, the Eq. 19 is derived for $\partial(\Delta G)/\partial r = 0$ obtaining.

$$r_c = \frac{2\ \gamma_{iw}\ T_m}{\rho\ h_{fus} \Delta T_{sc}} \tag{20}$$

The free energy of nucleation ΔG_{nuc} is the amount of free energy required for creating the minimum nucleus with the potential to grow, which equals the energy required for creating the interface minus the energy released. Thus, ΔG_{nuc} is obtained replacing the r_c from Eq. 20 into the r in 19 resulting in:

$$\Delta G_{nuc} = \frac{16\pi}{3} \frac{\gamma_{iw}^3\ T_m^2}{(\rho\ h_{fus} \Delta T)^2} \tag{21}$$

Assuming an ice water interfacial energy γ_{iw} of 29.1 J m^{-2} (Němec) the critical radius and the values of the nucleation energy are shown in Table. 3.

Table 3: Critical radius and free energy of nucleation for homogeneous nucleation.

Temperature T °C	**Critical radius** r_c nm	**Number of molecules** n -	**Energy of nucleation** ΔG_{nuc} J
-40	1.19	237	5.2065E-14
-20	2.38	1'895	2.6830E-13
-5	9.54	121'269	4.2716E-12
-3	15.9	561'431	1.1911E-11
-2.5	19.08	970'153	1.71521E-11
-2	23.85	1'894'831	2.6800E-11
-1.5	31.79	4'491'451	4.7645E-11
-1	47.69	15'158'647	1.0720E-10
-0.5	95.38	121'269'173	4.2880E-10

Derivations of Eq. 19, Eq. 20 and Eq. 21 must be considered only for the assumption of the spherical shape of small embryos or nucleus. For other non-spherical-like aspect assumptions as in the case of nucleation

of needle, disks or platelet-like crystals, other equations could be derived as presented in Giberti. As a consequence, different solutions of r_c and ΔG_{nuc} would be obtained as shown in Fig. 33.

Indeed, in the same reference (Giberti) another way of expressing the equation (19) in terms of the number of constituents (number of molecules) instead of the critical radius r_c is chosen, and converts that expression into a geometrical-shape-independent formulation, which is more useful in case of polymorphism.

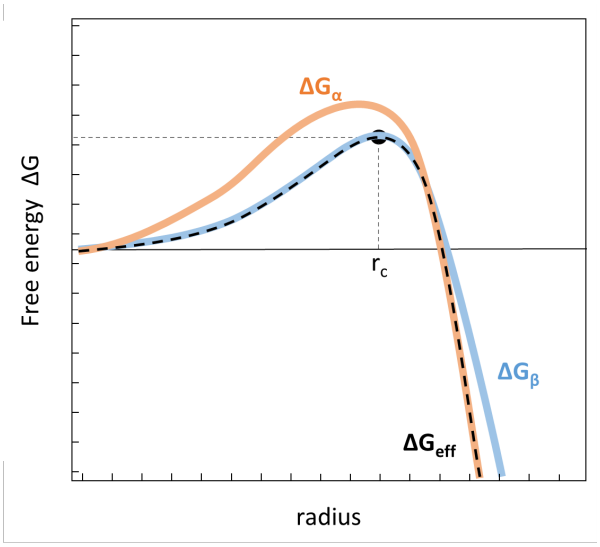

Figure 33: Two polymorphism, α and β possess two different free energy of nucleation ΔG_{nuc}. α is more stable than β, and consequently, when nucleation occurs, the first polymorph to nucleate is β, which turns into α as soon as the two resulting free energy curves cross each other (ΔG_{eff}).

Heterogeneous Nucleation

For heterogeneous nucleation, which describes nucleation at foreign surfaces, the free energy of nucleation is lower than that of homogeneous nucleation by a factor f_{het} which $0 \leq f_{het} \leq 1$ that depends on the interface and the geometry of the surface.

$$\Delta G_{het} = f_{het} \cdot \Delta G_{nuc} \tag{22}$$

For the simplified case of a smooth surface shown in Fig. 34 the f can be expressed in terms of the wetting angle θ_{wett}:

$$f_{het} = \frac{1}{4}(2 + cos\ \theta_{wett}) \cdot (1 - cos\ \theta_{wett})^2 \tag{23}$$

The $cos\ \theta_{wett}$ depends on interfacial energy between ice and water γ_{iw}, and likewise for every water's phase with the surface γ_{isurf} , γ_{wsurf}, in agreement with Young's equation:

$$cos\ \theta_{wett} = \frac{\gamma_{wsurf} - \gamma_{isurf}}{\gamma_{wi}} \tag{24}$$

For wetting angles of $\theta_{wett} = \frac{\pi}{2}$, $f_{het} = 0.5$ and then $\Delta G_{het} = 0.5 \cdot \Delta G_{nuc}$, thus, resulting in heterogeneous nucleation being half of the homogeneous equivalent. This lowered energy step involves that heterogeneous nucleation requires normally lower degrees of supercooling (or supersaturation) compared to homogeneous nucleation.

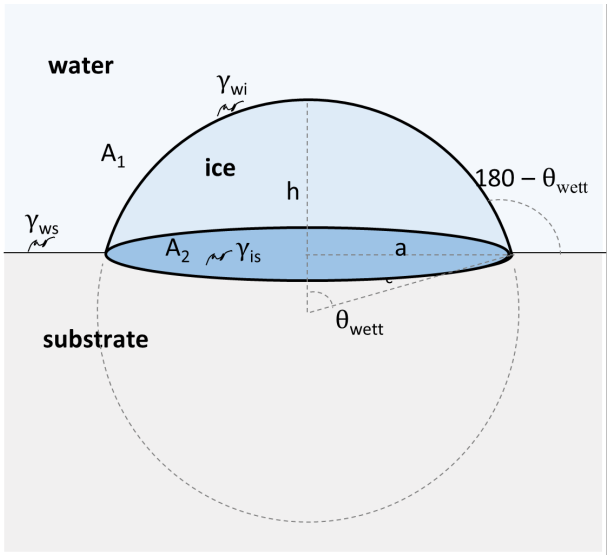

Figure 34: Surface balances for heterogeneous nucleation.

7.1.2 Crystal growth

The crystal growth mechanisms have been a question of interest for decades. Since J.W. Gibbs settled the basis of the thermodynamic equilibrium applied to chemical reactions and phase transitions by the end of 19th century (Gibbs), crystal growth has been the main topic of a vast number of researchers.

Since mid 20th century, there was an increasing number of investigations, both experimental and theoretical, which were conducted to explore the thermophysical and kinetic dependencies of crystal growth rates. Burton, Cabrera, and Frank developed the *BCF theory* in the 1950s (Burton et al.), which provided a fundamental framework for understanding crystal growth by atomic processes approach. Other researchers like Dorsey, Fisher et al. or Cahn et al. assumed a power-law-type relationship between the velocity growth rate v_{tip} and bulk supercooling temperature ΔT_{sc} in the form: $v_{tip} = a \cdot \Delta T_{sc}^{b}$, where a and b were empirically determined, resulting in empirical correlations that effectively captured the experimental data. These first experiences were useful in providing the first experimental crystal growth references, but their universal applicability beyond the framework of their experimental conditions (fluid material, fluid velocities, supercooling temperatures, experimental setups, etc.), was a matter of questioning and continuous further research. Furthermore, these empirical expressions, although useful, offered limiting profound insights into the intrinsic crystal growth process.

Papapetrou is credited with solving, in 1935, the growth rate for a dendrite with a cylindrical tip Akhtar et al., Kurz, Wang et al.. However, this contradicted experimental observations that favoured a parabolic tip shape. Ivantsov addressed this by formulating the *Stefan's problem* and solving the dendritic growth for a parabolic tip shape in 1947. Nevertheless, his solution was valid only for a range of values for the dendritic growth rate and dendritic curvature radius.

In the 1960s-1970s, experimental studies on crystal growth gained relevance: advances in experimental techniques, including microscopy and controlled environment experiments, allowed scientists to observe and measure crystal growth more accurately e.g. (Fernandez and Barduhn). Kallungal and Barduhn considered the flow velocity v in the form: $v_{tip} = a \cdot \Delta T_{sc}^{b} \cdot v^{c}$ on the traditional power-law-type relationship between growth rate of the tip dendrite v_{tip} and bulk supercooling temperature. Likewise, the coefficients a, b and c were empirically determined by fitting the experimental data.

The *LM-K theory*, which takes its name from its authors: Langer and Müller-Krumbhaar, provided a universal model for dendritic growth rate based on stability constant in the 1970s, Langer and Müller-Krumbhaar (a), Langer et al. and Langer and Müller-Krumbhaar (b). This theory contributed to the understanding of dendritic growth in various materials. This model was an important landmark but did not include curvature effects or molecular kinetics, which appear to be significant limitations to the model beyond a supercooling

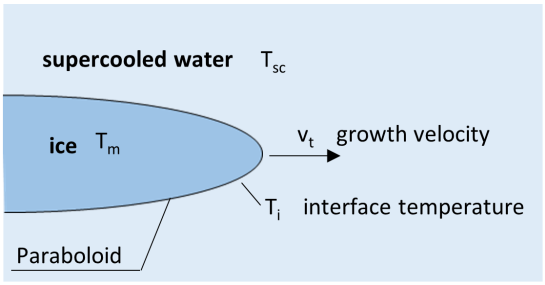

Figure 35: Dentrite crystal form as a paraboloid of revolution.

temperature.

To solve this limitation to the LM-K theory, Shibkov highlighted the need to consider the transition from diffusion to kinetics limited regimes at higher supercooling degrees, prompting the need to incorporate kinetic effects. This *crossover*, using Shibkov's own term, from diffusion to kinetics limited growth rate of ice crystals occurs above a supercooling temperature $\Delta T_{sc} > 4$ K to 5 K (Shibkov et al., b,c). A couple of years before, Shibkov had also analysed the *polymorphism*, the dependence between the different macroscopic structures: dendrite, needle-like crystal, fractal needled branch or platelet, and the supercooling degree in a morphology diagram of growth patterns (Shibkov et al., a). These different morphologies and growth patterns of ice are shown in Fig. 36 as a function of the supercooling degree ΔT_{sc}.

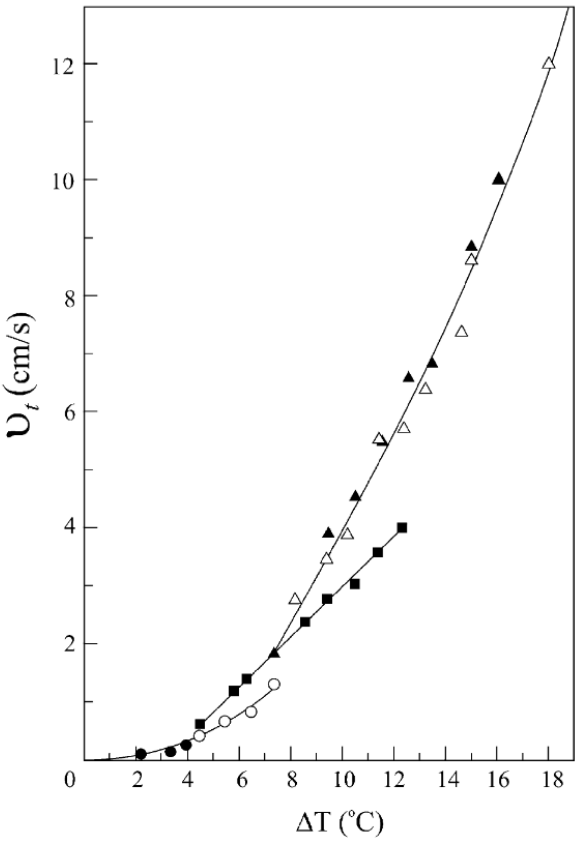

Figure 36: Morphology diagram of growth patterns from Shibkov et al. (a). (•) Dendrite, (○) needle-like crystal, (■) fractal needled, (△) compact needled or (▲) platelet, depending on supercooling degree ΔT_{sc}.

In Fig. 37 it can be seen that below a certain supercooling temperature, the LM-K theory is valid and reproduces the experimental data correctly. Based on that, it can be stated that for low supercooling rates, the diffusive heat transfer effect is the limiting factor for crystal growth, while for higher supercooling temperatures, the limiting factor is related to molecular kinetic. Thus, for higher supercooling degrees, regardless the morphology, what should be considered is the kinetic effect of the crystal's growth rate.

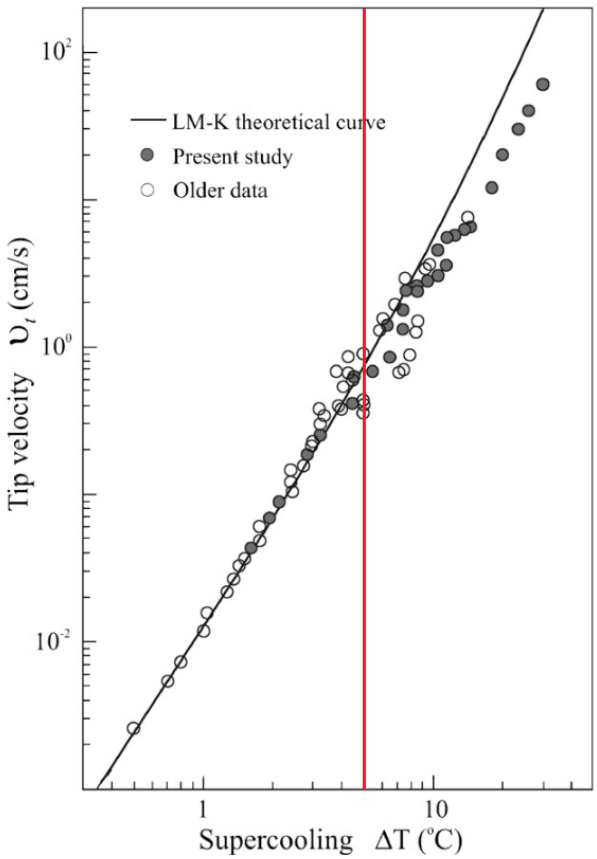

Figure 37: Comparison between experimental data and the LM-K theory (in solid line). Filled or unfilled correspond to different experimental data (the filled ones to Shibkov's study, and the unfilled ones to the previous analysis. Based on the figure from Shibkov et al. (a). It is shown how below a certain supercooling temperature ΔT_{sc} = 5 K, drawn as a red line, the LM-K theory is valid and beyond there is a discrepancy with the experimental data.

These kinetic effects in dendritic growth can be addressed by means of the linear kinetic theory or by means of the Wilson-Frenkel model. As described by Akhtar et al.: *"While both theories consider the effect of attachment kinetics in their formulation, the Wilson-Frenkel model has been demonstrated to predict the growth rates well for liquids with Lennard-Jones potential such as water."* Other authors, Wang et al. have suggested similar solutions, by modifying the interface temperature, in order to add the kinetic limitation.

Although the LM-K theory is flawed for its non-consideration of the kinetic effects, which would not be suited for higher supercooling degrees, for applications where the ΔT_{sc} is below 4 K, it is accurate enough.

The Langer and Müller-Krumbhaar (LM-K) theory

The LM-K theory finds a solution, in steady state, for a crystal in the form of a paraboloid of revolution, in a dendrite shape form, that grows with a constant velocity of its tip, v_{tip}. This solution is represented overlaying experimental data in Fig. 37.

The LM-K theory establishes a stability constant $\sigma_{LM-K} = 1/(4\pi^2) = 0.0253$ which determines the tip radius r_{tip} and growth rate v_{tip} for a given supercooling ΔT_{sc} independent of the time of the dendrite evolution.

As described in Shibkov et al. (c), in Ivantsov's solution the dimensionless supercooling temperature is defined as follows:

$$\Delta_{p_e} = \frac{\Delta T_{sc} \cdot c_{p,wat}}{h_{fus}} \tag{25}$$

where $c_{p,wat}$ is the heat capacity of water and h_{fus} is the enthalpy of fusion. This dimensionless supercooling temperature, Δ_{p_e} is related to Péclet adimensional number with the following expression:

$$\Delta_{p_e} = p_e \cdot \exp(p_e) \cdot \int_{p_e}^{\infty} \exp(-x)/x \, dx \tag{26}$$

The *Péclet* number is defined as the ratio of the rate of advection (convection) to the rate of diffusion, and it is given by the formula:

$$p_e = (v_{tip} \cdot r_{tip})/(2 \cdot \alpha_{diff,wat}) \tag{27}$$

where α_{diff} is the thermal diffusivity of water $_{wat}$.

The stability constant of the LM-K theory σ_{LM-K} is equal to:

$$\sigma_{LM-K} = 2 \cdot \alpha_{diff,wat} \cdot d_0/(v_{tip} \cdot r_{tip}^2) \tag{28}$$

where d_0 is the capillary length (which determines the surface tension forces' radius of action, calculated with the T_m is the melting temperature, as follows:

$$d_0 = T_m \cdot \gamma_{iw} \cdot c_{p,wat}/h_{fus}^2 \tag{29}$$

Regression models for the LM-K theory

To facilitate the implementation of the crystal growth rate, formulated under LM-K theory, into the CFD model, a regression model is required. Three regression models: Reg1, Reg2 and Reg3, have been proposed, including second-order polynomials represented by the equation $y = a_2 \cdot x^2 + a_1 \cdot x + a_0$, as well as potential regression forms given by $y = a \cdot x^b$ regression form. Some of these models (Reg1) are specifically adjusted for the degree of supercooling within the range of $0\,^{\circ}\mathrm{C}$ to $7\,^{\circ}\mathrm{C}$ range, and others (Reg2 and Reg3) more specifically for the range between $0\,^{\circ}\mathrm{C}$ to $3\,^{\circ}\mathrm{C}$. The following are the regression models:

$$v_{t,Reg1} = 1.2672\text{e}{-04} \cdot \Delta T_{sc}^{2.5122} \tag{30}$$

$$v_{t,Reg2} = 1.2613\text{e}{-04} \cdot \Delta T_{sc}^{2.4854} \tag{31}$$

$$v_{t,Reg3} = 3.0656\text{e}{-01} \cdot \Delta T_{sc}^2 - 2.9147\text{e}{-01} \cdot \Delta T_{sc} + 8.3465\text{e}{-02} \tag{32}$$

where T_{sc} in the supercooling degree °C and v_t the growth rate in $\mathrm{m\,s^{-1}}$.

Fig. 38 shows the tip velocity growth rate values obtained in $\mathrm{mm\,s^{-1}}$ from the LM-K theory and different regression models depending on the supercooling degree ΔT_{sc}.

As presented in Table Tab. 4, all three regression models have been assessed using the $error$ function RMSE for three distinct application ranges of supercooling degree. This evaluation aims to identify the regression model that best fits the data depending on the supercooling degree range of application. Based on the numerical values of the tip velocity growth rate presented in this table, it can be concluded that Reg1, despite being adjusted for $\Delta T_{sc} < 7\ ^{\circ}\mathrm{C}$ provides the best fit for the range $\Delta T_{sc} < 3\ ^{\circ}\mathrm{C}$, with an RMSE of $5.1\ \%$. However, in the range $\Delta T_{sc} < 4\ ^{\circ}\mathrm{C}$, Reg2 yields a lower RMSE of $8.7\ \%$ compared to $10.3\ \%$ of Reg1, making Reg2 the preferred choice over Reg1. Reg3 is ultimately discarded due to its poor performance for $\Delta T_{sc} < 1\ ^{\circ}\mathrm{C}$, where it exhibits a minimum v_t growth rate at $\Delta T_{sc} = 0.5\ ^{\circ}\mathrm{C}$, a behaviour that lacks of physical relevance. No regression performs adequately for $\Delta T_{sc} > 4\ ^{\circ}\mathrm{C}$. Thus, alternative equations should be considered if required.

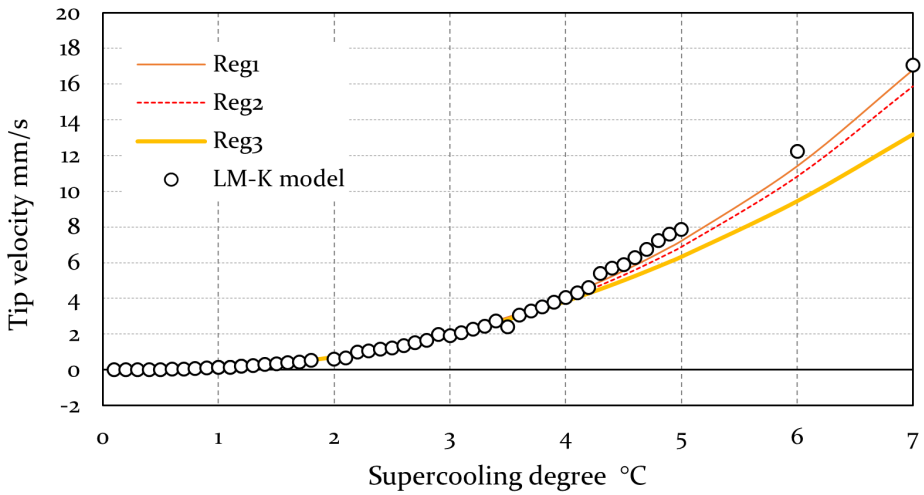

Figure 38: Comparison between tip velocity growth rate values obtained from the LM-K theory and different regression models depending on the supercooling degree ΔT_{sc}.

Table 4: Tip velocity growth rate for the LM-K theory and different regression models depending on the supercooling degree ΔT_{sc}.

Supercooling degree °C	**LM-K model** mm/s	**Reg1** mm/s	**Reg2** mm/s	**Reg3** mm/s
0.1	0.0004	0.0004	0.0004	0.0574
0.2	0.0026	0.0022	0.0023	0.0374
0.3	0.0065	0.0062	0.0063	0.0236
0.4	0.0135	0.0127	0.0129	0.0159
0.5	0.023	0.0222	0.0225	0.0144
0.6	0.0387	0.0351	0.0354	0.0189
0.7	0.0529	0.0517	0.052	0.0297
0.8	0.0746	0.0723	0.0724	0.0465
0.9	0.0957	0.0973	0.0971	0.0695
1	0.1311	0.1267	0.1261	0.0986
1.1	0.1378	0.161	0.1598	0.1338
1.2	0.2001	0.2003	0.1984	0.1751
1	0.1311	0.1267	0.1261	0.0986
1.1	0.1378	0.161	0.1598	0.1338
1.2	0.2001	0.2003	0.1984	0.1751
1.3	0.258	0.245	0.2421	0.2226
1.4	0.2966	0.2951	0.2911	0.2763
1.5	0.3336	0.3509	0.3455	0.336
1.6	0.3956	0.4127	0.4056	0.4019
1.7	0.4558	0.4806	0.4716	0.4739
1.8	0.5545	0.5548	0.5436	0.5521
2	0.6008	0.7229	0.7063	0.7268
2.1	0.6641	0.8172	0.7974	0.8233
2.2	0.9914	0.9185	0.8951	0.926
2.3	1.074	1.027	0.9997	1.0348
2.4	1.167	1.1429	1.1112	1.1497
2.5	1.223	1.2663	1.2299	1.2708
2.6	1.348	1.3975	1.3558	1.398
2.7	1.51	1.5364	1.4891	1.5313
2.8	1.645	1.6834	1.63	1.6708
2.9	1.976	1.8386	1.7785	1.8164
RSME $\Delta T_{sc} < 3$ °C		5.1 %	5.3 %	5.5 %
3	1.905	2.002	1.9349	1.9681
3.1	2.081	2.1739	2.0992	2.1259
3.2	2.266	2.3544	2.2715	2.2899
3.3	2.46	2.5436	2.4521	2.4601
3.4	2.757	2.7417	2.6409	2.6363
3.5	2.402	2.9489	2.8382	2.8187
3.6	3.059	3.1651	3.0441	3.0072
3.7	3.306	3.3906	3.2586	3.2018
3.8	3.537	3.6256	3.4819	3.4026
3.9	3.79	3.8701	3.7141	3.6095
RSME $\Delta T_{sc} < 4$ °C		10.3 %	8.7 %	9.8 %
4	4.054	4.1242	3.9553	3.8225
4.1	4.33	4.3881	4.2056	4.0417
4.2	4.619	4.662	4.4652	4.267
4.3	5.393	4.9459	4.7341	4.4984
4.4	5.691	5.2399	5.0125	4.736
4.5	5.887	5.5443	5.3005	4.9797
4.6	6.298	5.859	5.598	5.2295
4.7	6.746	6.1843	5.9054	5.4855
4.8	7.237	6.5202	6.2226	5.7476
4.9	7.613	6.8668	6.5499	6.0158
5	7.874	7.2243	6.8871	6.2901
RSME $\Delta T_{sc} < 5$ °C		23.9 %	33.7 %	50.3 %

7.2 CFD model development

NOTE: For clarity, the subscripts $_l$ and $_s$ will be used to denote the liquid and solid phases, respectively, in the following sections. The subscript $_q$ denotes independently of either phase.

7.2.1 Mass conservation equation

The conservation of mass states that mass is neither created nor destroyed, the mass of any fluid parcel remains constant over time. The mass conservation equation, also known as *Continuity equation*, for **unsteady** and **three-dimensional** domain for the liquid and solid phases of ice slurry, is formulated assuming an **incompressible** fluid [4] is given by the following Eulerian formulation equations for multiphase flows:

$$\frac{\partial}{\partial t}(\alpha_l \rho_l) + \nabla \cdot (\alpha_l \rho_l \vec{u}_l) = \dot{m}_{s,l} \tag{33}$$

$$\frac{\partial}{\partial t}(\alpha_s \rho_s) + \nabla \cdot (\alpha_s \rho_s \vec{u}_s) = \dot{m}_{l,s} \tag{34}$$

$$\dot{m}_{s,l} = -\dot{m}_{l,s} \tag{35}$$

where ρ_q is the density of the phase where the subscript q denotes the phase either liquid or solid, $\mathrm{kg\,m^{-3}}$, α_q is the volume fraction, $\mathrm{m^3\,m^{-3}}$, $\vec{u}_q$ is the velocity vector in$\mathrm{m\,s^{-1}}$, and $\dot{m}_{s,l}$ is the volumetric mass transfer from $_s$-phase to $_l$-phase and vice versa, $\mathrm{kg\,s^{-1}\,m^{-3}}$.

The first term on the left side of Eq. (33) and (34) $\frac{\partial}{\partial t}(\alpha_q \rho_q)$ represents the variation of density of each $_q$-phase over time, the *accumulation term*, due to i.e. changes in temperature. The second term $\nabla \cdot (\alpha_q \rho_q \vec{u}_q)$ states for the transport of mass by the fluid flow, the *advection* or *convection term*. The right side of the equation refers to the generation or destruction of mass due to the phase change between the liquid and solid phases, commonly referred as the *source term* of the equation.

The sum of volume fractions of each phase within the same fluid parcel domain is equal to one:

$$\alpha_l + \alpha_s = 1 \tag{36}$$

7.2.2 Momentum conservation equation

The momentum conservation equation for each phase, is given by:

$$\frac{\partial}{\partial t}(\rho_l \alpha_l \vec{u}_l) + \nabla \cdot (\rho_l \alpha_l \vec{u}_l \vec{u}_l) = -\alpha_l \nabla p + \nabla \cdot \bar{\bar{\tau}}_l + \alpha_l \rho_l \vec{g} + k_{s,l}(\vec{u}_s - \vec{u}_l) + (\dot{m}_{s,l}\vec{u}_s - \dot{m}_{l,s}\vec{u}_l) \tag{37}$$

$$\frac{\partial}{\partial t}(\rho_s \alpha_s \vec{u}_s) + \nabla \cdot (\rho_s \alpha_s \vec{u}_s \vec{u}_s) = -\alpha_s \nabla p - \nabla p_s + \nabla \cdot \bar{\bar{\tau}}_s + \alpha_s \rho_s \vec{g} + k_{l,s}(\vec{u}_l - \vec{u}_s) + (\dot{m}_{l,s}\vec{u}_l - \dot{m}_{s,l}\vec{u}_s) \tag{38}$$

where p is the static pressure shared by all phases, liquid and solid in Pa = $\frac{kg}{m.s^2}$, p_s is the solid pressure for *granular flow* in Pa (see Sec. 7.2.8), $\bar{\bar{\tau}}_q$ is the stress-strain tensor for the q-phase, in Pa. As the gradient or divergence operator $nabla$**!** is in $\mathrm{m^{-1}}$, the resulting equations terms' units, along the remaining terms, are expressed in $\mathrm{kg\,(m\,s)^{-2}}$. The fluid-solid exchange momentum coefficients between the two phases are $k_{l,s}$ or $k_{s,l}$, in $\mathrm{kg\,s^{-1}\,m^{-3}}$.

The first term of the Eq. (37) and (38) $\frac{\partial}{\partial t}(\rho_q \alpha_q \vec{u}_q)$ in $\mathrm{kg\,(m\,s)^{-2}}$, expresses the variation of momentum of each $_q$ phase over the time in the finite volume, the second term $\nabla \cdot (\rho_q \alpha_q \vec{u}_q \vec{u}_q)$, refers to the transport of momentum by the fluid flow. The first right-hand side term of the equation $-\alpha_q \nabla p$ is the gradient of the pressure scalar field. The term $\nabla \cdot \bar{\bar{\tau}}_q$ accounts for the dissipation of momentum by the viscous forces and $\alpha_q \rho_q \vec{g}$ for the gravity body forces. The exchange of momentum between the two phases is considered by the last two terms. The term with the fluid-solid exchange momentum coefficients accounts for the interphase forces, mainly drag force. The final term in Eq. (37) $(\dot{m}_{s,l}\vec{u}_s - \dot{m}_{l,s}\vec{u}_l)$ and its analogous term in Eq. (38), refers to the momentum exchange regarding the volumetric mass exchange $\dot{m_{s,l}}$ or $\dot{m_{l,s}}$, at velocity $\vec{u}_l$ or $\vec{u}_s$, being transferred from one phase to the other.

[4] that accepts small perturbations in density solution regarding pressure or temperature fields

Stress-strain tensors

The stress-strain tensor for the liquid phase, is given by:

$$\bar{\bar{\tau}}_l = \alpha_l \mu_l \left[\left(\nabla \vec{u}_l + \nabla \vec{u}_l^T \right) - \frac{2}{3} \nabla \cdot \vec{u}_l \cdot \bar{\bar{I}} \right] \tag{39}$$

where μ_l is the dynamic shear viscosity, $\mathrm{kg\,(m\,s)^{-1}}$ or $\mathrm{Pa\,s^{-1}}$, $\vec{u}_l$ refers to the velocity vector $\vec{u}_l = u_{l,x}\vec{i} + u_{l,y}\vec{j} + u_{l,z}\vec{k}$, $\vec{u}_l^T$ the transpose velocity vector and $\bar{\bar{I}}$ the second rank identity tensor. The resulting $\bar{\bar{\tau}}_l$ tensor is in $\mathrm{kg\,(m\,s)^{-2}}$.

For the solid phase in addition to the stress-strain terms from the Eq. 39, solids pressure and bulk viscosity are considered. These terms are the result from the exchange of momentum between particles that must be accounted in stress-strain tensor for a potential dense granular flow. These additional terms: solids pressure and bulk viscosity are considered by making an analogy between the random particle motion arising from the particle-particle collisions and the thermal randomly motion of molecules in a gas, taking into account the inelasticity of the granular phase. The resulting stress-strain tensor for the dense granular solid phase, is given by:

$$\bar{\bar{\tau}}_s = \left(-p_s + \xi \nabla \cdot \vec{u}_s \right) \cdot \bar{\bar{I}} + \alpha_s \mu_s \left[\left(\nabla \vec{u}_s + \nabla \vec{u}_s^T \right) - \frac{2}{3} \nabla \cdot \vec{u}_s \cdot \bar{\bar{I}} \right] \tag{40}$$

where the additional arguments, respect the stress-strain tensor for the liquid phase, are p_s, which corresponds to the solids pressure, in Pa and ξ as the solids bulk viscosity, in $\mathrm{Pa\,s^{-1}}$ described in 7.2.8. The solid shear viscosity μ_s is described in 7.2.3.

7.2.3 Solid shear stresses

The solid shear viscosity is composed by collisional $\mu_{s,col}$, kinetic $\mu_{s,kin}$ and frictional $\mu_{s,fr}$ viscosity components. The collisional and kinetic viscosity components account for the particle momentum exchange due to collisions and translations. A frictional viscosity component is incorporated to capture the viscous-plastic transition that occurs when the solid phase reaches its maximum packing density, that should not occur inside the crystallizer. The three components are combined into the following expression to determine the solids shear viscosity:

$$\mu_s = \mu_{s,col} + \mu_{s,kin} + \mu_{s,fr} \tag{41}$$

Collisional $\mu_{s,col}$, kinetic $\mu_{s,kin}$ and frictional $\mu_{s,fr}$ components, in $\mathrm{kg\,(m\,s)^{-1}}$ or $\mathrm{Pa\,s^{-1}}$, are calculated as the following expressions obtained from Gidaspow et al. for the collisional and Syamlal et al. for the kinetic components:

$$\mu_{s,col} = \frac{4}{5} \alpha_s \rho_s d_s g_{0,ss} (1 + e_{ss}) \sqrt{\frac{\Theta_s}{\pi}} \tag{42}$$

$$\mu_{s,kin} = \frac{d_s \rho_s \sqrt{\theta_s \pi}}{6(3 - e_{ss})} \left[1 + \frac{2}{3} (1 + e_{ss})(3e_{ss} - 1) \alpha_s g_{0,ss} \right] \tag{43}$$

$$\mu_{s,fr} = \frac{p_{fr} sin\varphi}{2\sqrt{I_{2D}}} \tag{44}$$

where α_s is the solid volume fraction $\mathrm{m^3\,m^{-3}}$, ρ_s is the density of the granular material $\mathrm{kg\,m^{-3}}$, d_s is the characteristic diameter of the particles in m, Θ_s is the granular temperature $\mathrm{m^2\,s^{-2}}$, $g_{0,ss}$ is the radial distribution function and e_{ss} is the coefficient of restitution (both non-dimensional and explained in Sec. 7.2.8).

The frictional component $\mu_{s,fr}$ only is considered when the solid volume fraction exceed the packing limit.

7.2.4 Interphase momentum exchange forces

There are different momentum exchange forces that arise due to interactions between the different phases. These forces govern the fluid dynamics of how momentum is transferred between the phases.

- Drag force, is exerted by the fluid on solid particles as the particles move trough the fluid. Drag force transfers momentum from the phase moving faster, slowing it down, to the slower phase, accelerating it.
- Lift force, occurs due to velocity gradient in the fluid flow field or due to rotational effects, and acts perpendicular to the direction of motion. Lift force cause particles to move across streamlines, affecting particle distribution on the flow.
- Collisions between particles, elastic or inelastic, also exchanges momentum among them and should be considered.
- Virtual mass force, occurs when the secondary (solid) phase accelerates relative to the primary (fluid) phase, then the inertia of the primary phase mass opposite a forces to this acceleration. This has a significant effect when the secondary phase has a much smaller density that the primary phase, which is not the case in ice slurry.
- Wall lubrication force, for liquid-gas bubbly flows, the effect of wall lubrication forces on the secondary phases (bubbles), tends to push the bubbles away from walls. For ice slurry does not also apply.

NOTE: In the first version of the model, only the Drag force and Collision between particles are considered, as they are the dominant phenomena.

Drag force

The fluid - solid momentum exchange coefficient $k_{s,l}$ kg s^{-1} m^{-3} used in Eq. (37) and Eq. (38) can be expressed in the general form:

$$k_{s,l} = \frac{\alpha_s \rho_s f}{\tau_s} \tag{45}$$

where α_s is the volume fraction of the solid phase m^3 m^{-3}, ρ_s is the density of the solid phase kg m^{-3}. f is a generalization of different exchange-coefficient models and τ_s is the particle relaxation time s., that is defined as:

$$\tau_s = \frac{\rho_s d_s^2}{18 \mu_l} \tag{46}$$

where d_s is the diameter of particles of the solid phase in m, and μ_l is the dynamic shear viscosity of fluid phase, kg (m s)$^{-1}$.

There are different approaches and models to account for this interphase momentum exchange, as an initial approach and based on the literature review, the Syamlal-O'Brien model will be used in our model. Future research should assess the differences between these models and their resulting behaviours in order to identify the drag model that most accurately represents the behaviour of ice slurry.

Syamlal-O'Brien model

For the Syamlal-O'Brien model Syamlal et al. f is defined as:

$$f = \frac{C_D Re_s \alpha_l}{24 v_{r,s}^2} \tag{47}$$

where α_l is the liquid volume fraction m^3 m^{-3}, C_D is the non-dimensional drag coefficient, and Re_s is the non-dimensional relative Reynolds number as given by:

$$C_D = \left(0.63 + \frac{4.8}{\sqrt{Re_s/v_{r,s}^2}}\right)^2 \tag{48}$$

and

$$Re_s = \frac{\rho_l d_s |\vec{u}_s - \vec{u}_l|}{\mu_l} \tag{49}$$

where $\vec{u}_s$ and $\vec{u}_l$ are the velocities of solid and liquid phases $\mathrm{m\,s^{-1}}$, respectively, ρ_l is the density of the fluid phase $\mathrm{kg\,m^{-3}}$, and d_s is the diameter of the solid phase particles m.

The resulting fluid-solid exchange coefficient states:

$$k_{s,l} = \frac{3\alpha_s\alpha_l\rho_l}{4v_{r,s}^2 d_s} C_D \left(\frac{Re_s}{v_{r,s}}\right) |\vec{u}_s - \vec{u}_l| \tag{50}$$

where $v_{r,s}$ is the terminal velocity in $\mathrm{m\,s^{-1}}$, which correlation is given by the following expression:

$$v_{r,s} = 0.5\left(A - 0.06Re_s + \sqrt{(0.06Re_s)^2 + 0.12Re_s(2B - A) + A^2}\right) \tag{51}$$

where $A = \alpha_l^{4.14}$ and $B = 0.8\alpha_l^{1.28}$ for $\alpha_l \leq 0.85$ or $B = \alpha_l^{2.65}$ for $\alpha_l > 0.85$.

7.2.5 Energy conservation equations

The energy conservation equation for each $_q$-phase is given by:

$$\frac{\partial}{\partial t}\left(\alpha_l\rho_l(e_{i,l} + \frac{\vec{u}_l{}^2}{2})\right) + \nabla\cdot\left(\rho_l\vec{u}_l(h_l + \frac{\vec{u}_l{}^2}{2})\right) = \nabla\cdot(\lambda_l\nabla T_l) + \nabla\cdot(\vec{u}_l\cdot\sigma_l) + h_{sl}(T_l - T_s) + (\dot{m}_{sl}h_s - \dot{m}_{ls}h_l) \tag{52}$$

$$\frac{\partial}{\partial t}\left(\alpha_s\rho_s(e_{i,s} + \frac{\vec{u}_s{}^2}{2})\right) + \nabla\cdot\left(\rho_s\vec{u}_s(h_s + \frac{\vec{u}_s{}^2}{2})\right) = \nabla\cdot(\lambda_s\nabla T_s) + \nabla\cdot(\vec{u}_s\cdot\sigma_s) + h_{ls}(T_s - T_l) + (\dot{m}_{ls}h_l - \dot{m}_{sl}h_s) \tag{53}$$

where ρ_q is the density of the phase where the subscript q denotes the phase either liquid or solid, in $\mathrm{kg\,m^{-3}}$, α_q is the volume fraction, $\mathrm{m^3\,m^{-3}}$, $\vec{u}_q$ is the velocity vector in $\mathrm{m\,s^{-1}}$, $e_{i,q}$ is the internal energy $\mathrm{J\,kg^{-1}}$, h_q is the enthalpy $\mathrm{J\,kg^{-1}}$, λ_q is the thermal conductivity in $\mathrm{W\,(m\,K)^{-1}}$, σ_q is the viscous stress tensor in $\mathrm{kg\,(m\,s)^{-2}}$, h_{sl} or h_{ls} is the volumetric heat transfer coefficient between both phases in $\mathrm{W\,K^{-1}\,m^{-3}}$ ($h_{sl} = h_{ls}$) and $\dot{m}_{s,l}$ is the volumetric mass transfer from $_s$-phase to $_l$-phase and vice versa, in $\mathrm{kg\,s^{-1}\,m^{-3}}$.

In the previous equations Eq. (52) and Eq. (53) the term $\frac{\partial}{\partial t}\left(\rho(e_q + \frac{\vec{u_q}{}^2}{2})\right)$ is the *accumulation term*, and represents the variation of energy over time for each $_q$-phase, while $\nabla\cdot\left(\rho\vec{u}_q(h_q + \frac{\vec{u_q}{}^2}{2})\right)$ is the *advection* or *convection term* and describes the transport of energy for each $_q$-phase out the parcel across its boundaries by the fluid flow. Both terms units are $\mathrm{J\,s^{-1}\,m^{-3}}$. On the right-side of the equations, the term $\nabla\cdot(\lambda_q\nabla T_q)$ represents the *diffusion term* of energy due heat conduction for each $_q$-phase. The term $\nabla\cdot(\vec{u}_q\cdot\sigma_q)$ accounts for the conversion of kinetic energy into internal energy due to the viscous stresses. The term $h_{sl}(T_l - T_s)$ or $h_{ls}(T_s - T_l)$ accounts for the heat transfer between both phases and and the term $(\dot{m}_{sl}h_s - \dot{m}_{ls}h_l))$ or $(\dot{m}_{ls}h_l - \dot{m}_{sl}h_s)$ summarizes the amount of energy regarding the mass transfer from of phase to the other. All right-side terms units are also $\mathrm{J\,s^{-1}\,m^{-3}}$.

7.2.6 Turbulence equations

To describe the effects of the turbulence fluctuations without the direct application of the *Navier-Stokes equation* in a very fine grid, the Reynolds Averaged Navier Stokes (RANS) equations are applied.

There are three methods for modelling turbulence in multiphase flows:

- The *mixture* turbulence model is suitable for scenarios where phase separation occurs, such as stratified (or nearly stratified) multiphase flows, and when the density ratio between phases is close to 1. In those cases, using mixture properties and velocities is sufficient to capture key aspects of turbulent flow.

- The *dispersed* turbulence model is more appropriate when secondary phase concentrations are dilute or when the granular model is employed. In this model, the fluctuating quantities of the secondary phases are expressed in terms of the mean properties of the primary phase, along with the ratio of particle relaxation time to eddy-particle interaction time. This model is ideal when there is one primary continuous phase, and the other phases are dispersed and dilute.

- The most general multiphase turbulence model solves a set of turbulence and transport equations for *each phase*. It is the best choice when turbulence transfer between phases plays a significant role. However, is more computationally demanding compared to the dispersed turbulence model.

NOTE: As an initial approach and based on the literature review, the mixture turbulence model will be used. Future research, validated with experimental data should assess the differences between these models and their resulting behaviours to identify the turbulence model that most accurately represents the ice slurry fluid flow patterns in the crystallizer.

$k-\epsilon$ ***mixture*** **turbulence model**

The transport equation for turbulent kinetic energy k is:

$$\frac{\partial}{\partial t}(\rho_m k) + \nabla \cdot (\rho_m \vec{u_m} k) = P_{k,m} - \rho_m \epsilon + \nabla \cdot \left[\left(\mu_m + \frac{\mu_{t,m}}{\sigma_k} \right) \nabla k \right] \tag{54}$$

The transport equation for the dissipation rate ϵ is:

$$\frac{\partial}{\partial t}(\rho_m \epsilon) + \nabla \cdot (\rho_m \vec{u_m} \epsilon) = C_{\epsilon 1} \frac{\epsilon}{k} P_{k,m} - C_{\epsilon 2} \rho_m \frac{\epsilon^2}{k} + \nabla \cdot \left[\left(\mu_m + \frac{\mu_{t,m}}{\sigma_\epsilon} \right) \nabla \epsilon \right] + S_{k,m} \tag{55}$$

where $P_{k,m}$ is the production of turbulent kinetic energy, σ_k and σ_ϵ are model constants (typically $\sigma_k = 1.0$ and $\sigma_\epsilon = 1.3$), $C_{\epsilon 1}$, $C_{\epsilon 2}$, C_μ are empirical constants (typically $C_{\epsilon 1} = 1.44$ and $C_{\epsilon 2} = 1.92$), and ρ_m and μ_m are the mixture density and dynamic viscosity calculated as follows:

7.2.7 Interphase heat transfer coefficient

The volumetric energy transfer rate between phases is assumed to be a function of the temperature difference, the volumetric interphase heat transfer coefficient h_{sl} or h_{ls} and the interfacial area A_{sl} (see section Sec. 7.2.9.

The volumetric interphase heat transfer coefficient h_{sl} or h_{ls} is related to the $_q$-phase Nusselt number Nu_s.

$$h_{sl} = h_{ls} = \frac{\lambda_l Nu_s}{d_s} \tag{56}$$

where λ_l is the thermal conductivity of the fluid phase, in $\mathrm{W\,(m\,K)^{-1}}$, and d_s is the characteristic diameter of the solid particles, in m.

In the case of granular flows the Gunn (1978) correlation is applicable to a porosity range of 0.35–1.0 and a Reynolds number of up to 10^5

$$Nu_s = (7 - 10\alpha_l + 5\alpha_l^2)(1 + 0.7 Re_s^{0.2} Pr^{1/3}) + (1.33 - 2.4\alpha_l + 1.2\alpha_l^2) Re_s^{0.7} Pr^{1/3} \tag{57}$$

7.2.8 Kinetic theory of granular flows

The Kinetic theory of granular flows, aka granular theory of solids, is theoretical framework used to describe the macroscopic behaviour of dense granular materials, which consist of discrete particles (like sand, grains, or powders). These materials exhibit unique behaviours that differ from conventional fluids or solids because of the interactions between the particles. The theory aims to explain how factors like solids pressure (p_s), granular temperature (Θ_s), and bulk viscosity (ξ) govern the collective motion of these particles and provides a set of transport equations that govern the flow and evolution of granular systems in fluid flows.

Granular temperature

The granular temperature Θ_s is a measure of the average kinetic energy of the random motion of particles in a granular material, analogous to thermal temperature in molecular gases. It is often defined in terms of the mean square velocity of particles:

$$\Theta_s = \frac{1}{3} u_i u_i \tag{58}$$

where u_i account for the fluctuating velocity of the solids particles within the finite volume in $\mathrm{m\,s^{-1}}$, and the $\frac{1}{3}$ term arises for the three dimensional geometry. The resulting units for the granular temperature Θ_s are $\mathrm{m^2\,s^{-2}}$.

The granular temperature transport equation takes the form of:

$$\frac{3}{2}\left[\frac{\partial}{\partial t}(\rho_s \alpha_s \Theta_s) + \nabla \cdot (\rho_s \alpha_s \vec{u_s} \Theta_s)\right] = \left(-p_s \bar{\bar{I}} + \bar{\bar{\tau}}_s\right) : \nabla \vec{u_s} + \nabla \cdot (k_{\Theta_s} \nabla \Theta_s) - \gamma_{\Theta_s} + \varphi_{ls} \tag{59}$$

where ρ_s is the density of the granular material $\mathrm{kg\,m^{-3}}$, α_s is the volume fraction $\mathrm{m^3\,m^{-3}}$, Θ_s is the granular temperature $\mathrm{m^2\,s^{-2}}$, $\vec{u_s}$ is the macroscopic velocity of the granular flow $\mathrm{m\,s^{-1}}$, p_s is the solid pressure Pa, $\bar{\bar{\tau}}_s$ is the stress tensor $\mathrm{kg\,m^{-2}\,s^{-1}}$. $\left(-p_s \bar{\bar{I}} + \bar{\bar{\tau}}_s\right) : \nabla \vec{u_s}$ represents the generation of energy by the solid stress tensor. k_{Θ_s} is the diffusion coefficient for the granular energy flux, γ_{Θ_s} is the collisional dissipation energy and $\varphi_{ls} = -3k_{l,s}\Theta_s$ is the energy exchange between the fluid or solid phase.

The diffusion coefficient, k_{Θ_s} for granular energy in the Syamlal et al. model is given by:

$$k_{\Theta_s} = \frac{15 d_s \rho_s \alpha_s \sqrt{\Theta_s \pi}}{4(41 - 33\eta)}\left[1 + \frac{12}{5}\eta^2(4\eta - 3)\alpha_s g_{0,ss} + \frac{16}{15\pi}(41 - 33\eta)\eta\alpha_s g_{0,ss}\right] \tag{60}$$

where $\eta = \frac{1}{2}(1 + e_{ss})$.

And the collisional dissipation energy, γ_{Θ_s} is given by:

$$\gamma_{\Theta_s} = \frac{12(1 - e_{ss}^2) g_{0,ss}}{d_s \sqrt{\pi}} \rho_s \alpha_s^2 \Theta_s^{\frac{3}{2}} \tag{61}$$

Solids pressure

For granular flows in the compressible regime (where the solids volume fraction is less than the maximum allowed value), a solids pressure is considered to account for the weight of overlaying particles and inter-particle forces regarding collisions. The solids pressure p_s in granular flows can be modelled considering a kinetic term and a second term due to particle collisions as in the following equation:

$$p_s = \alpha_s \rho_s \Theta_s + 2\rho_s (1 + e_{ss}) \alpha_s^2 g_{0,ss} \Theta_s \tag{62}$$

where ρ_s is the particle density in $\mathrm{kg\,m^{-3}}$, Θ_s is the granular temperature $\mathrm{m^2\,s^{-2}}$, $g_{0,ss}$ is the radial distribution function (explained below), and e_{ss} is the coefficient of restitution (which ranges from 0 to 1, where 0 represents perfectly inelastic collisions and 1 represents perfectly elastic collisions).

For the radial distribution function, the following empirical expression for one solid phase is given in Gidaspow:

$$g_{0,ss} = \left[1 - \left(\frac{\alpha_s}{\alpha_{s,max}}\right)^{\frac{1}{3}}\right]^{-1} \tag{63}$$

The radial distribution function introduces a correction factor that modifies the probability of collisions between the particles when the solid granular phase becomes dense.

Solids bulk viscosity

The solids bulk viscosity, ξ accounts for the resistance of granular flow to compression or expansion. It is an important parameter when studying the dissipative nature of granular flows. According to ANSYS.Inc, in Lun et al. the following expression is proposed for it:

$$\xi = \frac{4}{3}\alpha_s^2 \rho_s d_s g_{0,ss}(1 + e_{ss})\sqrt{\frac{\Theta_s}{\pi}} \tag{64}$$

where α_s is the solid volume fraction $\mathrm{m}^3\,\mathrm{m}^{-3}$, ρ_s is the density of the granular material $\mathrm{kg\,m}^{-3}$, d_s is the characteristic diameter of the particles in m, $g_{0,ss}$ is the radial distribution function and e_{ss} is the coefficient of restitution (both non-dimensional) and Θ_s is the granular temperature $\mathrm{m}^2\,\mathrm{s}^{-2}$. The resulting units for ξ are $\mathrm{kg\,(m\,s)}^{-1}$ or $\mathrm{Pa\,s}^{-1}$

For highly inelastic granular flows, the bulk viscosity ξ is typically much larger than the shear viscosity μ, reflecting the strong resistance to changes in volume compared to resistance to shear deformation.

7.2.9 Interfacial area concentration

The interfacial area concentration, A_{sl} is the area between two phases per unit volume. This parameters is used when applying to mass, momentum and energy transfer between phases.

Algebraic interfacial area concentration models are derived from the surface are to volume ratio:

$$A_{sl} = \frac{\pi d_s^2}{\frac{1}{6}\pi d_s^3} = \frac{6}{d_s} \tag{65}$$

where d_s is the diameter of the solid particles, in m, and the resulting A_{sl} in $\mathrm{m}^2\,\mathrm{m}^{-3}$.

7.3 Population Balance Equation model

7.3.1 Introduction

To investigate the *characteristic size* distribution of ice particles inside the crystallizer, it is necessary to introduce the concept of Population Based Equations (PBE). This approach is essential because, otherwise, accurately capturing particle size would necessitate discretizing and solving the conservation equations at the Kolmogorov scale, which would be computationally unaffordable. Thus, a mathematical approach using the PBE must the used to assess the evolution of particle size distribution throughout the domain and time.

The proper consideration of ice particles' size and distribution inside the crystallizer is important for a thorough evaluation. Not only is it essential for accurately evaluating the rheological properties of the ice slurry, but also for calculating the particle fluid interaction forces, such as the drag force. These considerations directly influence the evolution of the crystallization process inside the crystallizer.

7.3.2 General Population Balance Equation

The PBE, also referred to in the literature as Population Based Model (PBM) are a set of equations which describe the evolution of a specific characteristic of a population of particles, in our case, the size or volume.

The general assumption on the implementation of the PBE for the particle size distribution is that crystals can be characterized by a single length parameter, denoted as L in the Population Balance Equations and which is equal to the particle characteristic diameters d_s denoted in the CFD equations $L = d_s$. This assumption implies the presence of a one-dimensional particle size distribution, represented as $ndf(L)$. Since ndf is a density function, $ndf(L)dL$ represents the number of ice particles -by unit volume- of size between L and $L + dL$ (Mazzotti et al.).

The number density function can be also characterized by some external coordinates as $\vec{x}$, which expresses the position and time t inside the considered domain, resulting in $ndf(\vec{x}, L, t)$.

The local number density of particles $n_{v,l}(\vec{x}, t)$ in a specific physical space of the domain is for any time:

$$n_{v,l}(\vec{x}, t) = \int_0^\infty ndf(\vec{x}, L, t)\, dL \tag{66}$$

The total amount of particles in the whole domain $\Omega_{\vec{x}}$, in a given instant of time t, is then:

$$n_v(t) = \int_{\Omega_{\vec{x}}} \int_0^\infty ndf(\vec{x}, L, t))\, dL\, d\Omega_{\vec{x}} \tag{67}$$

The calculation of the ice crystal size includes different phenomena like nucleation, growth, aggregation and breakage as represented visually in Fig. 39.

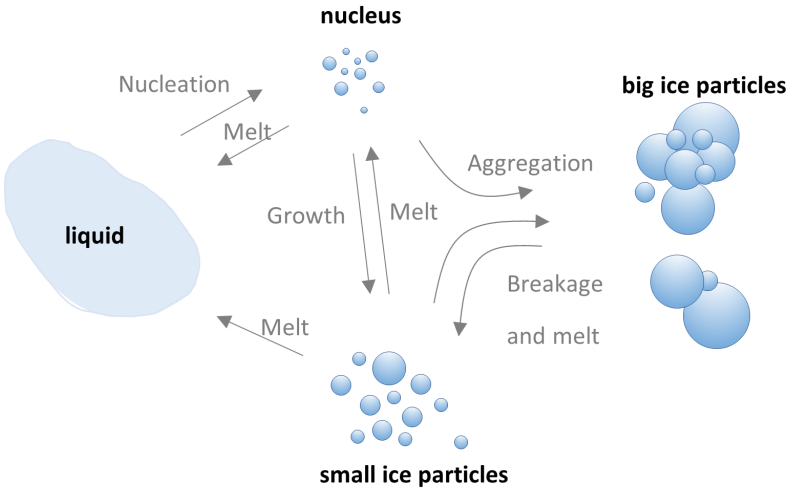

Figure 39: Dynamics of ice crystal based on Du et al. (2023)

The PBE formulation considered, for every volume control of the domain (thus simplifying for the $\vec{x}$) , reads as:

$$\underbrace{\frac{\partial\ ndf(L,t)}{\partial t}}_{\text{Cumulative term}} + \underbrace{\nabla[\vec{u}\ ndf(L,t)]}_{\text{Convection}} + \underbrace{\frac{\partial[Gro_v(L)\ ndf(L,t)]}{\partial L}}_{\text{Growh rate}} = \underbrace{Agg(L,t)}_{\text{Aggregation}} + \underbrace{Bre(L,t)}_{\text{Breakage or attrition}} + \underbrace{Nuc(L,t)}_{\text{Nucleation}} \tag{68}$$

where the first term, the *cumulative*, represents the rate of change of the number density of particles with respect to time. The second term represents the *advection* or *convection* of particles in the spatial (external) coordinate dimension. It describes how the number density of particles changes as a function of the external coordinates. The *growth rate* term represents the growth rate term for particles. The *aggregation* term represents the aggregation term of particles, also called coalescence. It accounts for the formation of larger particles through the collision and sticking together of smaller particles. The *breakage* or *attrition* term accounts for the fragmentation of larger particles into smaller ones due to external forces or collisions with other particles or with domain limits. The last term *nucleation* considers the rate at which the particles of size L are nucleated.

These terms together describe the evolution of the particle size distribution over time and capture the various processes that can occur in a population of ice particles.

7.3.3 PBE Growth rate term

The volumetric growth rate Gro_v is defined as the variation of volume per time unit in $\mathrm{m^3\,s^{-1}}$ given by:

$$Gro_v = \frac{\partial V}{\partial t} \tag{69}$$

The volume of a particle is expressed as a function of its characteristic length as:

$$V = K_v L^3 \tag{70}$$

where K_v is given by $\frac{\pi}{6}$ assuming particles are spherical. Using the above equations the Gro_v can be expressed as:

$$Gro_v = 3K_v L^2 \frac{\partial L}{\partial t} \tag{71}$$

The growth rate is defined in terms of particle's characteristic length, Gro_l, in $\mathrm{m\,s^{-1}}$ as:

$$Gro_l = \frac{\partial L}{\partial t} \tag{72}$$

Although specific equations for crystal growth rate for PBE have been described in the literature (Du et al., 2023, Xu et al., a,b), the growth rate expression used in the framework of this analysis is derived from the Langer and Müller-Krumbhaar (LM-K) theory outlined in section 7.1.2 as:

$$Gro_l = 1.2613\mathrm{e}{-04} \cdot T_{sc}^{2.4854} \tag{Eq. 31}$$

7.3.4 PBE Aggregation term

The aggregation expression, which accounts for the birth and death of particles of L size, is defined as:

$$Agg(L,t) = \frac{1}{2}\int_0^L k_{agg}(L-L',L')\cdot ndf(L-L',t)\cdot ndf(L,t)\,dL' - \int_0^\infty k_{agg}(L,L')\cdot ndf(L,t)\cdot ndf(L',t)\,dL' \tag{73}$$

The first part of Eq. accounts for the aggregation (aka birth) of ice particles of $L-L'$ and L' sizes, resulting in particles of size L. The factor $\frac{1}{2}$ is included to avoid counting twice each collision event. The aggregation kernel $k_{agg}(L-L',L')$, which has units of $\mathrm{m^3\,s^{-1}}$, is the aggregation rate between particles of sizes $L-L'$

and L', merging into a particle size L. The $ndf(L-L',t)$ express the number density function of particles of size $L-L'$ and similarly for $ndf(L,t)$. The second term accounts for the loss (aka death) of particles of size L by the aggregation of other particles of other sizes. Similarly, the aggregation kernel $k_{agg}(L,L')$, accounts for the aggregation rate between particles of sizes L and L', merging into a particle size $L+L'$.

Aggregation is a physical process that can be sequenced in two steps: the collision of two particles, and the sticking or fusion of these (ANSYS.Inc) (Xu et al., a). Therefore, some models define the aggregation kernel as the product of the probability of these two processes: *collision* and *coalescence*.

The aggregation kernel depends on the physical nature of the process. Different aggregation kernel models account for different physical nature of particles in fluids. The aggregation kernel model proposed in Luo, is composed by a collision frequency kernel and a probability that it results in coalescence. As it is based on applications dealing with bubbles, it is not the preferable option for the ice slurry phenomena. Similarly, aggregation kernel proposed in Prince as well as *Liao model* Liao et al. are based in bubbles coalescence.

In Smoluchowski an aggregation kernel for very small particles that collide due to Brownian motion, is proposed. The Brownian motion is commonly described as the random fluctuations or movements of particles suspended in a medium. It is assumed to be random and to depend on: the fluid temperature, the particle size and fluid viscosity. While the intensity of Brownian motion increases with temperature, i.e. higher temperatures mean more kinetic energy for the fluid molecules, the fluid viscosity damps the movement due to increased resistance.

For a Brownian motion assumption, long-range forces between the particles must be discarded, and the particles must be small enough (in the range 1 µm) to avoid influencing the fluid phase or being disturbed by fluid shear. In those cases, the collision frequency can be characterized by the following Eq. 74:

$$k_{agg,brownian}(L,L') = \frac{2k_BT}{3\mu}\cdot\frac{(L+L')^2}{LL'} \tag{74}$$

where k_B is the Boltzamnn's constant 1 380649e^{-23} in J K^{-1}, T the absolute temperature of the fluid in which the particles are colliding in K, μ is the fluid dynamic shear viscosity in kg (m s)$^{-1}$ or N s m^{-2} or Pa s J s kg^{-1} and L and L' are the characteristic lengths in m of the colliding particles. Consequently, the Brownian aggregation kernel proposed by Smoluchowski is not a good option as most of the particles are bigger.

Conversely, a turbulent aggregation kernel would be more suitable for our application involving turbulent flows as during mixing processes, mechanical energy is introduced into the fluid, generating turbulence. This turbulence leads to the formation of different scales of eddies, which dissipate the mechanical energy through viscous interactions. Consequently, in those turbulent conditions, particle aggregation occurs via two main mechanisms:

- in viscous subrange mechanism, for particles smaller than the Kolmogorov micro-scale, where local shear within the eddies affects particle collisions,
- or in inertial subrange mechanism, for particles larger than the Kolmogorov micro-scale, where particles exhibit independent velocities from local eddies.

Based on the work of Saffman and Turner, the collision rate in the viscous subrange is given by the following expression:

$$k_{agg,viscous}(L,L') = \zeta_T\sqrt{\frac{8\pi}{15}}\left(\frac{\epsilon}{\nu}\right)^{0.5}\frac{(L+L')^3}{8} \tag{75}$$

where ζ_T is a factor that accounts the coalescence efficiency of turbulent collision, ϵ is the dissipation of turbulent kinetic energy in m^2 s^{-3} , ν is the kinematic viscosity in m^2 s^{-1} , and L and L' are the characteristic lengths in m of the colliding particles.

In the inertial subrange, particles are larger than the smallest eddies, causing them to be carried along by the velocity fluctuations in the flow field. In this scenario, the aggregation rate is determined using Abrahamson.

$$k_{agg,inertial}(L,L') = \zeta_T 2^{\frac{3}{2}}\sqrt{\pi}\frac{(L+L')^2}{4}\sqrt{(U^2+U'^2)} \tag{76}$$

where U^2 is the mean square velocity of the particle in $m^2\,s^{-2}$, ζ_T is the coefficient for turbulent collision's coalescence efficiency which accounts for the hydrodynamic and attractive interactions between colliding particles and L and L' are the characteristic lengths in m of the colliding particles. In Higashitani et al. the following expression is proposed to evaluate the ζ_T :

$$\zeta_T = 0.732\left(\frac{5}{N_T}\right)^{0.242}; N_T \geq 5 \tag{77}$$

where N_T is the ratio between the viscous forces and Van der Waals force between two particles of L_i and L_j sizes in m.

$$N_T = \frac{6\pi\mu(L+L')^3\dot{\lambda}}{8A_{wi}} \tag{78}$$

where A_{wi} is the Hamaker constant in J, a constant depending on the particle material and $\dot{\lambda}$ is the deformation rate, in s^{-1} given by:

$$\dot{\lambda} = \left(\frac{4\epsilon}{15\pi\nu}\right)^{0.5} \tag{79}$$

where ϵ is the dissipation of turbulent kinetic energy in $m^2\,s^{-3}$, ν is the kinematic viscosity in $m^2\,s^{-1}$, $N\,m\,s\,kg^{-1}$ or $J\,s\,kg^{-1}$.

7.3.5 PBE Breakage term

The breakage expression, which accounts for the birth and death of particles of L size, is defined as:

$$Bre(L,t) = \int_{\Omega_L} ppp \cdot k_{bre}(L') \cdot pdf(L|L') \cdot ndf(L',t)\,dL' - k_{bre}(L) \cdot ndf(L,t) \tag{80}$$

In Eq. 80, the integral accounts, in all domain of particles Ω_L, for the formation or birth of new ice particles of size L, broken from a larger particle of size L' , resulting in particles of size L. The second term accounts for the loss or death of particles of size L by the breakage into other smaller particles. The coefficient ppp accounts for the number of child particles produced per broken parent particle (for example two for binary breakage). The breakage frequency $k_{bre}(L')$, which has units of s^{-1} , is the fraction of particles of size L' breaking per unit time. The $pdf(L|L')$ is the probability density function, in m^{-3} , of particles of size L' breaking into particle of size L.

Conversely to the aggregation term, the breakage term depends on the physical nature of the process. Different breakage kernel models, which have been proposed in previous research Luo,Liao et al. or Lehr et al. are based in bubbles breakage. Ghadiri and Zhang, in contrast to previous models, proposes a model only for the breakage frequency k_{bre} of the solid particles.

$$k_{bre}(L') = K_b u_s^2 d_s^{\frac{5}{3}} \tag{81}$$

where u_s is the particle velocity in $m\,s^{-1}$, d_s is the particle diameter prior to breaking, in m, and K_b is the breakage constant in $s^3\,m^{-11/3}$ which sets the overall scale of parents particles breaking per second and depends on $K_b \sim \frac{\rho_s E^{2/3}}{\gamma_{iw}^{5/3}}$, being ρ_s the particle density, E the elastic modulus of the granule and γ_{iw} the interface energy.

Complementary to the breakage frequency, a probability density function denoted as $pdf(L|L')$, defines the probability of a fragment with size L of being generated from the breakage of an L' sized particle. This probability is influenced by various factors, including particle properties such as strength or morphology. A parabolic probability density function is defined as follows:

$$pdf(L|L') = 0.5\left[\frac{c}{L'} + \frac{1-c/2}{L'}\left[24\left(\frac{L}{L'}\right)^2 - 24\left(\frac{L}{L'}\right) + 6\right]\right] \tag{82}$$

where L and L' are the daughter and parent particle sizes, respectively and c is a coefficient of the parabolic distribution function. For $c = 2$, the particle breakage has a uniform distribution. For $0 < c < 2$ the $pdf(L|L')$ results in a concave parabola distribution function, which means that is more likely to obtain unequally-sized fragments than equally-sized fragments.

7.3.6 PBE Nucleation term

The formulation of the nucleation equation has not been defined yet.

7.3.7 Coupling CFD and PBE models

The coupling procedure of the CFD and PBE model is depicted in Fig. 40. The CFD model solves the conservation equations for the two-phase flow: mass, momentum and energy, providing phase volume fraction, temperature, pressure and velocity fields for both phases, which are then transferred to the PBE model. The PBE model solves the population balance equations, using the solutions from the CFD equations to obtain the particle size distribution governed by the following processes: nucleation, particle growth, agglomeration, and breakage of ice particles. The liquid and solid phase volume fractions of CFD are related to the particle size distribution and mass transfer processes obtained from PBE. These results are subsequently fed back into the CFD model to update the interphase forces, and the conservation equations are recalculated in an iterative loop as shown in Fig. 40, which constitutes the coupling mechanism.

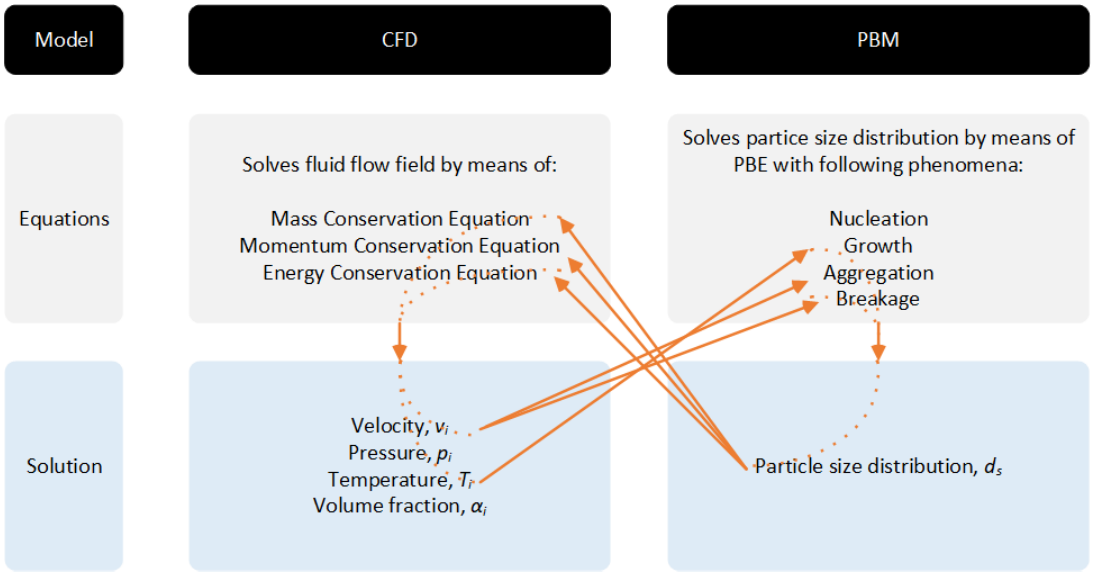

Figure 40: CFD and PBE model dependencies. Main equations for both models and coupled solutions.